

Untersuchung dünner Titandioxid- Photoelektrodenbeschichtungen mittels Rastersondenmikroskopie-Methoden

Von der Fakultät für Maschinenbau
der Helmut-Schmidt-Universität / Universität der Bundeswehr Hamburg
zur Erlangung des akademischen Grades einer Doktor-Ingenieurin / eines Doktor-Ingenieurs
genehmigte

DISSERTATION
vorgelegt von

Ragle Raudsepp.

aus *Haapsalu, Estland.*

Hamburg *2021.*

Gutachter 1: Prof. Thomas Klassen
Gutachter 2: Prof. Ian Sharp

Mündliche Prüfung am: 16.07.2021

*Investigation of thin titanium dioxide
photoelectrode coatings by scanning probe
microscopy methods*

Doctoral Thesis

approved by the

Department of Mechanical Engineering

of the

Helmut-Schmidt-University

University of the German Federal Armed Forces

for obtaining the academic degree of

Doktor Ingenieurin (Dr.-Ing.)

presented by

Ragle Raudsepp

from Haapsalu, Estonia

Hamburg 2021

DEDICATION

I dedicate this work to my parents

Rihti Raudsepp

and

Toomas Raudsepp

who have always supported and believed in me and have given me invaluable educational opportunities.

Abstract

In the transition from fossil fuels to renewable energy, efficient energy conversion and storage systems are required. One of the promising technologies that can support this transition is photoelectrochemical (PEC) water-splitting, in which solar energy is directly used to split water into oxygen and hydrogen. One of the main challenges in the design of efficient PEC systems is the optimization of the semiconductor material systems on the electrodes, which convert sunlight into electrochemical energy. The photoelectrochemical performance of these materials is significantly affected by the microstructure at the interface to the electrolyte, including the distribution of grains, grain boundaries and surface defects. Scanning probe microscopy (SPM) allows to simultaneously analyze and correlate morphological, mechanical, electrical and electrochemical properties at the nanometer scale.

In this work, a series SPM methods were employed to investigate, with high spatial resolution, the effect of film morphology on the electrical and electrochemical properties of semiconductor photoelectrodes. Thin TiO₂ films synthesized by atomic layer deposition (ALD) were used as model systems. Conductive atomic force microscopy (CAFM) measurements revealed anisotropy in the photocurrent activity, which was correlated with underlying crystalline orientations with the help of high-resolution topography and complementary microscopy techniques. Kelvin probe force microscopy (KPFM) studies revealed a slow charge redistribution upon and after illumination due to the trapping and detrapping of photogenerated charges. Current-voltage (I-V) characterization was employed to investigate charge carrier transport mechanisms occurring at the metal tip and crystalline TiO₂ nanojunction. Finally, electrochemical AFM (EC-AFM) was used to study the photocorrosion of partially crystalline TiO₂ *in-situ* under the working conditions of the photoanode. The results thus provide new insights into the fundamental microscopic processes in photoelectrodes, from which strategies for further efficiency improvements can be derived.

Kurzfassung

Beim Übergang von fossilen Brennstoffen zu erneuerbaren Energien sind effiziente Energieumwandlungs- und Speichersysteme erforderlich. Eine der vielversprechenden Technologien, die diesen Übergang unterstützen können, ist die photoelektrochemische (PEC) Wasserspaltung, bei der Sonnenenergie direkt zur Spaltung von Wasser in Sauerstoff und Wasserstoff verwendet wird. Eine der Hauptherausforderungen beim Entwurf effizienter PEC-Systeme ist die Optimierung der Halbleitermaterialsysteme auf den Elektroden, die Sonnenlicht in elektrochemische Energie umwandeln. Die photoelektrochemische Leistung dieser Materialien wird erheblich durch die Mikrostruktur an der Grenzfläche zum Elektrolyten beeinflusst, einschließlich der Verteilung von Körnern, Korngrenzen und Oberflächendefekten. Die Rastersondenmikroskopie (SPM) ermöglicht es, morphologische, mechanische, elektrische und elektrochemische Eigenschaften im Nanometerbereich zu analysieren und miteinander zu korrelieren.

In dieser Arbeit wurde eine Reihe von SPM-Methoden eingesetzt, um mit hoher räumlicher Auflösung den Einfluss der Filmmorphologie auf die elektrischen und elektrochemischen Eigenschaften von Halbleiter-Photoelektroden zu untersuchen. Dünne TiO₂-Filme, die durch Atomlagenabscheidung (ALD) synthetisiert wurden, wurden als Modellsysteme verwendet. Messungen mittels leitfähiger Rasterkraftmikroskopie (CAFM) ergaben eine Anisotropie der Photostromaktivität, die mit Hilfe von hochauflösenden Topographie- und komplementären Mikroskopietechniken mit kristallinen Orientierungen korreliert wurde. Kelvinsondenkraftmikroskop (KPFM) Studien zeigten eine langsame Ladungsumverteilung bei und nach der Beleuchtung aufgrund des Einfangens und Abfangens von photogenerierten Ladungen. Die Strom-Spannungs-Analyse (I-V) wurde verwendet, um Ladungsträgertransportmechanismen zu untersuchen, die an der Metallspitze und dem kristallinen TiO₂-Nanoübergang auftreten. Schließlich wurde elektrochemisches AFM (EC-AFM) verwendet, um die Photokorrosion von teilweise kristallinem TiO₂ *in-situ* unter typischen Arbeitsbedingungen der Photoanode zu untersuchen. Die Ergebnisse liefern damit neue Einblicke in die grundlegenden mikroskopischen Prozesse in Photoelektroden, aus denen sich Strategien für weitere Effizienzsteigerungen ableiten lassen.

Content

Abstract	i
Kurzfassung	ii
1. Introduction.....	1
2. Theory.....	3
2.1 Photoelectrochemical water-splitting theory	3
2.2 The Metal-semiconductor junction.....	5
Forward bias.....	5
Reverse bias.....	6
Junction under illumination	6
Charge carrier transport mechanisms at metal/semiconductor nanojunction	6
2.3 TiO ₂ as a photoanode for photoelectrochemical water-splitting	8
2.4 Scanning probe microscopy	10
2.5 Atomic force microscopy (history, operation principle)	10
2.5.1 Imaging modes	11
Contact mode AFM.....	11
Non-contact mode AFM	11
Tapping mode AFM	12
Peak-force tapping mode AFM.....	12
2.5.2 Artifacts and processing of AFM images	13
Scanner artifacts.....	13
Probe artifacts	14
External and internal noise.....	15
Processing AFM images	15
2.5.3 Electrical modes	16
Conductive AFM	16
Spectroscopy mode CAFM	16
Kelvin probe force microscopy.....	17
2.6 Electrochemical techniques	20
Imaging in liquid	20
Open circuit potential.....	20
Cyclic voltammetry.....	20
Chronoamperometry.....	21
Tafel extrapolation	21
2.7 Atomic layer deposition	22
2.8 Photodeposition	23

2.9	Electron backscatter diffraction	24
3.	Experimental	26
4.	Results and discussion.....	29
4.1	Physicochemical properties.....	29
4.1.1	High resolution topography	29
4.1.2	Photoactivity variation	31
4.1.3	Selective Pt photodeposition	34
4.1.4	Identification of different grain types	36
	Literature discussion	37
	Grain identification.....	37
4.1.5	Crystal growth direction	38
4.2	Surface voltage mapping.....	40
4.2.1	CPD vs time.....	42
4.2.2	Instrumentation effects.....	45
4.3	Charge carrier transport mechanisms at tip-semiconductor nanojunction.....	47
	Current instabilities at the tip and sample nanocontact.....	51
4.4	Degradation of amorphous phase on partially crystalline TiO ₂ thin films	54
4.4.1	Influence of photoelectrochemical conditions on degradation rates.....	56
4.4.2	Evolution of roughness.....	59
5.	Conclusion and outlook.....	62
6.	Appendix.....	64
6.1	Physicochemical properties.....	64
6.2	Surface voltage mapping.....	66
6.3	Degradation of amorphous phase on partially crystalline TiO ₂ thin films	67
7.	References.....	71
	Acknowledgements.....	82
	Posters and Presentations at conferences.....	83
	Posters.....	83
	Presentations.....	83
	Publications	84
	Manuscripts in preparation:.....	84

1. Introduction

As the world is in transition from fossil fuels to renewables, efficient energy conversion and storage systems are of great importance, since the main sustainable energy sources at the moment, wind and solar, are naturally strongly fluctuating. Energy production has to match the peak demand in consumption. However, overproduction of renewables is currently wasted due to the lack of efficient storage systems and due to costs. Countries are forced to shut down wind turbines, pay for neighboring countries to accept the surplus electricity, or set the price for the customers to negative values, meaning that households would pay for producing electricity. In order to overcome such unfavorable situations, efficient storage systems for the excess energy are required, for later use during low energy production periods. Currently existing major storage systems include pumping water to higher elevated tanks. Perspectively charging batteries and using water electrolysis to generate hydrogen may be scalable solutions, other options are less promising on a large scale.

Hydrogen is not only a clean energy carrier, but is also used in the chemical industry to produce ammonia, methanol, hydrogen peroxide, as well in metallurgy, oil refinery, etc. Currently the main hydrogen production method is steam reforming of methane, which is not sustainable and is expensive due to the need for noble metal catalysts. Therefore, the production of green hydrogen through electrolysis would not only help store the surplus energy from the sun and wind, but would also transform hydrogen production towards industrial sustainability. Moreover, hydrogen produced by using only water and electricity is clean, avoiding further expensive purification processes. This is extremely important when using hydrogen as an energy carrier, since fuel cells are overly sensitive to carbon and sulfur impurities.

Hydrogen can be stored in a high-pressure tanks, in cryogenic tanks as liquid hydrogen, or in solid storage systems based on metal hydrides. Storage in form of chemical compounds, like ammonia or methane, or other synfuels is also feasible, but so far less energy-efficient.

Green hydrogen production via water electrolysis combined with renewable energy sources has been demonstrated at large scales. For example in Aarau, Switzerland, hydropower is used to run the water-splitting reaction inside a renewable electrolyzer plant [1]. Hydrogen is then distributed to fueling stations to charge fuel cell vehicles. An electrolyzer power plant with 100 MW capacity, powered by wind and solar energy, is planned to be built in Hamburg, Germany, by 2025 [2]. In addition to solar and wind energy, wave energy has also been used to run electrolysis systems to generate green hydrogen [3], [4]. Using electrolysis combined with renewable energy sources is already a big step forward and helps to store excess energy.

However, a more elegant and perspectively more energy-efficient technology is the combination of solar absorbers and water splitting in only one cell. This so-called photoelectrochemical (PEC) water-splitting, also named “direct” photoelectrolysis, is an alternative to combined photovoltaic (PV)/electrolyzer systems. The straightforward idea of the PEC water-splitting device is that the photoactive material that can adsorb sunlight and provides the energy to split water, is placed directly in the water reservoir. The PEC water-splitting device has several advantages over PV powered electrolysis: *i*) 100 times lower current densities, which decreases the loss of active electrode area [5], *ii*) improved thermal management due to cooling by the electrolyte, which avoids losses in efficiency, *iii*) lower cost, as the number of components (wiring, inverters, etc.) is decreased [6], [7].

However, to realize PEC as a main hydrogen production technology, major breakthroughs are still required. These involve discovering/developing new absorber materials, large-scale device design, and standardized references for benchmarking the efficiency and stability [5]. One of the biggest challenges of the PEC device is the optimization of the photoactive material for the oxygen evolution electrode, i.e. on the photoanode. It needs to absorb a wide spectrum of solar light, be stable in oxidative and corrosive environments, and should be non-toxic and abundant. Until now, no such material that meets all the aforementioned requirements has been identified. To be able to identify promising photoelectrode materials, in-depth understanding of the processes taking place under various conditions is essential. Due to the physical and theoretical limits governed by the charge carrier diffusion length, the optimal thickness of the absorber material is often on the nanometer scale. Otherwise, electrons and holes recombine before the water splitting can take place. Most common photoanode absorber materials like TiO₂ have optimal film thickness of up to 100 nm [8], [9], BiVO₄ also up to 100 nm [10], [11], WO₃ up to 150 nm [12] and Fe₂O₃ only up to few nanometers [13], [14]. Therefore, to observe and understand the processes occurring at nanoscale, powerful screening and characterization methods are needed.

In this work, a scanning probe microscope (SPM) is used as a central characterization instrument to study the surface of water-splitting photoanodes. SPM utilizes a nanoscale tip to scan the sample topography, simultaneously measuring the mechanical, electrical, and electrochemical properties with high spatial resolution in dark conditions and under illumination. Atomic layer deposited (ALD) TiO₂ was chosen as model system to investigate the basic phenomena involved.

After description of the fundamental theory and the presentation of the experimental details, the results of this thesis are divided into four sections:

In **Chapter 4.1** a wide range of physicochemical studies were conducted on the TiO₂ sample series. Variations in the photocurrent were observed and correlated with the surface morphology as well as with the crystalline structure of the samples.

In **Chapter 4.2** surface voltage and photovoltage was measured for both crystalline and amorphous phase TiO₂. Trapping and detrapping of photogenerated charge carriers was observed by measuring the potential as a function of time in dark conditions and under illumination.

In **Chapter 4.3** the main charge carrier transport mechanisms at the metal tip and TiO₂ nanojunction were determined by fitting the current-voltage (I-V) relationships measured at each pixel for AFM scans in dark conditions and under illumination.

In **Chapter 4.4** degradation of amorphous phase on a partially crystalline TiO₂ samples was observed under the working conditions of photoanode. The loss of amorphous material was observed *in-situ* with electrochemical atomic force microscopy (EC-AFM).

Finally, the main conclusions are drawn and an outlook is given.

The main goal of this work is to elucidate the effect of microstructure, including roughness, distribution of grains, grain boundaries and surface defects, on the performance of water splitting photoanodes. Fundamental studies are vital to gain an in-depth understanding of the complex processes taking place at photoelectrodes, and are step forward that helps to design novel efficient materials in pursuit of economically viable PEC devices.

2. Theory

2.1 Photoelectrochemical water-splitting theory

The most crucial and challenging part of the photoelectrochemical water-splitting system is the photoactive semiconductor material. In dark conditions, an undoped semiconductor has a fully filled valence band and an empty conduction band, separated by a characteristic band gap, wide enough that no charge carrier can overcome the gap and the material has a conductivity close to an insulator. Upon illumination, if the photon energy is higher or equal than the bandgap, charge carriers are excited and gain enough energy to jump to the conduction band, thus become mobile and can facilitate the desired reactions. An electron, when leaving the valence band, leaves behind a positive charge called hole.

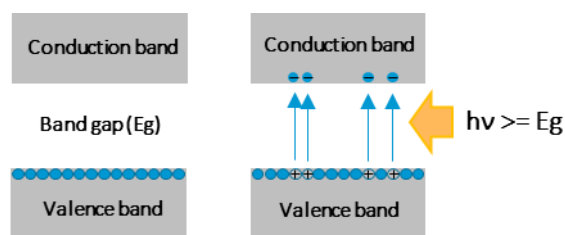


Figure 1. Simplified charge carrier generation in semiconductor under illumination.

In order to use the generated holes and electrons in water oxidation and hydrogen generation reaction, they need to be separated to avoid recombination. Charge separation can be achieved by applying an external bias voltage or by using the built-in potential. The latter is achieved when *i*) bringing a n-type and p-type semiconductor into contact with each other and thereby creating the p-n junction, *ii*) bringing the semiconductor into a contact with a metal (will be discussed in more detail in the following chapters) and *iii*) bringing the semiconductor into a contact with an electrolyte (in ambient conditions also the presence of water). All three mentioned charge separation methods are based on the Fermi level equilibration between the two materials/media. *Figure 2* presents the formation of the built-in potential when the semiconductor is immersed in the electrolyte. *Figure 2a* represents the flat band conditions where no built-in potential exist. Immersing a p-type electrode in the electrolyte causes the flow of electrons from the electrolyte to the semiconductor because the Fermi energy of the semiconductor is below the redox potential of the electrolyte [15]. This charge distribution causes the electrolyte on the semiconductor surface to be positively charged. With the n-type semiconductor, electrons flow the opposite direction because the Fermi energy of the semiconductor is higher than the redox potential of the semiconductor. This causes the electrolyte layer on top of the semiconductor to be negatively charged. The charged layer on the semiconductor surface is called the **Helmholtz layer** [16], [17], marked with gray shaded area on the *Figure 2*. On the *Figure 2b* the semiconductor surface is positively charged which attracts negative charge causing the region close to the surface become more negative compared with the bulk, this is called as **accumulation region** [16]. The potential energy of an electron decreases, and bands bend downwards. On the *Figure 2c* semiconductor surface is negatively charged causing the region close to the surface being more positively charged compared with the bulk. This is called the **depletion region** [16] since the number of majority charge carriers is depleted. The bands bend upward as the electron in the semiconductor feels the repulsion from the surface causing its potential energy to increase. If the minority carrier concentration near the surface gets higher than the majority carrier concentration and the latter decreases below the intrinsic carrier density, bands bend even further upwards, and an **inversion layer** [17] is formed. This means that n-type semiconductor near the surface behaves like p-

type. Band bending region is also called as **space charge layer** [16]–[18], and the larger the width (w) of this layer, the better is the charge separation. Hence, a built-in potential in the semiconductor occurs also when there is no contact with other material or media (in vacuum) due to the surface states [19].

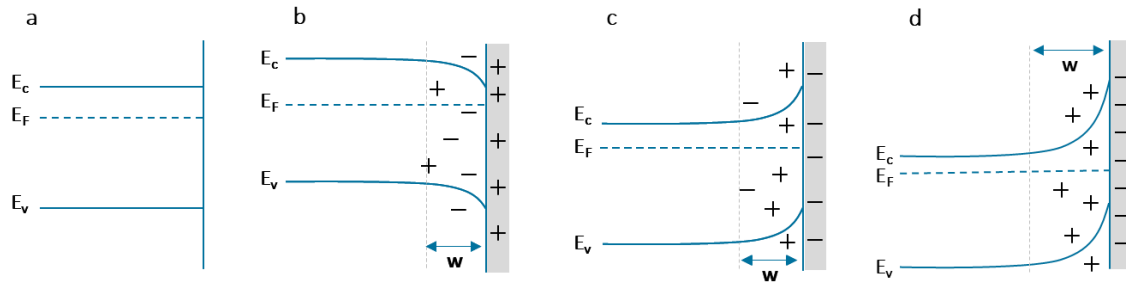
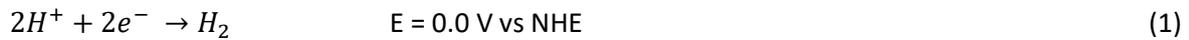


Figure 2. Formation of the built-in potential due to the charge distribution within the semiconductor near the surface. Adapted from [20].

Since the n-type semiconductor was studied in this work, the following illustrations are done using it as an example, but similar behavior (although with different polarity) is observed for p-type semiconductors. After the charge carrier generation due to the photon absorption and separation by the built-in potential, electrons and holes can be consumed in water-splitting reactions. In order to run the photoelectrochemical water-splitting reaction, the valence band edge must be more positive than the water oxidation potential, which is 1.23 V vs NHE, and the conduction band edge must be more negative than the water reduction potential, which is 0 V vs NHE. The required thermodynamical potential for water-splitting reaction is 1.23 V but in practice an overpotential is needed due to the complex four-electron-involved process taking place on a photoanode [21], [22]. Other processes that also contribute to the need of overpotential are: losses coming from the charge transfer through the external circuit and space charge layer, charge recombination, incomplete band flattening due to the surface states [23]. Under illumination electrons in the conduction band move towards the semiconductor back contact and from there through the external circuit to the metal electrode (cathode) where they are consumed in hydrogen generation reaction (half reaction 1) [24]. The holes move towards the surface to run the water oxidation reaction (half reaction 2) [24]. Both half reactions and thermodynamical potentials are valid in acidic media at pH 0. Increasing the pH, both potentials change by 0.059 V per 1 pH value.



Under the illumination, the Fermi level splits and quasi-Fermi level for holes ($E_{F,p}$) and electrons ($E_{F,n}$) are formed. The potential difference between the two quasi-Fermi energies, when no current flows through the system, is called the photovoltage (V_{ph}). V_{ph} is the driving force to run the water-splitting reaction [25].

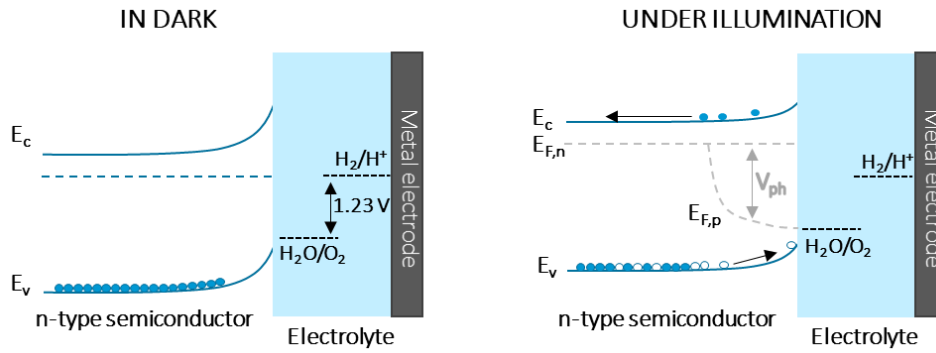


Figure 3. Band energy diagrams in dark and under illumination, adapted from [25]. Upon illumination quasi-Fermi levels for holes and electrons are formed.

Since the four-electron-involved oxygen evolution reaction (OER) is the bottle neck for the overall water-splitting reaction, the main focus is often on the photoanode to make the solar water-splitting more efficient. Therefore, also in this work photoanode material was studied.

2.2 The Metal-semiconductor junction

Similarly to the equilibration processes at the semiconductor/electrolyte junction, when bringing a semiconductor into a contact with a metal, electrons from the material with lower work function (ϕ) will flow towards the material with higher work function, until the Fermi levels are aligned (*Figure 4a*).

If the work function of the metal (ϕ_m) is larger than the work function of the semiconductor (ϕ_s), electrons from the conduction band of the semiconductor will flow towards the metal, which causes a decrease in the concentration of free electrons in the semiconductor near the interface. A space charge layer is formed, with energy bands bending upwards. A barrier is formed at the junction, between the Fermi energy of the metal and the bottom edge of the conduction band in the semiconductor, called a Schottky barrier (ϕ_B). The Schottky barrier gives the junction a rectifying behavior, which means that current flow is favored in only one direction. The most important characteristic of the Schottky barrier is its height (Schottky-Barrier Height, "SBH", ϕ_B). For an n-type semiconductor, its value corresponds to the difference between the metal work function (ϕ_m) and the electron affinity of the semiconductor (χ_s) [20], which is the energy difference between the semiconductor local vacuum level and the bottom edge of the conduction band [26]. If the $\phi_m < \phi_s$ no Schottky barrier is formed and the metal-semiconductor contact is Ohmic [20].

When applying bias to the system the equilibrium band diagram is altered. Nevertheless, as the metal work function is pinned to its vacuum level and the valence and conduction band edges of a semiconductor are pinned as well, the SBH is theoretically unaffected by the applied bias [27]. However, the current flow across the junction can be influenced by applying a potential difference (bias voltage) between semiconductor and metal.

Forward bias

When a potential is applied to the semiconductor that is more negative with respect to the metal, the Fermi level in the semiconductor shifts upwards, and correspondingly the band bending and the width of a space charge layer are reduced. Since the potential barrier is reduced, the flux of electrons from the semiconductor to the metal is increased compared to the thermal equilibrium condition. In this condition the junction (*Figure 4b*) is said to be under forward bias. Since the applied bias has the same

polarity as the barrier, a semiconductor-metal junction under enough forward bias shows ohmic behavior [28].

Reverse bias

When the semiconductor is biased more positive than the metal, the Fermi level in the semiconductor shifts downwards. Band bending and depletion width are increased, and correspondingly the built-in voltage is increased. In this condition the junction is said to be under reverse bias (*Figure 4c*). As the potential barrier is increased, electrons require more energy to overcome the barrier. Under high reverse bias voltages, the depletion layer behaves like insulator, creating a metal-insulator-semiconductor (MIS) system [28].

Under equilibrium, at zero bias (*Figure 4a*), current from the metal to the semiconductor (I_{ms}) and from the semiconductor to the metal (I_{sm}) are equal and no current flows between the two materials [29]. Applying forward bias, I_{sm} dominates over saturation current (I_0) which under forward bias is defined as a recombination and leakage current [29] (*Figure 4b*). Under high reverse bias, due to the increased depletion layer, I_{sm} is negligible and the current depends only on the I_0 (*Figure 4c*).

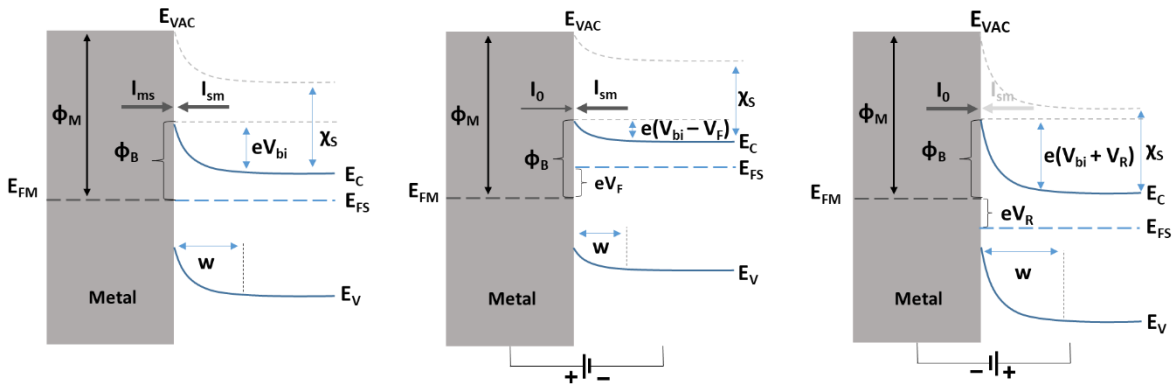


Figure 4. Metal-semiconductor contact under equilibrium (left), under forward (middle) and reverse (right) bias conditions. E_{FM} : metal Fermi level, E_{FS} : semiconductor Fermi level, E_{VAC} : local vacuum level, ϕ_M : metal work function, ϕ_B : Schottky barrier height, V_{bi} : built-in potential, e : elementary charge, E_C : conduction band minimum, E_V : valence band maximum, w : width of a space charge layer, V_F : forward bias and V_R : reverse bias.

Junction under illumination

Under illumination, electron and hole pairs are created in the semiconductor. Minority carriers move towards the interface and majority carriers away from it, generating an electric field that counters the field of the space charge layer. This causes Schottky barrier to decrease and leads to enhanced current [30].

Charge carrier transport mechanisms at metal/semiconductor nanojunction

Charge carrier transport at the metal-semiconductor nanojunction can follow several mechanisms: *i*) Schottky emission/Thermionic emission, *ii*) Thermionic field emission, *iii*) Fowler-Nordheim tunneling, *iv*) Poole-Frenkel emission, *v*) Direct tunneling/field emission, *vi*) Hopping conduction and *vii*) space charge limited conduction (SCLC). All the aforementioned transport mechanisms except SCLC are presented on *Figure 5*. Expressions and linear relationships of the transport mechanisms are summarized in *Table 1*.

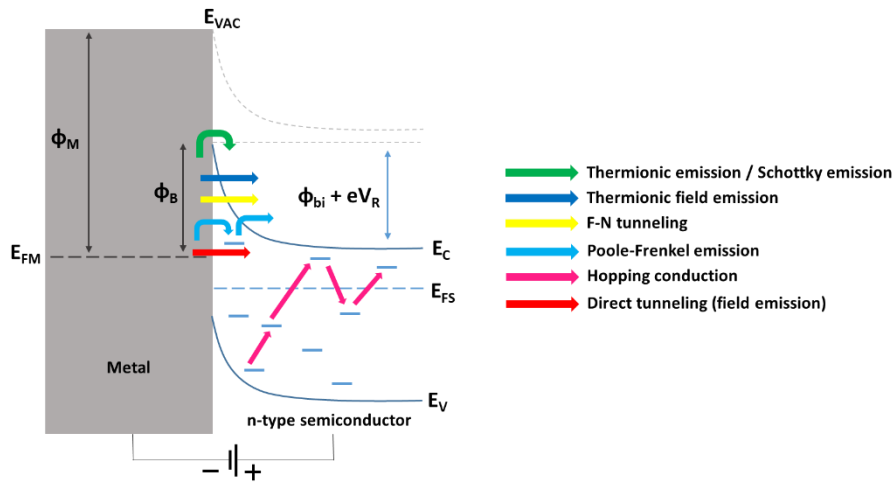


Figure 5. Charge carrier transport mechanisms at metal-semiconductor interface under reverse bias.

Thermionic emission and *Schottky emission* are current transports mechanisms in which electrons in the metal gain enough energy (by thermal or photoactivation) and are able to overcome the potential barrier. It occurs when carrier concentration in semiconductor is low, charge carriers have enough energy to overcome the barrier height, and the depletion width is large (>10 nm) [31]. It is the most common conduction mechanism occurring in Schottky barrier junctions [26].

Thermionic field emission takes place when the semiconductor has an intermediate carrier concentration and depletion width [31].

Fowler-Nordheim tunneling occurs at higher voltages compared with direct tunneling. F-N tunneling is more prominent at metal-insulator-semiconductor contacts than at metal-semiconductor contacts [32]. Defect states that trap charge carriers hinder the F-N tunneling [33].

Poole-Frenkel emission, also called as internal Schottky emission, takes place when trapped electron gets excited into the conduction band [34], [35]. It often dominates at higher temperatures or at high electric field [34].

For a *space charge limited current*, a plot of I vs E^2 should be linear [36], [37]. Hence, this is only valid for trap free materials, for the presence of trapped states, the exponent is higher than 2 [38].

Hopping conduction takes place through localized states (electron trap states) within the band gap. The main difference between P-F tunneling is, that trapped charges do not gain enough energy to jump to the conduction band but instead tunnel through the states within the band gap.

Field emission and/or *direct tunneling* dominates if the semiconductor is highly doped and the depletion width is very small, which can lead to an Ohmic contact between the metal and the semiconductor [39]. Direct tunneling occurs when there is a thin, up to 3.5 nm, insulating oxide layer on the semiconductor (MIS contact) [34]. If the oxide layer is thicker, F-N tunneling is dominant over direct tunneling [33].

Table 1. Expressions and linear relationships of different conduction models at metal-semiconductor junction.

Conduction model	Expression	Linear relationship	Sources
Schottky emission (reverse bias)	$I_0 = A_{\text{eff}} A^* T^2 \exp\left(-\frac{q}{kT}(\varphi_B - \sqrt{qE_m/4\pi\epsilon_s})\right)$	$\ln I \text{ vs } E^{\frac{1}{2}}$	[36], [40], [41]
Thermionic field emission	$I = A_{\text{eff}} \frac{q^2 \sqrt{m} (kT)^{\frac{1}{2}} E_{\text{ox}}}{8\hbar^2 \pi^{\frac{5}{2}}} \exp\left(-\frac{q\varphi_B}{kT}\right) \exp\left(\frac{\hbar^2 q^2 E_{\text{ox}}^2}{24m(kT)^3}\right)$	$\ln\left(\frac{I}{E}\right) \text{ vs } E^2$	[34], [36], [42]
Fowler-Nordheim tunneling	$I = A_{\text{eff}} \frac{q^3}{16\pi^2 \hbar} \frac{m_e}{m_{\text{ox}}} \frac{E_{\text{ox}}^2}{\varphi_B} \exp\left(-\frac{4}{3} \frac{\sqrt{2m_{\text{ox}}}}{q\hbar} \frac{\varphi_B^{\frac{3}{2}}}{E_{\text{ox}}}\right)$	$\ln\left(\frac{I}{E^2}\right) \text{ vs } \frac{1}{E}$	[34], [36], [43], [44]
Poole-Frenkel emission	$I = A_{\text{eff}} q \mu N_{\text{cv}} \exp\left(-\frac{q}{kT}(\varphi_B - \sqrt{qE_{\text{ox}}/\pi\epsilon_{\text{ox}}})\right) E_{\text{ox}}$	$\ln\left(\frac{I}{E}\right) \text{ vs } E^{\frac{1}{2}}$	[34], [36], [40]
Direct tunneling	$I = I_{\text{FNT}} \exp\left(1 - \frac{qV_{\text{ox}}}{\phi_B}\right)^{3/2}$	$\ln\left(\frac{I}{E^2}\right) \text{ vs } \ln \frac{1}{E}$	[40], [44], [45]
Hopping conduction	$I = A_{\text{eff}} q \mu N_{\text{cv}} \exp\left(-\frac{\Delta E_{\text{ae}}}{kT}\right) E_{\text{ox}} = A q \mu n E_{\text{ox}}$	$\ln I \text{ vs } E$	[34], [36], [40]
Space charge limited current	$I = A_{\text{eff}} E_{\text{ox}} \exp\left(-\frac{E_t}{kT} \ln\left(\frac{qH_t d}{2\epsilon_0 \epsilon_r E_{\text{ox}}}\right)\right)$	$I \text{ vs } E^2$	[10], [36], [37]

I_0 : saturation current, I : electrical current, A_{eff} : effective emission area, m_{ox} : effective charge carrier mass in the oxide, m_e : free electron mass, \hbar : reduced Planck constant, q : electron charge, φ_B : Schottky barrier height, $E_{\text{ox}} = V_{\text{ox}}/d_{\text{ox}}$: electrical field across the oxide, V_{ox} : effective oxide voltage, d_{ox} : effective oxide thickness, ΔE_{ae} : carrier activation energy difference, T : absolute temperature, A^* : Richardson constant, ϵ_{ox} : permittivity of the oxide, k : Boltzmann constant, N_{cv} : density of states, n : charge carrier density, μ : carrier mobility, ϵ_s : permittivity of the semiconductor, E_m : electrical field maximum, E_t : characteristic energy of trap state distribution, H_t : density of trap states, ϵ_0 : permittivity of free space, ϵ_r : dielectric constant, E (without suffix): the applied potential.

2.3 TiO₂ as a photoanode for photoelectrochemical water-splitting

Metal oxides are the most common semiconductor materials used as photoanodes in the photoelectrochemical water-splitting systems. This is due to their Earth abundance, suitable band gap for solar light absorption, band alignment and good stability in the oxidative environments. The most widely studied metal oxides for photoanode application are TiO₂ (band gap 3.2 eV) [46]–[52], BiVO₄ (2.3 - 2.5 eV) [10], [53]–[59], Fe₂O₃ (2.2 eV) [60]–[62], ZnO (2.2 eV) [63]–[65] and WO₃ (2.6 – 2.8 eV) [66]–[69]. Among the aforementioned metal oxides, TiO₂ has the largest band gap which means that only UV region wavelengths can excite the charge carriers. This limits the maximum theoretical solar-to-hydrogen (STH) efficiency to 1% [18]. However, TiO₂ is considered as one of the most stable photocatalyst in aqueous solutions [70] and therefore has paved a wide interest in various (photo)electrochemical processes.

TiO₂ has three stable crystalline forms: anatase (band gap 3.2 eV) [71], [72], rutile (3.0 eV) [71] and brookite (3.3 eV) [72], [73] and an amorphous phase with a band gap around 3.2 – 3.4 eV [74]–[76].

Anatase and rutile are most extensively studied crystalline forms since pure brookite is difficult to synthesize [77], [78]. Although rutile has a slightly smaller band gap which means it can absorb wider range of the solar spectrum, anatase is considered better photocatalyst due to: *i*) higher carrier life times while having indirect band gap compared with rutile which has direct band gap [79], [80], *ii*) better charge transfer due to the higher energy level of the valence band maximum [80], [81], and *iii*) has a twice longer exciton diffusion length and therefore assumedly also longer charge carrier lifetime and diffusion length [80].

Exposure of certain crystal facets on the surface plays an important role in the photocatalytic activity of semiconductor material. High surface energy facets are more active towards photocatalytic reactions due to the high amount of under-coordinated Ti and O atoms [82]. However, as they are thermodynamically less stable than low surface energy facets the later usually dominates at the end of the growth process [82]. Anatase belongs to tetragonal crystal system and according to the Wulff construction, slightly truncated tetragonal bipyramid is thermodynamically most stable anatase crystal shape (*Figure 6b*) [83], [84]. It is mostly built up with 101 facets (more than 90 %) and 001 facets (less than 10 %). Surface energies of different anatase facets are listed on the *Table 2*. By controlling the surface termination, it is possible to control the shape of anatase crystal. For example, in basic conditions (oxygenated surfaces) anatase crystal becomes elongated and the so-called “belt” with 100 and 010 facets is formed (*Figure 6c-d*) [85]. Due to the difference in adsorption energy of different facets, capping agents are used, that will selectively adsorb on high surface energy facets, therefore stabilizing them and enabling them to grow [86].

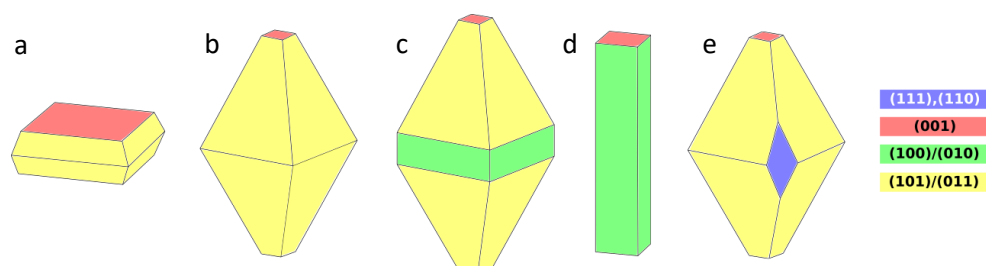


Figure 6. Shape of anatase crystals.

Table 2. Anatase facets and representative surface energies.

Facet	(111)	(110)	(001)	(100)/(010)	(101)/(011)
Surface energy (J*m ⁻²)	1.61 [86]	1.09 [87]	0.90 [88]	0.53 [87] [88]	0.44 [88]

Anatase facets differ from each other not only by surface energy but for example also from other properties, like optical band gap value. For 001, 101, 010 and 111 facets band gaps of 3.01, 3.04, 3.08 and 3.17 were measured accordingly [86]. Although the 111 facet has the highest band gap, it has the highest conduction band minimum and can therefore generate more reductive electrons to take part in the photocatalytic reaction [86], [89]. Another phenomenon to mention here is the peculiar oxidative and reductive properties of the facets [90]. Kim, et.al. found that the transport of the electrons from the bulk is 3.95 times faster towards the 101 facet compared with the 001 facet and the transport of holes is 3.8 times faster in the direction of the 001 facet [91]. Due to better oxidative properties is the 001 facet more attractive as a photoanode compared with the 101 facet. To reproducibly synthesize high energy anatase facets is still a challenge.

For water-splitting applications, crystalline TiO₂ has gained more interest than the amorphous counterpart due to lower band gap and therefore wider solar spectrum absorption, better charge carrier transport and higher stability in aqueous solutions. However, amorphous TiO₂ has shown to be efficient protection layer for photoanodes that are more expensive and/or less stable than TiO₂ [54], [92], [93]. Amorphous TiO₂ has supreme hole conductivity [75], a thin layer is transparent and it is economically more feasible to produce than the crystalline TiO₂. Although anodic corrosion potential for TiO₂ at pH 0 is more positive than the oxygen evolution reaction (OER) [94], care should be taken since in real systems overpotential is needed to drive the OER which can lead the operating potentials close to the edges of TiO₂ theoretical stability window in the Pourbaix diagram.

2.4 Scanning probe microscopy

Scanning probe microscopy is a powerful tool which allows us to study the morphology as well as local electrical and mechanical properties of a sample with high spatial resolution. The main components of a SPM are a nanoscale size probe which interacts with the sample surface and a piezoelectric scanner which controls the probe/sample (x,y,z) position. According to the type of interaction between probe and sample, SPM has two main operating modes – scanning tunneling microscopy (STM) and atomic force microscopy (AFM).

STM was invented by Swiss scientists Gerd Binnig and Heinrich Rohrer in 1981 [95], [96]. The interaction between the sample and STM probe is the tunneling current. Two main working modes are based on keeping the constant current or constant height between the sample and the probe. With the first mode, the change in probe height is measured and with the later, the change in tunneling current is detected. As STM is rather challenging to use for investigating samples with low electrical conductivity, especially in ambient conditions, mostly AFM is used to study semiconducting or insulating materials.

2.5 Atomic force microscopy (history, operation principle)

Based on STM theory, AFM was invented by Binnig, et.al. in 1986 [97]. AFM allows to study conductive, semiconductive as well as insulating materials. The basic AFM working principle is illustrated on *Figure 7*. The laser beam is aligned with the end of the cantilever and is reflected from the cantilever onto the photodetector. Attractive and repulsive forces between the tip and the sample surface cause the cantilever to bend towards or away from the sample movement of the reflection of the laser spot on the photodiode. The photodiode consists of four independent segments which will produce a voltage signal when the laser spot shines on them. This voltage signal is introduced to a feedback system which keeps the cantilever deflection constant by applying a voltage to the piezo. The piezoelectric ceramic will change its geometry when the voltage is applied and therefore the applied voltage is a measure of the height of the morphological details on the sample. Interactions between an AFM probe and a sample depend on the distance between the two and can be attractive for distances above 0.5 nm and repulsive for distances below 0.3 nm [28]. The exact value of the force can be calculated using Hook's law [98]:

$$F = -kx$$

where k is cantilever spring constant and x is cantilever displacement. Forces as low as pico-newton can be detected with AFM.

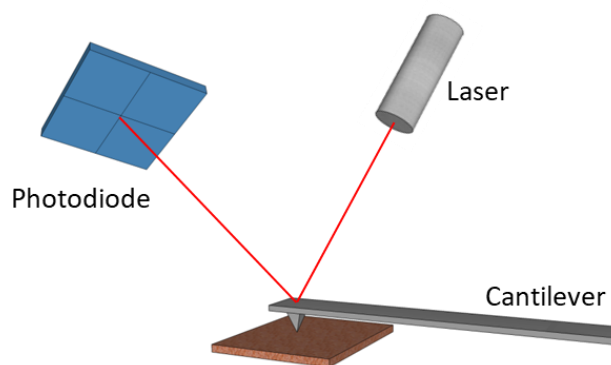


Figure 7. Basic working principle of AFM.

Table 3. Main forces that occur between the AFM tip and the sample [99].

Long-range forces (attractive)	Short-range forces (repulsive)
Van der Waals forces	Pauli repulsion
Capillary forces	Ionic repulsion
Magnetic forces	Chemical forces
Electrostatic forces	

2.5.1 Imaging modes

There are different imaging modes available when using AFM. Choosing an imaging mode depends on the type of the sample, probe and the information one aims to receive.

Contact mode AFM

As the probe is raster-scanned across the sample, the tip is in a continual contact with the sample. A feedback system keeps the cantilever deflection constant by adjusting the vertical piezo. Soft samples, e.g. biomaterials, are not suitable for studying with contact mode AFM because of the mechanical load that the samples receives. Care should also be taken when choosing the probe, as it also wears during the measurement and therefore, coated probes are not the best choice.

Non-contact mode AFM

As the name already suggest, the tip does not contact the sample when using non-contact mode. The cantilever is oscillating in the attractive regime close to the sample surface. There are two different possibilities to use non-contact AFM – amplitude modulation and frequency modulation. In the first, the cantilever oscillates above its resonance frequency and in the later at its resonance frequency. A feedback loop is keeping the oscillation frequency or amplitude constant by adjusting the distance between the probe and the sample. Non-contact AFM is ideal for soft and delicate samples. Although, when measuring in ambient conditions samples are covered with a (thin) water layer and this forms a meniscus between the sample and the probe. The meniscus causes the probe to stick and therefore results in low-resolution imaging [100].

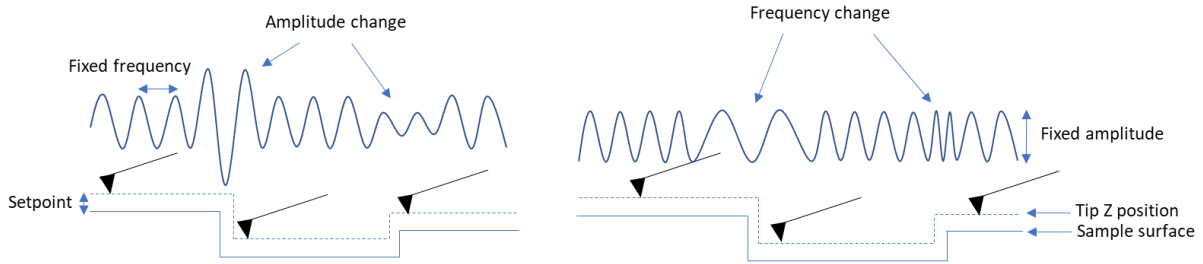


Figure 8. Basic principle of amplitude modulation (left) and frequency modulation (right) non-contact AFM. Adapted from [101].

Tapping mode AFM

In tapping or intermittent contact mode AFM, the cantilever oscillates near its resonance frequency. Amplitude and frequency are both kept constant using a feedback loop. Tapping mode uses much higher cantilever oscillation amplitude, in the range of 100-200 nm, compared with non-contact mode where the amplitude is in the range of 10 nm. As the probe gets closer to the sample surface, oscillation amplitude is decreased. The feedback system adjusts via the piezo drive the height of the cantilever to maintain constant oscillation amplitude.

Peak-force tapping mode AFM

Peak-force tapping (PFT) is the latest AFM imaging mode. In this mode the probe is oscillated at 1 – 2 kHz which is much lower than the cantilever resonance frequency. During the oscillation the tip periodically touches the sample surface with a user defined force (peak force), which will be held constant by applying Hook's law and the feedback system. PFT mode has several advantages over the previously mentioned imaging modes. It helps to protect the tip/sample damage as well as enables to receive mechanical data simultaneously with topography by analyzing the force-distance curves which will be generated for each tap. The spring constant of the cantilever needs to be suitable for sample hardness, e.g. harder samples require cantilevers with a higher spring constant. The peak force setpoint needs to be high enough for sufficient sample deformation (ca. 1-2 nm indentation, see *Figure 9b*) in order to get the proper tracking (approach and retrace curves align) of the sample surface.

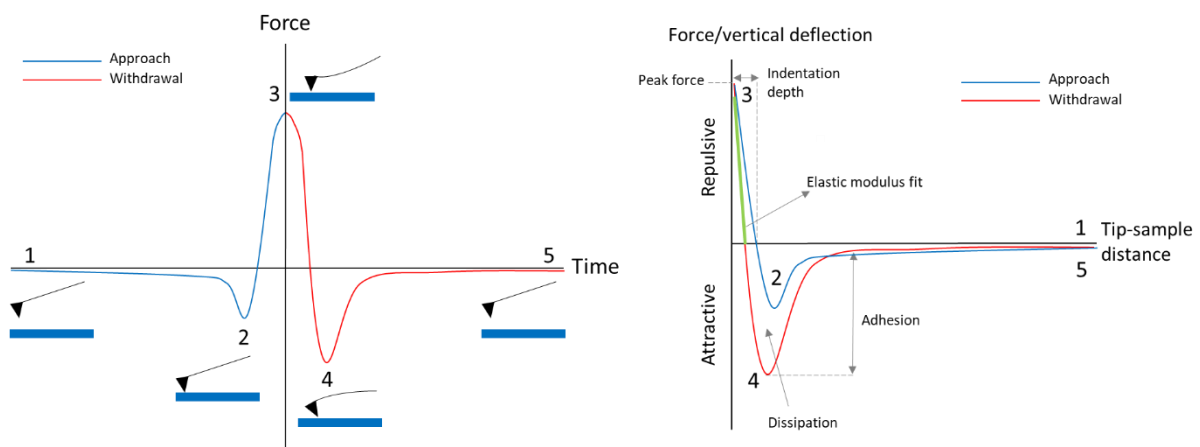


Figure 9. Peak force tapping curve (a) and force-distance curve (b) obtained for each pixel. Adapted from [102].

The resolution of the AFM image depends on several aspects. The main limitation for the vertical resolution is the thermal noise of the cantilever oscillation [103]–[105]. The amplitude of the thermal noise Δz is expressed as [105]:

$$\Delta z = \sqrt{\frac{4k_B T}{3k}}$$

where k_B is Boltzmann constant, T is absolute temperature and k is cantilever spring constant. As the Δz depends on absolute temperature and spring constant, thermal noise is reduced when working at lower temperatures and with stiffer cantilevers.

Lateral resolution is mostly limited by the end radius of the tip. Size and the geometry of the tip are in general the most crucial features for high resolution imaging. Another important parameter is the number of data points the system is told to record. As already mentioned, AFM imaging is done in raster scan mode which consists of forward and reverse scan lines called as trace and retrace. The number of measurement points per each scan line is limited by the end diameter of the probe. The step size between the two recorded pixels should be larger than the tip end diameter to avoid duplicated data points. The typical number of scan lines and pixels per line stays between 32 and 1024. This creates a matrix data file with 32x32 to 1024x1024 elements.

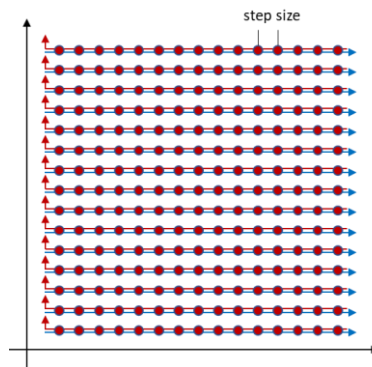


Figure 10. Schematic of the raster scan imaging mode. Blue lines indicate trace and red lines retrace scan direction. Adapted from [106].

2.5.2 Artifacts and processing of AFM images

In order to receive high quality data using AFM, it is crucial to recognize image artifacts. Distinguishing image artifacts from the real data helps to avoid misinterpretation. Primary sources for AFM image artifacts come from *i)* scanner, *ii)* probe, *iii)* external and internal noise, and *v)* surface contamination.

Scanner artifacts

Hysteresis

The main component of the AFM scanner is the piezoelectric ceramic which extends and contracts when applying bias. When applying linear bias, the response is non-linear. This is because the piezo scanner is more sensitive and moves more per voltage at the end of the scan line than at the beginning. This causes hysteresis between trace and retrace scanning directions. Hysteresis of piezoelectric ceramic causes edge overshoot artifacts which look like small hills and valleys at the edge of surface structures [107]. Reducing the scan speed helps to reduce the effect of hysteresis.

Thermal drift and piezoelectric creep

AFM is susceptible for even a small change in temperature. Thermal drift causes image distortion which is clearly noticeable when scanning samples with straight line features. These features appear to be bended instead of straight in the presence of thermal drift. To avoid artifacts caused by the change in temperature, thermal equilibrium should be reached before the imaging or by using faster scan rates.

Artifacts caused by piezoelectric creep look very similar to thermal drift but have completely different origin. Large variations in DC offset voltages introduced to the piezo cause the scanner to change its position. Most of the change is done in less than a millisecond and the rest of the displacement is done in longer time scale. The drift of the piezo displacement is called creep. Usually, the creep settles out during one scan, therefore it is suggested to capture the next image when creep artifacts appear.

Bow and tilt

An AFM scanner is built to be attached to a microscope body from one side and having a free end at the other side. This causes scanner movement following the arc shape instead of being planar. An artifact caused by arc shape movement is called bow effect and it is more striking when using large scan size. When the probe and the sample are not perpendicular to each other, large planar background is recorded also known as tilt. Only a few degrees deviation from planar placement of the sample causes tilt on the AFM image. Bow can be avoided when decreasing the scan size, but tilt is rather difficult to prevent. Nevertheless, bow and tilt can be removed by using image processing functions called flattening or plane fit. Different functions for data processing will be described in the next section.

Probe artifacts

Tip-sample convolution

Tip-sample convolution causes protruding objects to appear larger and voids appear smaller. This is an artifact that cannot be fully removed. Features that have similar or smaller radii than the tip will have the highest convolution effect. The smaller the tip radius, the smaller is the probe convolution effect. In addition to the end radius, also the height as well as the front, back and side angles of the tip can have a significant impact to the veracity of the AFM image.

Blunt or contaminated tip

If unexpected features are repeating all over the image it is most probably due to contamination of the tip. It can be rather difficult to notice when imaging unknown sample. For the verification, a reference sample or a sample with known features should be scanned. Contamination can be removed by using false engage (probe “engages” further away from the sample surface) and increasing the gains which will cause piezo and hereby also cantilever to oscillate. Another possibility would be to use a large scan size and high scan rate and thereby mechanically removing the contamination. The latter is rather audacious as it can wear the tip.

Blunt or dull tips will result in low image resolution. Compared with a non-degraded tip, the image looks blurry, features appear larger and smoother. In order to avoid tip wearing, scanning parameters should be chosen with extra care.

Double tip

Features on the image emerge double and blurred. It appears as each feature on the sample surface has an identical twin right next to it. With data processing functions there is a possibility to restore convoluted and blurred images. Wang, et.al. introduced deblurring model based on Bayesian framework to restore double-tip artifacts [108]. As it is not always possible to carry out automatic algorithms, it is rather time-consuming process, therefore, it is wise to invest time to choosing proper scanning parameters.

Optical interference

A poorly aligned laser can spill over the edge of the cantilever and reflect back from the sample. If this reflection interferes with the incident laser light, it creates a sinusoidal pattern on the image [109].

This artifact is more pronounced when using probes with a small cantilever and highly reflective samples. To avoid optical interferences, the laser should be realigned and moved towards the back of the cantilever.

External and internal noise

High frequency ringing

When the cantilever is oscillating at higher frequencies than the resonance frequency, ring-like features may appear on the image. Reducing the drive frequency should resolve the problem.

Vibrations

AFM is very sensitive to any environmental disturbances. Mechanical and acoustic-caused probe vibrations cause artifacts on the AFM images. Usually, long line across the whole image can be observed.

Surface contamination

Although sample preparation for AFM imaging is, compared to many other techniques like TEM, EBSD rather simple, care should be taken nonetheless by removing loose debris on the sample surface. The tip starts to drag the contamination with it and therefore creates a blurred image with streaks on it. In the worst-case, contamination can break the tip.

Processing AFM images

As mentioned above, there are artifacts that are difficult avoid, e.g., tilt and bow, therefore almost all AFM topography images require post-processing of the data. Most frequently used commands are Flatten and Plane Fit. Flatten uses all unmasked scan lines to calculate least-square fit polynomials for each line and then subtracts them out. Depending on the order of polynomial applied it is possible to eliminate tilt, bow and low frequency noise. Flatten polynomials are:

- 0th order - centers data along each line
- 1st order - centers data and removes tilt on each scan line by calculating and removing offset and slope
- 2nd order - centers data and removes tilt and bow on each scan line by calculating second order least-square fit and then subtracting it from the scan line.
- 3rd order – same as the 2nd order except that third order least-square fit is calculated

Instead of calculating least-square fit polynomial, plane fit uses single polynomial function and subtracts it from the image. It can be applied to either X, Y or to both directions. The purpose of each plane fit order is similar to flatten command order:

- 0th order - centers data
- 1st order - removes tilt
- 2nd order – removes 2nd order bow
- 3rd order – removes 3rd order bow

There are many other data processing models which include Gaussian, lowpass, median, etc. filters. These are not further discussed here as in this work mostly flatten and plane fit commands are used.

2.5.3 Electrical modes

Conductive AFM

Conductive AFM (CAFM) measures the current flowing between the conductive AFM probe and the sample simultaneously, together with topography. A voltage difference between the probe and the sample is established by applying a DC bias to one of them, and as a result current will flow from tip to sample or vice versa. This current is guided through linear preamplifier which converts the current signal into digital voltage signal.

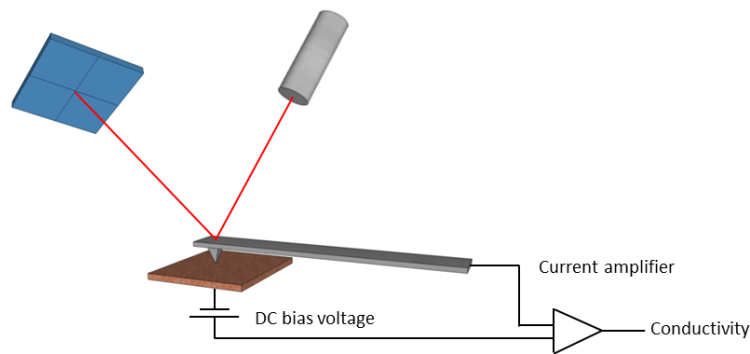


Figure 11. Schematic of a basic conductive AFM setup.

Tunneling AFM (TUNA) works similarly to CAFM but can measure ultra-low currents in the range of $<1\text{pA}$ to nA compared with CAFM which detects currents in the range of $<\text{nA}$ to μA . This is due to more sensitive amplifier and therefore is more suitable for samples with low conductivity. The bandwidth of the PF-TUNA module is 10 times greater than PF tapping frequency and this helps to precisely collect the current data with each tapping with high signal-to-noise ratio. To increase the tip and sample contact time for better electrical contact, 1 kHz PF tapping frequency is used instead of 2 kHz.

Combining TUNA with PF tapping imaging mode, local electrical properties simultaneously with topography and mechanical properties can be received. With PF-TUNA there are three different kind of current information available: peak current which occurs at maximal force (point nr 3 on *Figure 9a*), contact current during the points 2-4 on *Figure 9a* and TUNA current which is cycle average current (points 1-5 on *Figure 9a*).

As already mentioned, choosing the AFM probe is one of the key factors that determines the image resolution. For conductivity measurements mostly Pt or Au coated probes or highly doped SiN probes are used, with the later having lower conductivity but better durability than the coated probes. Mechanical wear of the conductive coating and melting of the tip varnish are two main reasons for low quality conductivity maps. When conducting measurements in air, one also needs to take into consideration local anodic oxidation of the sample surface.

Spectroscopy mode CAFM

In addition to current maps, CAFM can also be used in spectroscopy mode. In this mode the sample bias is ramped and local current-voltage (I-V) curves can be recorded at the probe-sample nanojunction. When capturing I-V curves at a given position on the sample surface, the feedback is changed to contact mode, in order to keep the cantilever deflection constant. Recently, Bruker has introduced the so called DataCube mode, which enables acquisition of I-V curves for each tapping pixel during peak force imaging. Its working principle is similar to peak force tapping mode (see *Figure 9a*), with the main difference being that now the peak force is held for a period of time, called the "hold

segment", and ranging from μs to ms , during which the bias is ramped and the resulting current is measured (Figure 12a-b). Topography simultaneously with I-V curves at each pixel, as well as mechanical properties, can be recorded in this way.

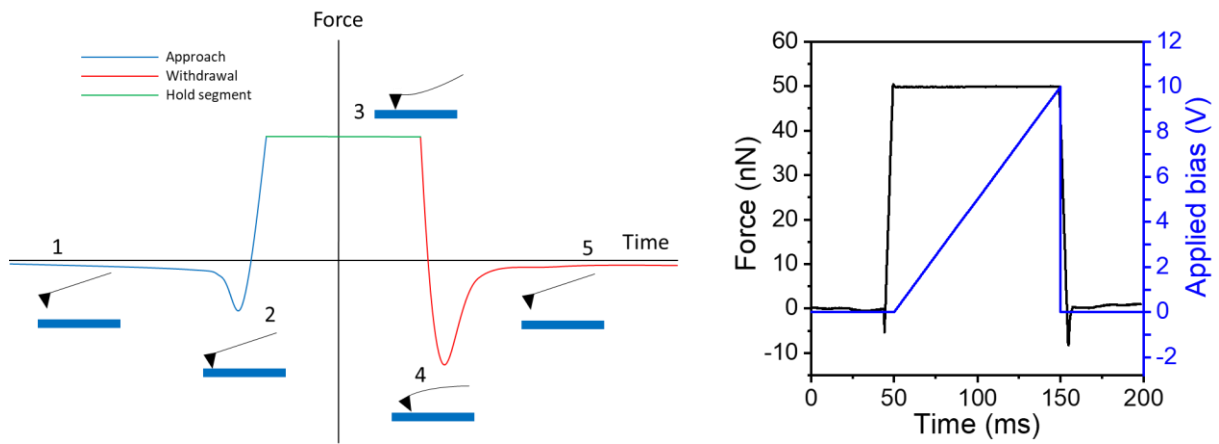


Figure 12. a) one tapping cycle for simultaneous measurement of topography and I-V curves, b) potential ramping during one tapping cycle.

Kelvin probe force microscopy

Kelvin probe force microscopy (KPFM) is an advanced AFM technique that measures contact potential difference (CPD) between a sample and an AFM probe. The conventional Kelvin probe method was developed in 1861 by Scottish scientist Lord Kelvin [110]. It is a non-contact and non-destructive technique to measure the surface potential by measuring the CPD. Simplified scheme of the CPD formation and detection is displayed in Figure 13. When two materials are brought into electrical contact, electrons will flow from the one with lower work function to the one with higher work function, equalizing the Fermi energies. As the Fermi levels are equalized difference in vacuum levels is established. The system attempts to nullify the change in vacuum levels by applying DC bias (V_{DC}) to the tip while grounding the sample. The CPD equals the absolute value of the applied V_{DC} , but is of opposite sign.

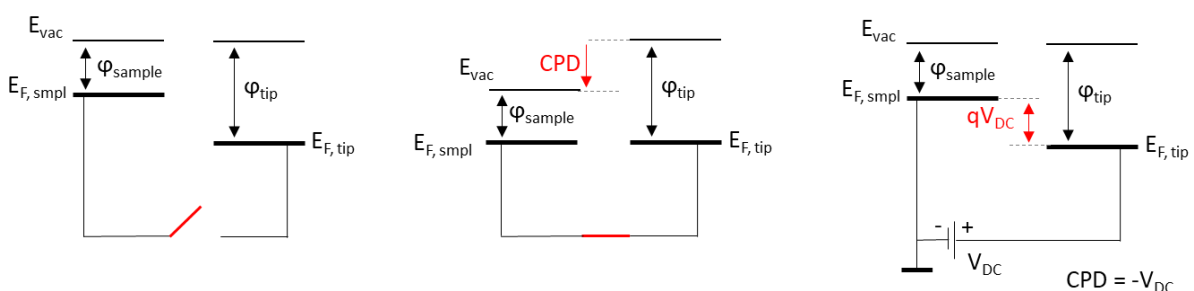


Figure 13. Simplified diagram of the CPD formation between the tip and the sample. Adapted from [111].

The advantage of KPFM over conventional Kelvin probe method is high lateral resolution of CPD map as well as simultaneously recorded high resolution topography. Using a probe with calibrated work function it is possible to measure the work function of the sample by using the equation:

$$CPD = \frac{\varphi_{tip} - \varphi_{sample}}{-e}$$

where the φ_{tip} and the φ_{sample} are the work functions of the tip and the sample and e is the elementary charge. Since the work function is very sensitive to impurities, humidity, etc. on the surface, the measurement needs to be done in a vacuum in order to receive a correct value of the work function.

KPFM can be operated in the so-called dual pass measurement mode in which high resolution topography is recorded with the first pass, then the probe is lifted to a certain lift height (usually 50-100 nm away from the sample to prevent tip damage) and a second pass will be carried out to measure the CPD. In this work topography was measured using the peak force tapping mode. The second pass to detect the CPD is done in the non-contact AFM working modus, which already mentioned above, has two possibilities: amplitude and frequency modulated working modes (Figure 8). With the former, the electric force and with the latter, electric force gradient between the tip and the sample is used to measure the CPD.

Since there are numerous different forces affecting interaction between the probe and the sample (Table 3), electrostatic force, which is relevant for CPD measurement, needs to be separated from the others. In order to do so, an additional AC voltage (V_{AC}) is applied to the probe. The V_{AC} causes the cantilever to oscillate at frequency ω (close to the cantilevers resonance frequency), which modulates the electric field. Feedback loop applies the V_{DC} to nullify the oscillation induced electric force. The electric force between the sample and the tip can be expressed as [112]:

$$F_{el} = -\frac{1}{2} \frac{\partial C}{\partial z} (V_{DC} - \Delta V + V_{AC} \sin(\omega t))^2$$

where C is the capacitance between the probe and the sample, z is the lift height of the tip and ΔV is the CPD between the sample and the tip. The equation contains itself three components of the electric force [112]:

$$F_{DC} = -\frac{1}{2} \frac{\partial C}{\partial z} \left((V_{DC} - V_{CPD})^2 + \frac{1}{2} V_{AC}^2 \right)$$

$$F_{\omega} = -\frac{\partial C}{\partial z} (V_{DC} - V_{CPD}) V_{AC} \sin(\omega t)$$

$$F_{2\omega} = \frac{1}{4} \frac{\partial C}{\partial z} V_{AC}^2 \cos(2\omega t)$$

The applied V_{AC} voltage causes the electric force to modulate at ω and 2ω frequencies which can be measured with cantilever deflection.

The feedback system tries to minimize the amplitude of the oscillation with frequency ω by adjusting the applied bias voltage. When the bias voltage equals the CPD the amplitude of the oscillation with frequency ω is zero and the electric force is minimized. Measuring the CPD with an KPFM by minimizing the electric force between the tip and the sample is called amplitude modulation KPFM (AM-KPFM). Another option is to use the frequency modulated KPFM (FM-KPFM) which is based on the electric force gradient between the tip and the sample and can be expressed as [112]:

$$\frac{\partial F_{el}}{\partial z} = -\frac{1}{2} \frac{\partial^2 C}{\partial z^2} (V_{DC} - \Delta V + V_{AC} \sin(\omega t))^2$$

and the three components can be written down as [112]:

$$\frac{\partial F_{DC}}{\partial z} = -\frac{1}{2} \frac{\partial^2 C}{\partial z^2} \left((V_{DC} - V_{CPD})^2 + \frac{1}{2} V_{AC}^2 \right)$$

$$\frac{\partial F_{\omega}}{\partial z} = -\frac{\partial^2 C}{\partial z^2} (V_{DC} - V_{CPD}) V_{AC} \sin(\omega t)$$

$$\frac{\partial F_{2\omega}}{\partial z} = \frac{1}{4} \frac{\partial^2 C}{\partial z^2} V_{AC}^2 \cos(2\omega t)$$

When the $V_{DC} = CPD$ the electric force gradient is minimized.

In this work FM-KPFM mode was used for the second pass, as it enables to receive higher spatial resolution than the AM-KPFM.

One of the most valuable information which can be measured with KPFM is the surface photovoltage (SPV) of photoactive materials. The CPD measured in dark CPD_{dark} is subtracted from the CPD measured under illumination CPD_{ill} , this equals the SPV with opposite sign. ΔCPD is the light induced change of the contact potential difference:

$$\Delta CPD = CPD_{ill} - CPD_{dark} = -SPV$$

The formation of SPV on the n-type semiconductor is illustrated in *Figure 14*. Under illumination Fermi energy shifts towards the more cathodic potentials. This shift in Fermi energy upon illumination is equal to the SPV. Under illumination the upward band bending of the n-type semiconductor is reduced as the photogenerated holes move towards the surface and neutralize the negative charge to some extent. Therefore, the SPV is the change in band bending between light and dark conditions. Under illumination the Fermi level splits and forms two quasi-Fermi energies, one for electrons and other for holes. The potential difference between the two potentials corresponding to the quasi-Fermi levels is the maximum voltage that can be extracted from the device. Therefore, the difference between the quasi-Fermi levels needs to be larger than 1.23 eV for water-splitting reaction [25], [113].

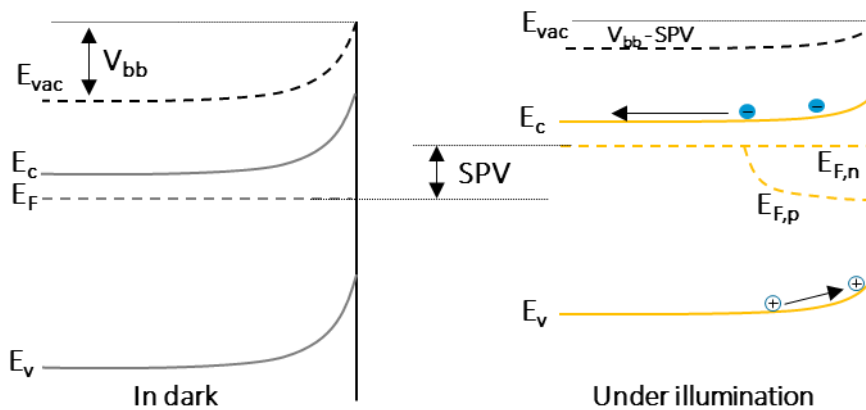


Figure 14. Energy band diagram in dark and under illumination. Figure adapted from [25], [114].

In the ideal system without surface states, the SPV after the illumination immediately returns to its initial value in dark. In the real systems this is not true due to the charging of the defect states upon illumination. Turning off the light the discharging of the defect states can take from seconds to hours [113]–[115]. The areas that remain more positive compared with the initial CPD value in dark reveal the location of the trapped holes and the areas that remain more negative represent the location of the trapped electrons [116]. Presenting CPD as a function of time, dynamic processes like charge-carrier lifetime, recombination and spatial distribution can be observed [113], [116]–[118].

2.6 Electrochemical techniques

Imaging in liquid

Assuring that the AFM scanner is protected from the liquid by using a protective “skirt” attached around the cantilever holder, AFM measurements can be conducted in the liquid media. Combining the AFM liquid cell with a potentiostat it is possible to carry out electrochemical studies inside the AFM cell (EC-AFM). The advantage of EC-AFM in front of conventional EC measurements is the real-time observation of the surface undergoing electrochemical reaction.

Open circuit potential

Open circuit potential (OCP) measurements reveal the position of the Fermi energy of the semiconductor in respect to the reference electrode when no current flows through the system. Upon above-band gap illumination, the Fermi energy of the n-type semiconductor shifts towards the more cathodic potentials and therefore the OCP is more negative than in dark [18]. The change in Fermi levels between the dark and light OCP measurements is called the photovoltage (V_{ph}). By using the saturation light intensity, which means that the OCP remains unchanged when further increasing the illumination intensity, it is possible to estimate the flat-band potential. It is important to find the band flattening intensity in order to avoid unnecessary high intensities that can lead to warming up the sample and thereby the corrosion of the semiconductor.

Drift in the OCP measurement can be indication of a corrosion processes taking place on a semiconductor or a slow adsorption of electrolyte ions to the surface [18].

OCP is often measured in between other (photo)electrochemical studies while it shows whether or not the system has reached a steady-state conditions before continuing with characterization.

Cyclic voltammetry

During the cyclic voltammetry (CV) studies, the potential sweep is periodically switching the direction and the current response is measured. It is possible to achieve qualitative information of the oxidative and reductive reactions taking place on the sample and to locate the redox potentials of electroactive species. CV is a common technic which is conducted before and after other (photo)electrochemical studies in order to observe whether or not the surface has undergone changes. One of the important parameters of the CV measurements is the scan rate (mV/s), which has an effect to the measured current. Faster scan rate leads to an enhanced current due to decreased diffusion layer on the sample [119]. The hysteresis between the two potential sweep directions reveals the capacitive charging at the semiconductor/electrolyte interfaces which increases when increasing the scan rate.

Chopped cyclic voltammograms help to reveal the charge recombination processes in a form of spikes on the current-voltage curve (transient photocurrent). On the n-type semiconductor the recombination is mostly governed from the accumulation of holes on the semiconductor surface as a

result of slow kinetics. The losses in current due to the recombination can be improved by introducing a hole scavenger. If no improvement can be seen, the recombination most likely takes place at the semiconductor/substrate interface [120]. Rate constants of hole transfer (k_{trans}) and recombination (k_{rec}) can be calculated from the ratio of the steady state photocurrent (j_{ss}) and transient photocurrent (j_t) [121], [122].

$$\frac{j_{ss}}{j_t} = \frac{k_{trans}}{k_{trans} + k_{rec}}$$

Chronoamperometry

Instead of periodically switching the direction of the applied potential like in CV measurements, the potential is held constant during the chronoamperometry measurements (CA) and the current is measured versus time. It is often controlled by the diffusion-limited current which is expressed as a (rapid) decrease of the current due to the mass transport limitation of electro-active species near the surface. CA measurements in the dark reveal the magnitude of the current governed from the electrochemical reactions involving the majority charge carriers. Upon illumination the current changes due to the generation of charge carriers and the current is mostly controlled by the photoelectrochemical reactions involving minority charge carriers. Nevertheless, one of the drawbacks of the CA measurement is that it is not selective and the current is a sum of the Faradaic currents governed by all the reactions taking place at a given potential [123].

Similar to the chopped cyclic voltammogram, charge carrier recombination rate and the origin can be studied by performing a chopped CA measurement. CA is more accurate compared with CV since the potential change and capacitive component are absent.

Chronoamperometry is one of the common techniques to study the stability of the sample undergoing the (photo)electrochemical reaction [124], [125].

Tafel extrapolation

Tafel polarization is a widely used method to determine the corrosion rate, current density and potential [126], [127]. Anodic and cathodic potentials versus OCP are applied and the current is measured. For the analysis, the current on a logarithmic scale is plotted against the applied potential. Linear segments of the anodic and cathodic branch extrapolate to the corrosion current density (J_{corr}) as well as the corrosion potential (E_{corr}) (Figure 15) [128]. From the J_{corr} and anodic and cathodic slopes (β_a , β_c) the polarization resistance (R_p) can be calculated which shows the sample resistance to oxidation. The higher the J_{corr} and the more negative the E_{corr} the more prone is the studied sample to corrosion.

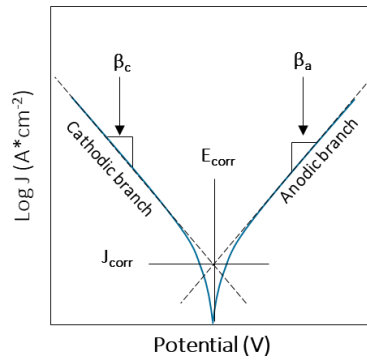


Figure 15. Tafel extrapolation, adapted from [127].

To study the presence of photocorrosion, J_{corr} , E_{corr} , and R_p values are compared between the curves measured in dark and under illumination.

2.7 Atomic layer deposition

Atomic layer deposition (ALD) enables deposition of thin films onto planar and structured substrates with high conformity all over the surface. Due to the conformity even on complex surface geometries and precise control over film growth and composition, ALD is preferred over other vapor phase coating techniques like chemical vapor deposition (CVD) and physical vapor deposition (PVD). Various materials from metal oxides to noble metals that can be deposited using ALD. Usually two precursors, both in gaseous phase, are sequentially introduced in ALD chamber where the self-limiting surface reactions take place. Due to the surface-controlled reactions, only one monolayer of a current precursor will be chemisorbed on the surface and the rest will be removed by purging the chamber with an inert carrier gas. After purging, the second precursor will be introduced and another monolayer will be added. Since individual precursor reactions are considered half-reactions, then the reaction is complete only after introducing the second precursor. One complete reaction is called a cycle, which is repeated until the desired film thickness is achieved. *Figure 16* illustrates the ALD process.

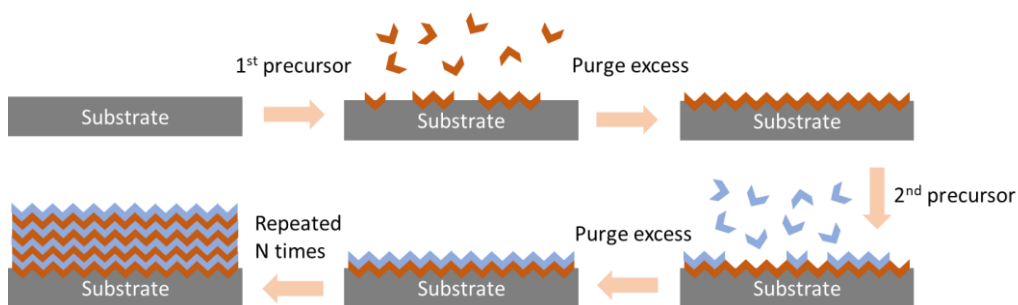


Figure 16. Simplified schematic of the ALD process.

Choosing the deposition temperature depends on the “ALD window” which is presented as film growth per cycle vs temperature. Several aspects like precursor condensation, desorption, decomposition, and reactivity are taken into consideration when constructing the ideal ALD window. Using temperatures lower than the ALD window leads to precursor condensation and/or incomplete reactions whereas too high temperatures result in precursor decomposition and/or desorption. The type of substrate and desired film properties also play a crucial role in choosing the proper deposition temperature. Although ALD has many favorable features, it also has limitations. The main disadvantages are slow deposition

rates, usually between 100 and 300 nm/h [129]–[131]. To produce large samples, the size of the ALD chamber increases as well, leading to even longer deposition times. Nevertheless, in the photocatalyst field where thin films high conformity is required, ALD is an irreplaceable technique.

2.8 Photodeposition

Photodeposition is a facile method to deposit cocatalyst nanoparticles onto a photoactive material. Mostly noble metals (Pt, Ir, Ag, Au, Pd) or metal oxides (RuO_2 , PbO_2) are of interest. A semiconductor is placed in a cocatalyst precursor containing solution and illuminated, no external bias or high temperature is needed. Photon energy needs to be high enough to create electron-hole pairs which will take part from reduction and oxidations reactions. There are two kinds of photodeposition types: a) reductive, during which photo-excited electrons will reduce the metal ions into metallic particles and b) oxidative, in which photo-generated holes will oxidize the metal ions into metaloxide [132]. Although photodeposition itself is a rather easy method, in order to control the cocatalyst particle size, distribution and oxidation state, it requires deeper understanding of photodeposition principles. In the following, some of the main parameters which contribute to the optimization of photodeposition process are shortly discussed.

a) Cocatalyst precursor concentration

Precursor concentration has a strong effect on deposition rate, which is higher when using higher concentrations. Too high deposition rate leads to an uncontrollable nanoparticle size and distribution.

b) Deposition time

Longer deposition time results in higher coverage of the sample with metal nanoparticles, whether forming a film or growing larger particles.

c) Solution pH

Solution pH has an effect on the deposited nanoparticle oxidation state. Metallic Pt is obtained when the solution pH is under 5, Pt oxides are formed when pH is higher than 9 and in between pH 5-9, both metallic Pt and Pt oxides are created [133].

d) Sacrificial agents

In order to increase the photodeposition efficiency, sacrificial hole scavengers are used. Mostly organic molecules, alcohols, are used as they have lower oxidation potential than water. Using low sacrificial agent concentration was shown to deposit metal particles with high oxidation state [134]. Higher sacrificial agent concentration helps to obtain low oxidation state metal particles, but it needs to be taken into a consideration that higher sacrificial agent concentrations also lead to higher particle sizes. For depositing Pt nanoparticles onto TiO_2 , mostly alcohols are used as a sacrificial agent [134]–[138]. Photogenerated holes oxidize the alcohol and create alcohol radicals which will be used to reduce Pt ions into metallic Pt.

e) Absence or presence of oxygen in the solution

In the presence of oxygen in the solution the deposition of metal nanoparticles is highly suppressed as the O_2 is a competing electron scavenger [139].

2.9 Electron backscatter diffraction

Electron backscatter diffraction (EBSD) is a scanning electron microscopy (SEM) based method for obtaining information about the orientation of the individual grains, phase, texture, etc. Electron beam is focused on the polished sample, which is tilted 70° in order to increase the contrast of the diffraction pattern. When the electron beam interacts with the sample, electrons are inelastically scattered in all directions. If the electrons leave the sample in a way that they satisfy the Bragg's condition:

$$2d \sin \theta = n\lambda$$

they form two diffraction cones known as Kossel cones. Each family of planes $\{hkl\}$, from which the electrons are diffracted, forms two parallel Kossel cones with an angle between them of 2θ , which are located either side of the plane. Kossel cones intersect with the phosphor screen and create two parallel lines, called band. The image formed with several bands is called a Kikuchi pattern. From the center line of the bands, the interplanar angles are obtained by comparing the angles between the bands with theoretical values from the table [140]. From the interplanar angles, information about the existing planes and directions is obtained. In order to solve the Kikuchi pattern, the position of 5-10 most intense bands is necessary [140].

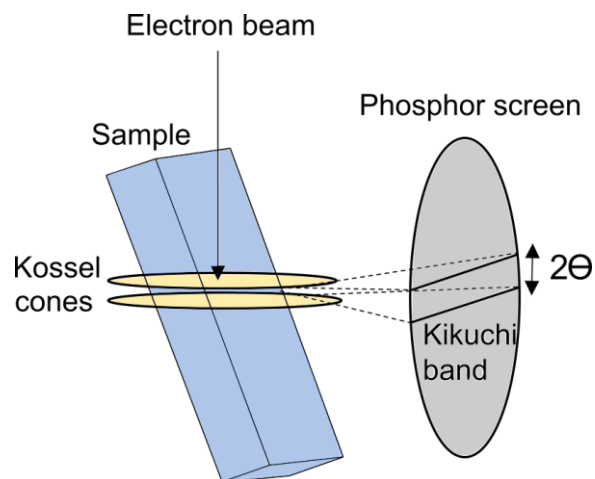


Figure 17. Simplified EBSD working principle and the formation of Kikuchi bands.

A common way to present the EBSD data is by using pole figures. One can imagine a reference crystal with a cubic symmetry placed in the middle of a 3D sphere (*Figure 18a*). Crystal spatial arrangement needs to be fixed by using an external reference point. Normal direction (ND) is towards the Z axes, rolling direction (RD) towards the Y axes and transverse direction (TD) towards the X axes. Passing a straight line through one of the crystal planes, it intersects with a sphere in two diametrically opposite positions [141]. On *Figure 18*, for a simplification, only one direction is presented. By looking on the sphere from the ND direction, a two-dimensional representation of the intercepted locations is received, called as pole figure (*Figure 18b*).

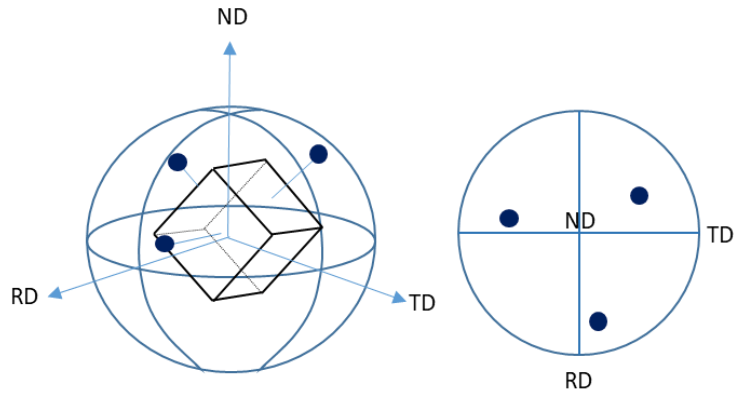


Figure 18. Formation of a pole figure using a crystal with a cubic symmetry. Adapted from [141].

Instead of presenting a certain direction with respect to the ND, RD and TD, an inverse pole figure (IPF) (*Figure 19a*) aligns the orientation with the specific crystal direction [141]. An inverse pole figure is divided into 24 stereographic triangles with a standard unit triangle highlighted with black borders. This triangle is used to construct and read the EBSD orientation maps.

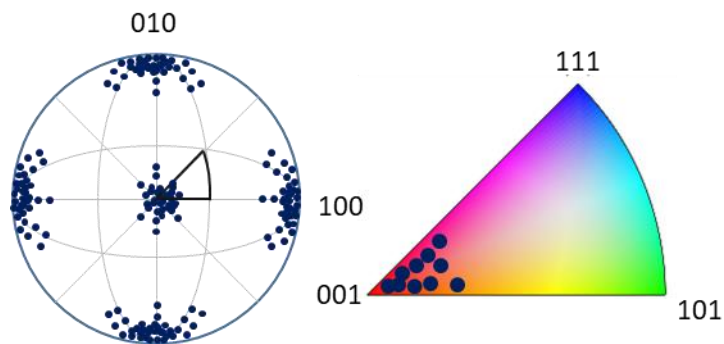


Figure 19. Inverse pole figure looking from the 001 direction and a standard unit triangle used as a color key to read the IPF maps. Adapted from [141].

3. Experimental

Atomic layer deposition

This work makes use of several AFM-based methods for the investigation of a series of TiO₂ thin film samples deposited by atomic layer deposition, at a growth temperature of 300 °C, and using Tetrakis dimethyl titanium (TDMAT) and oxygen plasma as precursors. The substrates used are n⁺⁺ doped (100) silicon wafers (5 mOhm cm, Siegert Wafer GmbH). Prior to the deposition process, the substrates were cleaned by sonication in ethanol and ultrapure water, followed by the removal of the native SiO₂ layer in HF:NH₄F (1:6) solution. For nominal thicknesses of 10, 20, 30, 40, 50, 75 and 100 nm, the corresponding number of ALD cycles was 180, 360, 540, 720, 900, 1350 and 1800 respectively. The samples investigated in this work were kindly provided by Dr. Herman Kriegel.

Atomic force microscopy

AFM measurements were done using a Bruker Dimension ICON atomic force microscope. Prior to each measurement the deflection sensitivity of the cantilever was calibrated using the thermal tune method. This is based on the detection of the cantilever resonance frequency by measuring its thermal fluctuations with the laser. Since only the static force is considered, a deflection sensitivity correlation factor of 1.08 was applied to compensate the underestimation of the dynamic motion amplitude. For the measurements in liquid, thermal tune was performed in the same media as the measurements.

After the measurements each AFM topography image was processed by flattening or plane fit in order to remove the background tilt on each line.

High-resolution topography

High-resolution topography images were obtained using PEAKFORCE-HIRS-SSB probes (Bruker) with nominal tip radius of 1 nm, spring constant of 0.12 N/m and resonance frequency of 110 kHz. Low peak force of 350-500 pN as well as low tip velocity of 3.32 μm/s were used.

(Photo-)current mapping

Electrical contact of the sample to the chuck was achieved by scratching the back of the substrate with a wafer scribe, applying a small amount of Gallium-Indium eutectic, pressing the sample on a metal plate with Kapton tape, and positioning the metal plate carrying the sample on the AFM sample holder. TUNA current measurements were conducted using SCM-PIT-V2 probes (Bruker) with nominal tip radius of 25 nm, spring constant of 3 N/m and resonance frequency of 75 kHz. A peak force of 100 nN was applied, and the tip velocity was set to 5.00 μm/s. During current measurements, a DC bias of +2.0 V was applied to the sample. Samples were illuminated using fiber-coupled LED light source (Thorlabs M365FP1) with 365 nm nominal wavelength, irradiance of 11.46 W/m² and fiber-optic angle of incidence of 10°.

Platinum photodeposition (with methanol and ethylene glycol)

Platinum photodeposition on fully crystalline TiO₂ sample was conducted in a commercial PEC cell (Zahner Elektrik GmbH) with a quartz window, and without counterelectrode. 0.1 mM chloroplatinic acid hydrate (Sigma Aldrich) with 20 % methanol (Acros Organics) or 20 % ethylene glycol (Sigma Aldrich) solution was used to photo-deposit platinum nanoparticles. Deposition time was 2.0 to 2.5 minutes, simulated sunlight (AM1.5G) was used for illumination and the solution pH was 3.65 (at 21.5 °C). Before and during the photodeposition, the solution was purged with argon. After the deposition samples were rinsed with MilliQ water and dried with nitrogen flow.

Electron backscatter diffraction

EBSM measurements were carried out using an SEM from Zeiss Company coupled with an EBSM e-flash^{HR} detector from Bruker and the Esprit 1.94 software. All measurements were taken at a working distance of ~16.1 mm, using an acceleration voltage of 20 kV and a beam current of 10 nA. Scans were performed with a step size of 75 nm on a 400 x 300 pixel grid with individual patterns of 160 x 120 pixels and exposure times of 18 and 18.5 ms. These measurements were carried out at the Bundesanstalt für Materialforschung und –prüfung, see acknowledgments below.

Spectroscopy mode CAFM

Measurements were repeated with two different probe materials: Au coated probes (HQ:NSC18, MikroMasch, tip end radius < 35 nm, spring constant 2.8 N/m, resonance frequency of 75 kHz), as well as Pt coated probes (SCM-PIT-V2, Bruker, tip end radius < 25 nm, spring constant 3 N/m, resonance frequency of 75 kHz). A peak force of 150 nN was applied at each position (x, y) on the sample surface and held for 100 ms ("hold segment"), during which a sample bias from 0 to 8 V was applied and the current through the metal-tip/semiconductor nanojunction was measured. 260 measurement points were recorded during the hold segment. Measurements were performed in the dark as well as under illumination. The sample electrical contact and illumination conditions were the same as those used for current mappings. For analysis, I-V curves were fitted with the current-voltage relationships corresponding to different conduction models shown in *Table 1* using non-linear least squares, with the Levenberg-Marquardt algorithm for minimization (as implemented in the SciPy Python library).

Before and after the DataCube measurements, the electrical conductivity of the probe was measured on the freshly cleaved HOPG. A sample bias ramping from -250 mV to +250 mV and peak force setpoint of 25 nN was used, and 32 I-V curves were captured for each measurement. Curves were plotted and the magnitude of the current was compared between curves captured before and after the measurements on the TiO₂ sample.

Surface voltage mapping

Highly doped silicon nitride probes (PFQNE-AL, Bruker) with nominal tip radius of 5 nm, spring constant of 0.8 N/m and resonance frequency of 300 kHz were used for KPFM measurements. The peak force set point was 3 nN and the tip velocity 5.00 μm/s. The lift height during the potential measurements was varied between 30 nm and 50 nm, and the drive amplitude was 200 mV. Drive routing was set to "sample" for the interleave mode. With this configuration, the CPD of an n-type semiconductor shifts to more negative values under illumination. Samples were illuminated using fiber-coupled LED light source (Thorlabs M365FP1) with 365 nm nominal wavelength, irradiance of 11.46 W/m² and fiber-optic angle of incidence of 10°.

Corrosion studies in AFM-EC cell

For samples that had undergone photoelectrochemical tests in a PEC cell, *ex-situ* high-resolution AFM topography images were obtained with a Bruker Dimension ICON atomic force microscope (AFM). Measurements were conducted in air using PEAKFORCE-HIRS-SSB probes (Bruker) with nominal tip radius of 1 nm, spring constant 0.12 N/m and resonance frequency 110 kHz. Low peak force of 350-500 pN as well as low tip velocities from 0.665 to 6.65 μm/s were used. AFM images were processed by flattening (line-by-line least-squares polynomial fit) in order to remove the background tilt on each line.

For AFM imaging during the *in-situ* electrochemical experiments (AFM-EC), PEAKFORCE-HIRS-F-A probes (Bruker) with 1 nm nominal tip radius (spring constant k = 0.35 N/m, resonance frequency f = 165 kHz) were used. An in-house built electrochemical cell (*Figure A. 7*) was studied under

potentiostatic control (CH Instruments model CHI760E bipotentiostat). In a three-electrode system, platinum wires (99.99%, Sigma Aldrich) were used as counter and pseudo-reference electrodes, with the sample surface as working electrode. Gallium-Indium eutectic alloy was applied to ensure ohmic contact to the back of the samples. The electrolyte used was 0.5 M H₂SO₄ (Carl Roth, Germany). The pseudo reference electrode was regularly calibrated against the Ag/AgCl reference electrode. All potentials in this work are reported with respect to the reversible hydrogen electrode (RHE). Tafel polarization curves were also measured in the AFM-EC setup described, at a scan rate of 2 mV/s. Experiments under illumination employed fiber-coupled LED light sources with wavelengths of 365, 565 and 1050 nm (Thorlabs M365FP1, M565F3 and M1050F3). The irradiance for each experiment was determined on the sample position, using an absolutely calibrated spectrometer (OceanOptics USB2000+XR).

Acknowledgments

The sample series investigated throughout this work were synthesized by Dr. H. Kriegel, and the voltammetry curves shown on *Figure 46* are extracted from Dr. Kriegel's PhD work. EBSD measurements were carried out at the Federal Institute for Materials Research and Testing (BAM) by Dr. G. Nolze and Dr. R. Saliwan Neumann. XPS characterization were performed at nanoAnalytics GmbH by Dr. T. Reuter. The ellipsometry mapping shown on the *Figure A. 14* was carried out by Mr. J. Kollmann.

4. Results and discussion

4.1 Physicochemical properties

This chapter describes the study of the morphology and photoactivity of the TiO_2 sample series deposited by atomic layer deposition. Current maps revealed heterogeneities in photocurrent, and the relationship of photoactivity to local height and roughness was explored. Selective platinum photodeposition revealed a possible influence of the crystallographic structure of the sample on the local variations in photocurrent. This was further investigated by correlative studies with AFM and EBSD on fully crystalline TiO_2 samples.

4.1.1 High resolution topography

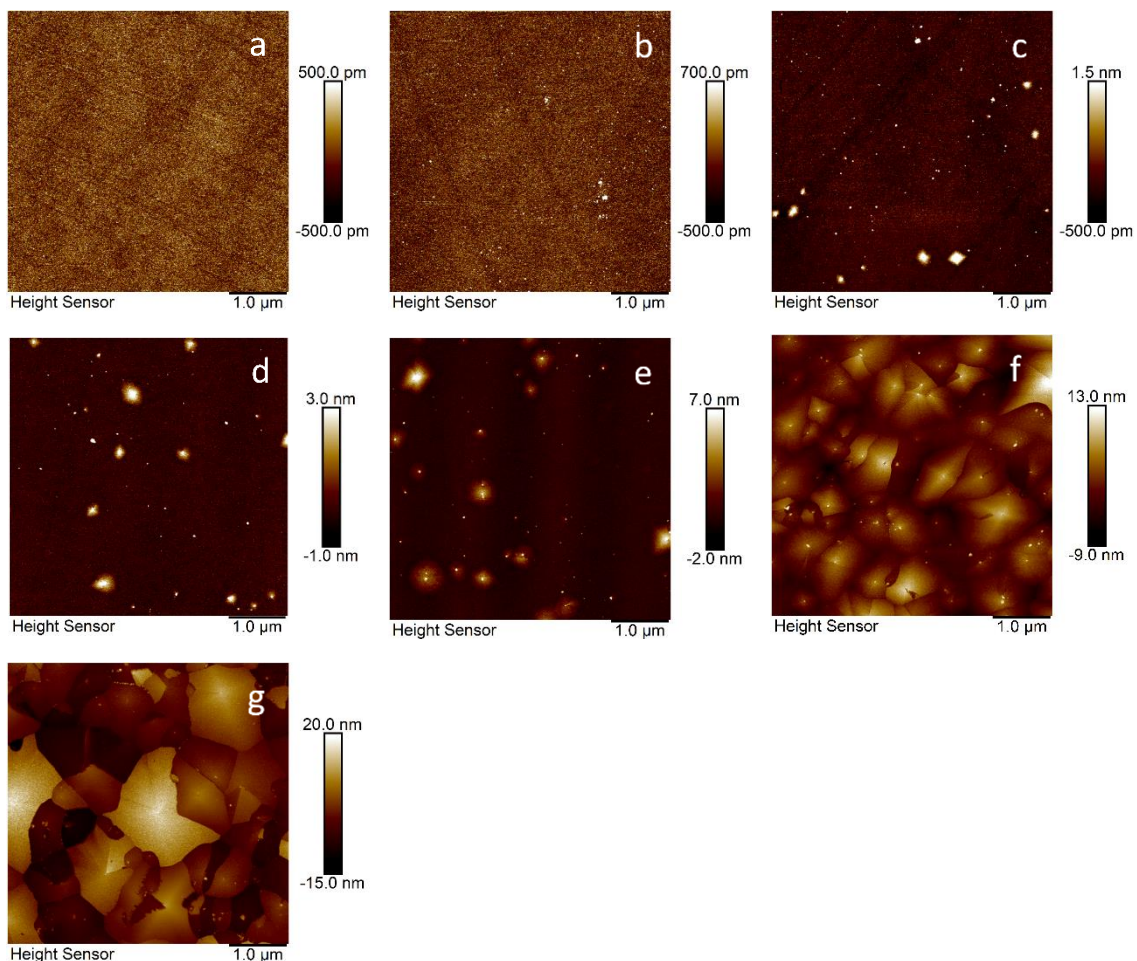


Figure 20. High resolution topography images on the sample series. a) 10 nm, 180 cycles; b) 20 nm, 360 cycles; c) 30 nm, 540 cycles; d) 40 nm, 720 cycles; e) 50 nm, 900 cycles; f) 75 nm, 1350 cycles and g) 100 nm, 1800 cycles.

High resolution topography images on the sample series can be seen on *Figure 20*. While the 10 nm sample (*a*) appears fully amorphous, and the 100 nm sample (*g*) as fully crystalline, the 20 – 75 nm TiO_2 thin films appear as a mixture of both phases (*Figure 20b - f*). While XRD and Raman signals for the crystalline phase can be observed from a film thickness of 40 nm, AFM shows evidence of crystallization already on the 20 nm sample. According to XRD data the crystalline phase formed is anatase [120]. Increasing the number of cycles, the number of these crystalline regions grows, as does

their size. They grow laterally, and gradually come in contact with each other, until the full surface is covered by crystallites. The images show that during the crystallization process of these ALD TiO₂ thin-films, nucleation sites are formed at the surface, and with increasing number of ALD layers these crystallites grow towards the substrate. This was verified by transmission electron microscopy (TEM) on this sample series [142]. Therefore, the tips on top of the hillocks are assumed to be the initial anatase seeds.

Figure 21 illustrates the arithmetic average (Ra) and root mean squared (Rq) roughness as a function of TiO₂ layer thickness. Ellipsometry data was used to estimate the film thickness [120] and the roughness data was taken from the AFM height sensor images presented on the *Figure 20*. As the layer grows from 10 to 50 nm, during which the first crystallites start to form and grow, the increase in roughness is minimal. In the range from 20 nm to 50 nm the average height of crystalline hillocks (*Table 4*: "average particle height") increases only around 1 nm, resulting in a small change in roughness (*Figure 21*). From 50 to 100 nm film thickness, the crystallites grow significantly, and consequently also the Rq and Ra values increase, later reaching from 0.8 % of the film thickness for the 50 nm layer, to 4.9 % for the 100 nm thin layer.

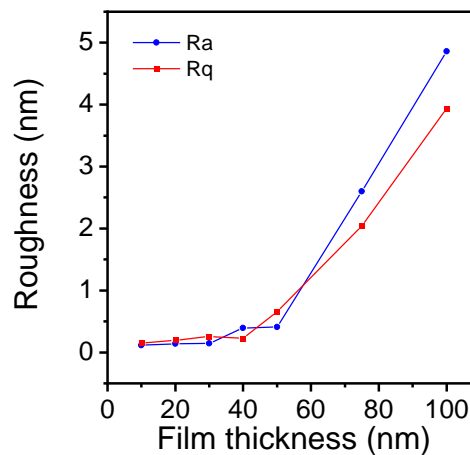


Figure 21. Ra and Rq values for the sample series, taken on AFM images of 5 μm scan size.

The percentage of crystallized area was determined using particle analysis (Bruker Nanoscope Analysis software) which enables the measurement of lateral and vertical dimensions of isolated features identified by height data. Three 5 μm x 5 μm areas (regions of interest, ROIs) were analyzed on different locations on each sample. The threshold height, above which all the features are considered as crystallites, was chosen 0.8, 1.0 and 1.5 nm for the 30, 40 and 50 nm samples respectively. Within each ROI the distribution of areas is rather wide, as new small crystallites are formed, while the existing ones continue to grow laterally. However, across all ROIs on the same sample, the crystalline areas for each ROI, obtained by integration of the crystallite area distributions, show similar values.

The results are presented on *Table 4*. Although the average crystallite height increases about 1 nm per 10 nm of layer growth, the average crystallite area more than doubles by lateral growth, and the total crystallized area increases significantly.

Table 4. Percentage of crystallized area was calculated for 30, 40 and 50 nm sample using particle analysis.

Sample	Average crystallite height (nm)	Average crystallite diameter (nm)	Average crystallite area (nm ²)	Average Crystallized area for all ROIs (%)
30 nm TiO ₂	6.2	115	13 125	0.9 ± 0.01
40 nm TiO ₂	7.4	163	28 190	1.9 ± 0.4
50 nm TiO ₂	8.0	216	61 915	7.0 ± 1.9

4.1.2 Photoactivity variation

Current maps were captured at +2.0 V sample bias in dark and under illumination (Thorlabs M365FP1, wavelength 365 nm, irradiance 11.46 W/m²) on 50, 75 and 100 nm samples. High tip loading force (100 nN) was used in order to penetrate the absorbed water layer and to form mechanically and electrically stable contact between the probe and the sample.

As can be seen on *Figure 22*, for the 50 nm sample (crystallites in a predominantly amorphous matrix) the photocurrent detected in the amorphous regions is one to two orders of magnitude lower than for the crystalline areas. This can be attributed on the one hand, to the higher bandgap required to excite the amorphous fraction [142] as well as the lower carrier mobility in the amorphous material [143]. Furthermore, not all of the crystalline areas embedded in the amorphous matrix exhibit photocurrent. A possible explanation is that, as the crystallization starts on the surface and crystallites grow towards the substrate, the smaller crystalline domains are still electrically separated from the conductive substrate by amorphous material. This has been evidenced on recently reported [142] transmission electron microscopy (TEM) studies on the 40 nm thin film TiO₂ sample of the same sample series.

On the mostly and fully crystalline TiO₂ samples (75 and 100 nm), much higher photocurrents are observed, increasing from the fA range in dark conditions, to the pA range under illumination. A non-uniform distribution of the photoactivity between different crystalline plates can be observed and is further analyzed in the following chapters.

Under illumination, high photoconductivity is also measured at the grain boundaries. Whether the grain boundaries improve or worsen the photocatalytic activity of the polycrystalline TiO₂ is an ongoing debate. Enhancement of the photocatalytic activity has been attributed to the band bending at the grain boundaries that separates the electrons and holes, thereby increasing their lifetime [144]. Other reports claim that grain boundaries act as recombination centers [145] or that charge carriers that move towards the grain boundaries may be trapped in dangling bonds, reducing the photocatalytic activity [146].

We performed platinum photodeposition experiments (see the next section) on the fully crystalline TiO₂ samples, and observed no enhanced deposition on the grain boundaries, compared with the respective neighboring grains. Therefore, for the samples investigated here, the increased photocurrent at the grain boundaries is assumed to be due to the higher electric field on the sharp edges.

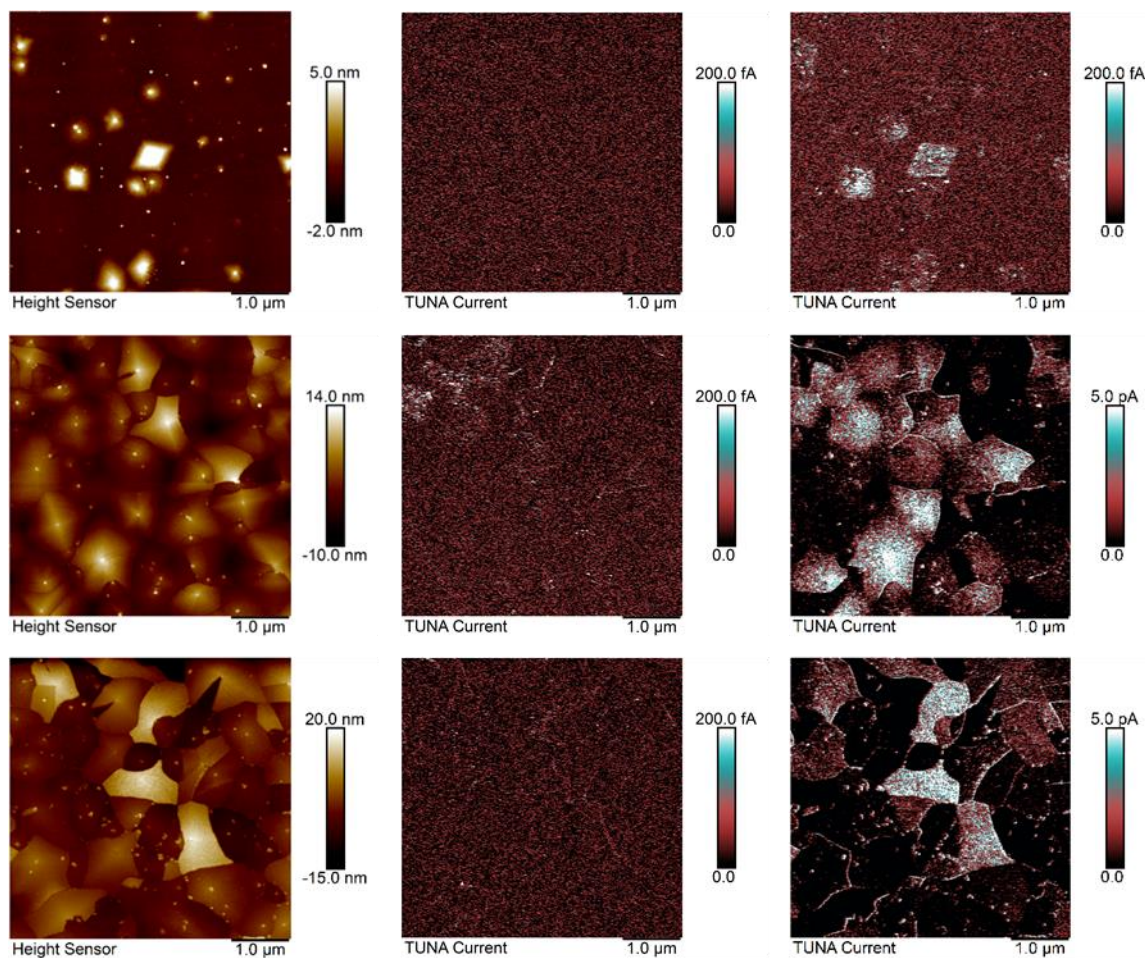


Figure 22. Topography (on the left) and corresponding current maps in dark conditions (in the middle) and under illumination (on the right) on 50, 75 and 100 nm TiO₂ on n⁺⁺ Si.

In order to investigate the effect of morphology on the photocurrent, a series of height and photocurrent profiles were extracted and plotted against each other. As *Figure 23* shows, the higher areas result in higher photocurrents. The feedback loop keeps the cantilever deflection constant during the whole imaging, to ensure that the contact force is the same at every tapping pixel. Therefore, the hypothesis that the difference in current between the lower and higher areas is due to the different contact force on the two areas can be ruled out. While there is a strong correlation between crystallite height and photocurrent, a weak correlation was found between local height and roughness (see *Figure A. 1*).

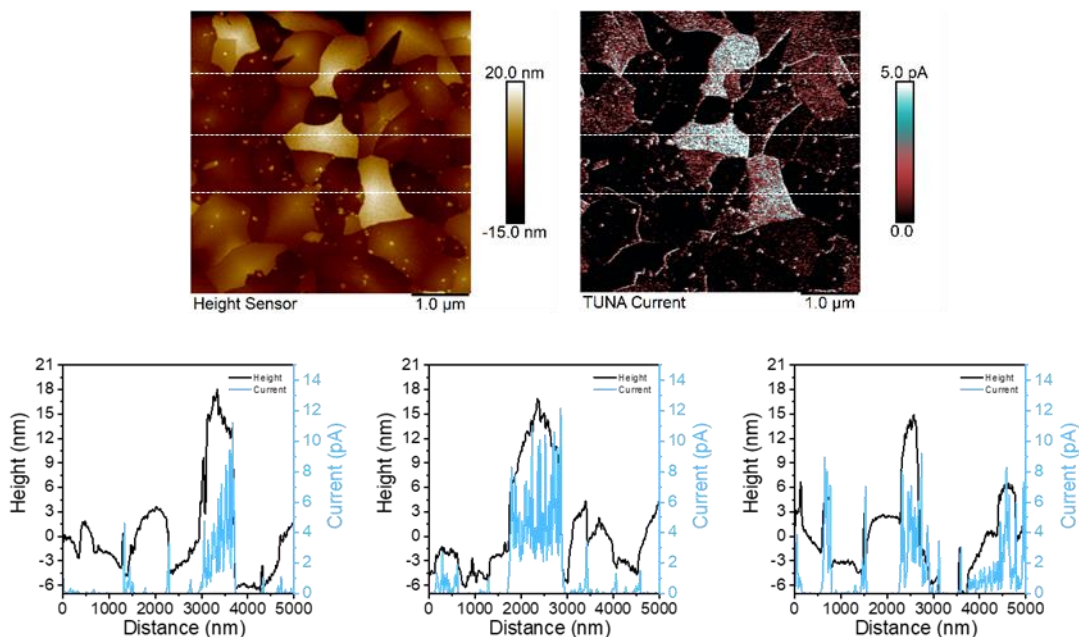


Figure 23. Photocurrent vs height. Cross-sections (top) and representative plots (below).

To quantify the relationship between photocurrent and roughness, local values of both in the same regions were extracted and plotted against each other. *Figure 24* shows that the roughness has a clear effect on the measured photocurrent: higher photocurrent was observed with increasing surface roughness. The shaded area represents the standard deviation of the measurements, which increases at increasing currents. The areas with low photocurrent have a stable current value around zero whereas the areas with high photocurrent have a quite large fluctuations (see *Figure 23*). Increasing the surface roughness is a known method of improving photoelectrochemical performance, mainly by increasing the specific surface area of the interface involved in the photoelectrochemical reaction, and by enhancing light capture through multiple internal reflections [147], [148].

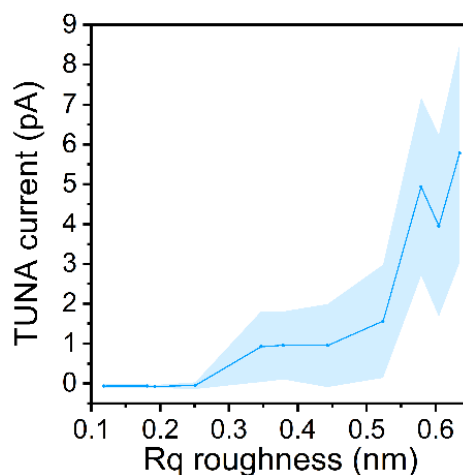


Figure 24. Photocurrent vs roughness. 250 x 250 nm areas on the same positions on the TUNA and Height Sensor map were analyzed.

4.1.3 Selective Pt photodeposition

One factor to consider is that, with higher roughness, the contact area between the probe and the sample increases, and this may lead to higher measured currents. In order to account for this, platinum photodeposition on fully crystalline samples was carried out. Samples were placed in a conventional photoelectrochemical cell, fitted with a quartz window, and filled with Pt precursor/salt solution, with 20 % of methanol as a hole scavenger, and illuminated with simulated sunlight (AM1.5G) (no potential was applied). Deposition time and Pt salt concentration were adjusted to get the selective Pt coverage: by increasing one and/or the other, the whole sample was covered with Pt film (see *Figure 25*). Samples were imaged with AFM and it was observed that Pt photodeposition is selective, and tends to take place on the regions that have higher roughness, leaving smooth areas almost blank (*Figure 26*). Therefore, the roughness itself seems to be a main factor affecting the availability of charge carriers at the sample surface. Interestingly, the lower areas that exhibit low photocurrents were also covered with Pt nanoparticles. The Pt nanoparticles on the lower areas were smaller and packed more closely than the Pt nanoparticles on the high rough areas. The higher number and smaller size of deposited particles points to a higher number of nucleation sites.

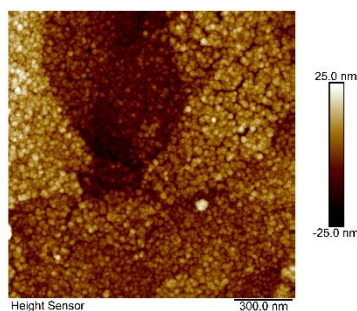


Figure 25. TiO₂ surface is fully covered with Pt film when increasing the deposition time from 2.5 minutes to 5 minutes. Methanol was used as a hole scavenger.

Literature discussion

Other research groups have demonstrated selective photodeposition of noble metal nanoparticles on anatase facets due to the different solvent adsorption, which alters the charge distribution between different facets [149], [150]. According to Chamtoury et al. [149] using methanol as a hole scavenger, methoxy groups will be adsorbed on the TiO₂ surface, causing the Fermi energy level of the low energy 101 facet to shift to lower energies compared with 001 facet. Electrons will move from higher to lower energy configurations, resulting in an excess of electrons on lower energy facets. A high number of electrons enables the reduction of more Pt salt, thereby producing a higher load of noble metal nanoparticles. On the contrary, when using ethylene glycol as a hole scavenger, hydroxy-ethanolate groups are adsorbed on the surface [150]. The change in energy levels of different facets is minimal and electron migration between the facets is suppressed [149]. This causes noble metal nanoparticles to deposit all over the sample surface. Another difference when compared with methanol as a hole scavenger is the size of nanoparticles. When using monoalcohol, already deposited metal particles act as electron traps and thereby hinder the deposition on other nanoparticles on neighboring positions, instead causing already existing particles to grow [149]. This is hindered by the presence of ethylene glycol, as it increases the deposition rate compared with monoalcohol. Increased rate leads to shorter electron lifetimes (which will be directly used for metal salt reduction) whereas in the presence of monoalcohol the electron lifetime is longer and electrons can be drawn to already deposited metal nanoparticles [150]. Another reason for smaller particle size and homogenous distribution is due to the hydroxy-ethanolate groups, which are strongly adsorbed all over the TiO₂ surface, thereby blocking

the active sites, which in turn suppresses the electron trapping by the deposited metal nanoparticles [150]. As ethylene glycol is a very efficient hole scavenger (it needs five holes to be oxidized, compared with methanol which needs three holes) the adsorbed species will be oxidized rather fast and the resulting radicals will reduce the metal salt all over the sample surface. Additionally, density of states (DOS) calculations have revealed an extra localized state within the bandgap of 001 facets resulting in slightly higher electron concentration, thereby increasing the reductive properties of 001 facets to some extent, compared with 101 facets that had higher reductive properties in the presence of monoalcohol [149], [150].

Experiments on photodeposition selectivity

We were able to reproduce this tuning of the Pt deposition selectivity on our samples, and the results can be seen on *Figure 26* (Pt photodeposition in the presence of methanol) and *Figure 27* (Pt photodeposition in the presence of ethylene glycol). Compared with methanol as a sacrificial agent, which caused Pt nanoparticles to deposit mostly on the high rough and low areas, leaving the smooth areas almost empty (see example marked with blue circle on *Figure 26a* and *b*), using ethylene glycol results in smaller nanoparticle size and a more homogenous distribution over the sample surface. It is also noticeable in *Figure 27* that the smooth grains (marked with a blue circle), which were empty when using methanol as a hole scavenger, are covered with Pt nanoparticles when using ethylene glycol as a hole scavenger. *Figure 27d* and *e* show adhesion channel data, to help distinguish surface roughness from the Pt nanoparticles. The marked grain is smooth in areas, where no Pt nanoparticles have yet deposited.

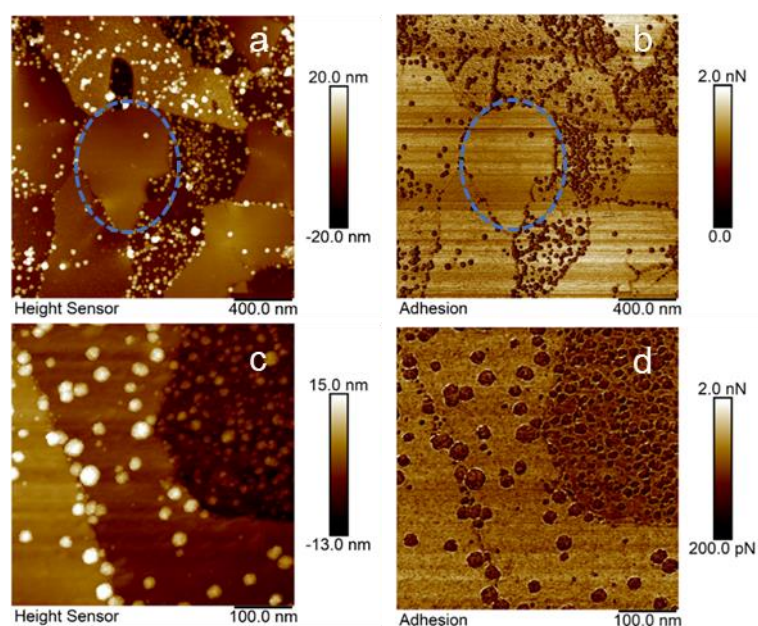


Figure 26. Pt photodeposition using methanol as a hole scavenger. **Left:** topography, **right:** additional channel (adhesion) that helps to better identify Pt nanoparticles from the TiO₂. Bottom images are captured using a smaller scan size. One example of the smooth area is marked with a blue circle.

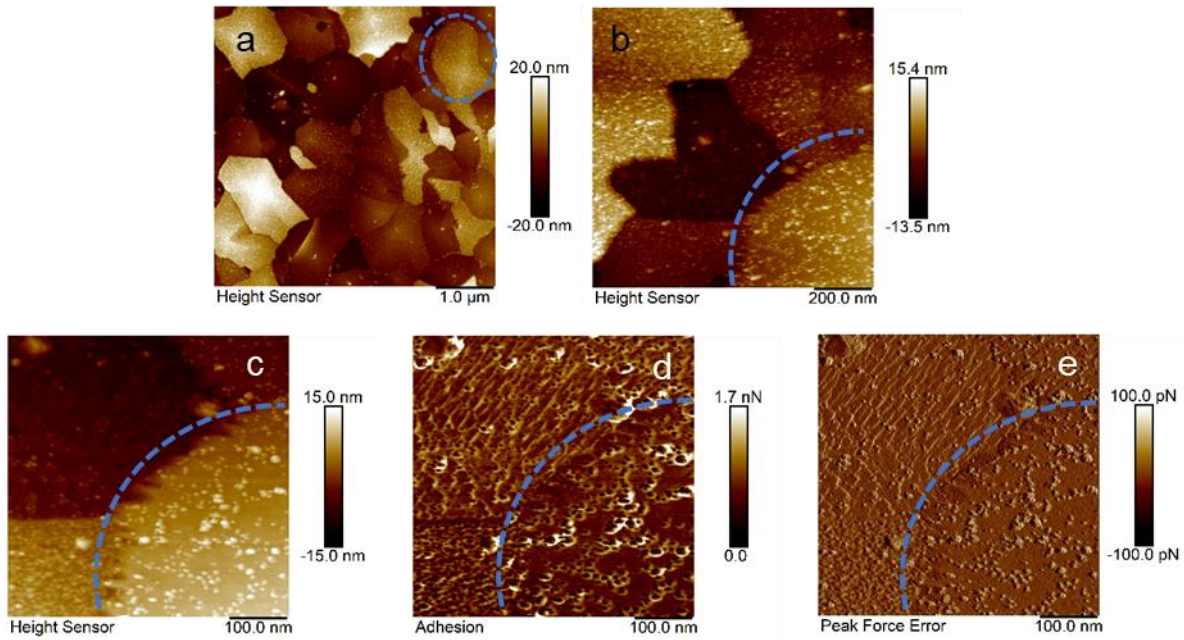


Figure 27. Pt photodeposition using ethyleneglycol as a hole scavenger. Images a, b, and c are topography images with different scan sizes. Images d and e are additional channels (adhesion, peak force error) for image c, showing the smooth surface of the marked grain (where no Pt has deposited yet), compared to the intrinsic roughness of the neighboring grains.

4.1.4 Identification of different grain types

We can distinguish different surface morphologies according to roughness, height and size. In this work, four main morphologically different grains types were identified which are marked with different colors in *Figure 28a*.

1. High rough grains, marked with blue color.
2. Middle smooth grains, marked with red color.
3. Middle rough grains, marked with green color.
4. Low grains, marked with yellow color.

The average height, area and roughness were calculated for each of the four grain types from the data presented on the *Figure 28a*. For high rough grains, the average of three grains marked with blue color was used (the blue grain on the left border on the *Figure 28a* was excluded as it does not fit completely within the image). For middle smooth grains, the average of the three red areas was used. For middle rough grains the average of the four green areas, and for low grains the average of the four yellow areas was used for comparison. The software packages Fiji (ImageJ), Gwyddion and Bruker Nanoscope were used respectively for estimation of average areas, heights, and roughness values. For the height comparison between the four grain types, all data values were shifted so that the minimum values were assigned 0 height, in order to avoid negative height values. The results are presented in *Table 5*. The high rough grains have the largest average area and highest roughness, and are the tallest among the four different types. Middle smooth grains have the second largest average area and height, but as mentioned have low roughness. Middle rough grains have a height close to middle smooth grain type, but are smaller in area. Low grains have the smallest average area, roughness and height among the four distinct grain types. *Figure 28b* is an additional channel (peak force error) that helps to reveal fine structural details and can give an initial comparison of the grain types with different roughness.

Table 5. Characteristics of four distinguishable grain types with different surface morphology.

	Height (nm)	Area (μm^2)	Roughness (Rq) (nm)
High rough	21.8	1.5	1.3
Middle smooth	16.9	0.8	0.5
Middle rough	13.6	0.5	0.8
Low	6.6	0.3	0.3

Literature discussion

For the activity of the 001 facet, contradicting results are reported in the literature. A large number of studies have shown higher activity of the 001 facet compared with the 101 facet, and attributed it mainly to the higher surface energy and dissociative water adsorption of the former [82], [151], [152]. Other studies have demonstrated that the higher activity is instead governed by the existence of F⁻ ions in the structure, which are difficult to remove from 001 without surface reconstruction [153]–[156]. The F⁻ ions are part of the capping agent used to stabilize high energy facets during the anatase particle growth process. Post treatments like annealing or NaOH washing are used to remove the F⁻ ions [153]. This leads to surface relaxation and reconstruction to lower the surface energy, changing the surface properties by creating vacancies. The presence of the F⁻ ions leads to higher photocatalytic activity of 001 surface due to the surface electronic alteration [153] and/or due to higher oxygen adsorption as a result of the presence of HF [155]. Surface relaxation after F⁻ removal indicates that the pure 001 facet is unstable and undergoes (1x4) surface reconstruction in order to lower the surface energy which also reduces the reactivity of the 001 facet [154], [156]–[160].

Grain identification

Based on the photocurrent and photodeposition tests with two different hole scavengers, a preliminary assignment between the different grain type surfaces and anatase facets can be done. Low photoactivity and a high number of photodeposited Pt particles on lowest grains indicate that these expose the low surface energy facets 101, marked with yellow color.

Since as discussed, according to the literature photodeposition is not preferred on 001 facets when using methanol as a hole scavenger, but 001 facets become the preferential surface for deposition when using ethylene glycol as a hole scavenger, and based on our results, we assign the smooth grain surfaces to 001 facets, marked with red color.

Furthermore, in this work, no capping agents were used during the film growth process and therefore the active, high surface energy facet 001 can only exist in (1x4) surface construction, low surface energy and low activity form. This would explain the low photocurrent on these areas that, based on the photodeposition results, can be assigned to the 001 anatase surface.

Hence the high rough grains which are the most photoactive (marked with blue color) can be expected to expose high energy facets 110 or 111. Since the synthesis of anatase single crystals with high surface energy facets (110 and/or 111) is very challenging, little information is available on the photodeposition on these facets, and a more specific assignment by this method is not possible.

The middle rough grains (marked with green color) could then be assigned to facets with surface energy in between the 101 and 110/111, namely 100 or 010. Nevertheless, while the presence of 101 and 001 facets is certain since they are the most energetically favored surfaces of anatase, the presence of higher energy facets 100/010 and 110, 111 is questionable and needs further

complementary studies, for example by transmission electron microscopy (TEM) and electron backscatter diffraction (EBSD).

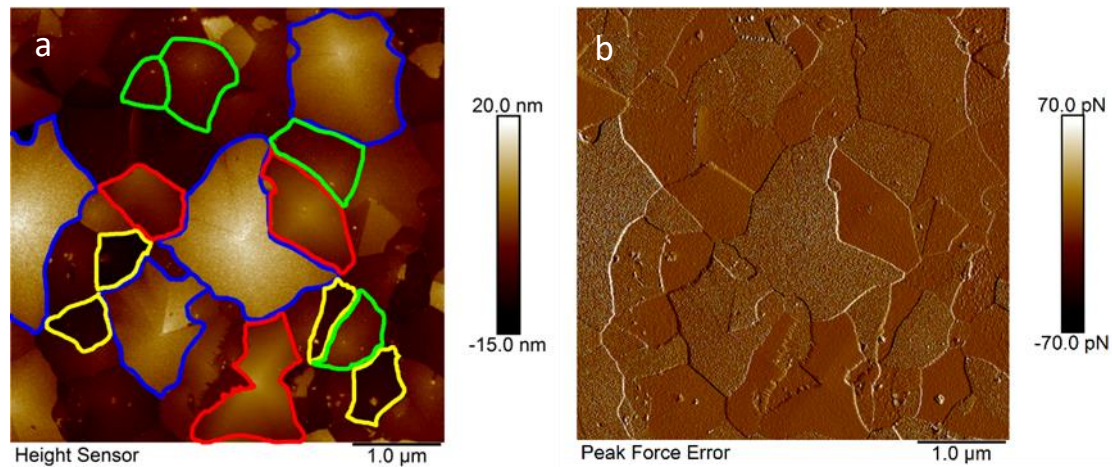


Figure 28. Different grains marked with individual colors (a) and an additional channel (peak force error) that helps to reveal fine structural details (b).

4.1.5 Crystal growth direction

Electron backscatter diffraction (EBSD) was conducted on the fully crystalline 100 nm thin film TiO_2 sample to determine the growth direction of the individual grains. Although EBSD analysis gives the orientation of the grains looking from certain reference points, and not the exposed facets on the surface, it allows to identify whether certain grain types (discussed in the previous section) have a preferred crystallographic direction. An orientation map is presented with an Inverse Pole Figure (IPF) color key, indicating the crystallographic poles aligned with a specified sample direction. AFM topography and corresponding IPF-Z (orientation map, taking the axis normal to the sample (Z) as the viewing direction) images are presented on *Figure 29*. The IPF-Z map shows no predominant color which means there is no preferential orientation of the grains in general on these samples. It should be noted that on the *Figure 29* only a small area of the IPF-Z maps is presented; a larger SEM scan and corresponding IPF-Z maps can be found in the Appendix (*Figure A. 2*). Allowing 10° of misorientation we can distinguish several directions: the highest number of grains have a [101] crystallographic direction, followed by [100] and [120] (see *Figure A. 3*). For grains showing a pyramidal shape crystalline growth, with the initial anatase seed on the top, there is a variation in the growth direction within the single grains. On the IPF-Z and AFM data taken on the same region, it can be seen that the high rough grains have a dominant direction of [110] and [120]. Middle smooth grains have a dominant direction towards [100], and low areas towards the [001] and [101] directions. The summary is presented on the *Table 6*. This confirms the above assumptions in paragraph 4.1.1 that the specific grain types have the similar crystalline direction. Nevertheless, the middle rough areas seem to have different orientations and not one or two preferred.

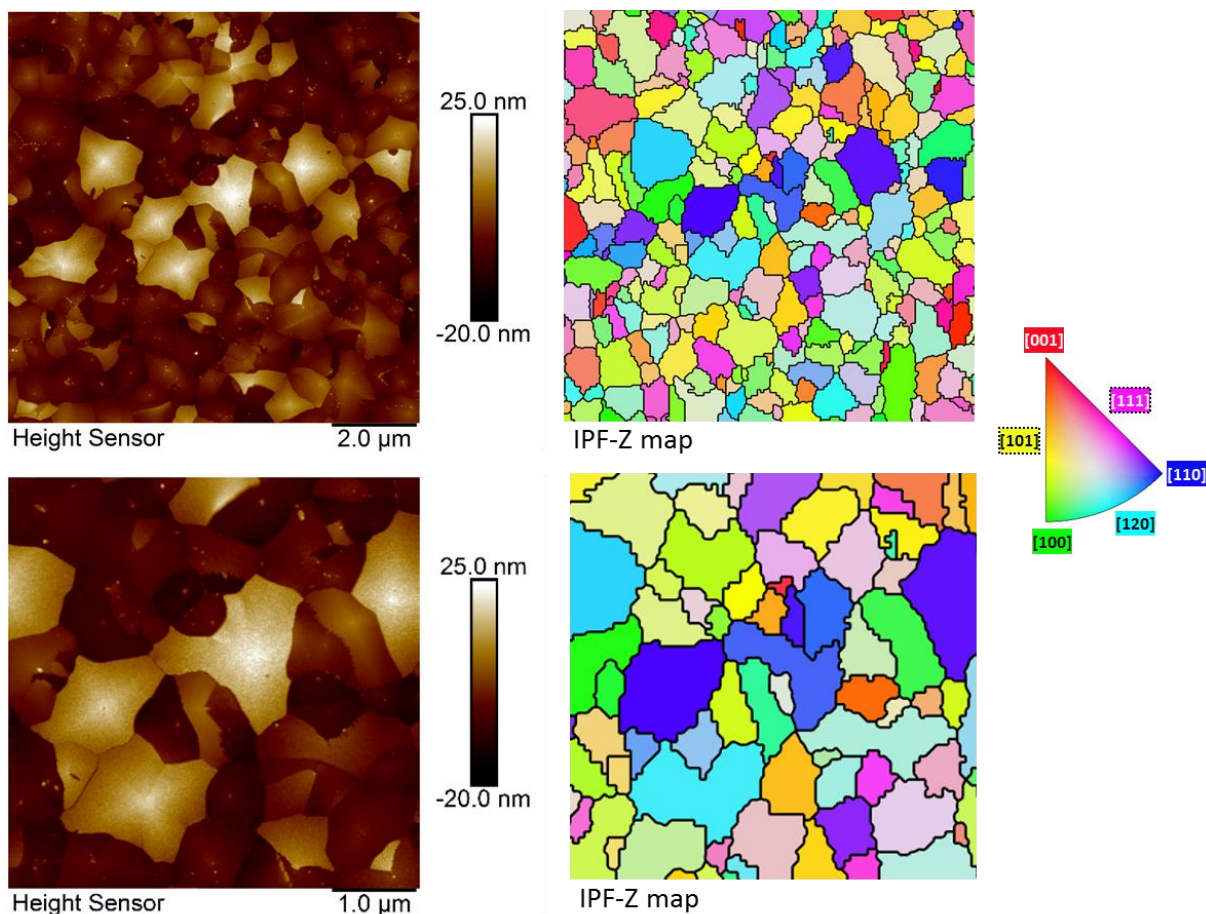


Figure 29. AFM topography and corresponding EBSD IPF-Z map with 10 x 10 μm and 5 x 5 μm scan sizes. Later is the higher resolution of the 10 x 10 μm images. IPF-Z color key is presented on the bottom.

Table 6. Grains identified with high resolution topography measurements and correlated with anatase facets based on photodeposition and photocurrent results and with the help of literature. These were further correlated with underlying crystalline orientation with the help of EBSD characterization.

	Facet based on photocurrent	Facet based on photodeposition	EBSD direction
High rough	110,111	-	110–120
Middle smooth	-	001	110
Middle rough	100/010	-	-
Low	101	101	101

In conclusion, we have shown that local variations in photoactivity observed on the surface of these ALD deposited TiO_2 samples are mostly governed by the difference in crystallographic structure. We can identify four main grain types according to morphology, selective photodeposition and photoactivity. From EBSD measurements on a fully crystalline TiO_2 thin film we can assign three of the four grain types to particular orientations. Correlative studies with AFM and EBSD, on the same region of interest of the sample surface confirmed the assumption that the identical grain types have a similar crystallographic orientation. Further analysis is needed in order to identify the exact nature of the exposed facets.

4.2 Surface voltage mapping

In this chapter the surface voltage on mixed amorphous/crystalline phase TiO_2 samples is studied by measuring contact potential difference (CPD) in dark and under illumination conditions. From the difference between the CPD in dark and under illumination, the ΔCPD (surface photovoltage, SPV) was obtained for both crystalline and amorphous phases with high lateral resolution. The evolution of CPD was studied against time, evidencing the charging and discharging of trap states. We furthermore investigate the origins of a size discrepancy of the studied film features, observed when comparing topography and potential maps.

The influence of illumination on the surface potential was studied on 50 and 75 nm thin film TiO_2 samples. As shown on *Figure 30*, upon illumination the surface potential shifts to negative values, which is clearly noticeable on the crystalline areas. The surface potential of the amorphous fractions changes as well, also shifting towards negative values. The band gap for 50 and 75 nm samples was calculated measuring the SPV signal at various photon energies and was 3.40 and 3.37 eV respectively [142]. For fully amorphous TiO_2 films prepared in similar conditions as these 50 and 75 nm samples (but at lower reaction temperature), the optical bandgap was found to be 3.30 – 3.45 eV [161]. Since the 365 nm wavelength corresponds to a photon energy of 3.40 eV, we expect that the change in surface potential on the amorphous component of these samples to be primarily due to light adsorption in amorphous TiO_2 . As a result of the lift height used during the potential measurement, the crystalline areas on the 50 nm sample appear larger on the potential map compared to the height sensor map (this will be discussed in more detail in the next section). On the 75 nm sample, the photovoltage map evidences amorphous regions that are otherwise not easily identifiable on the topography map.

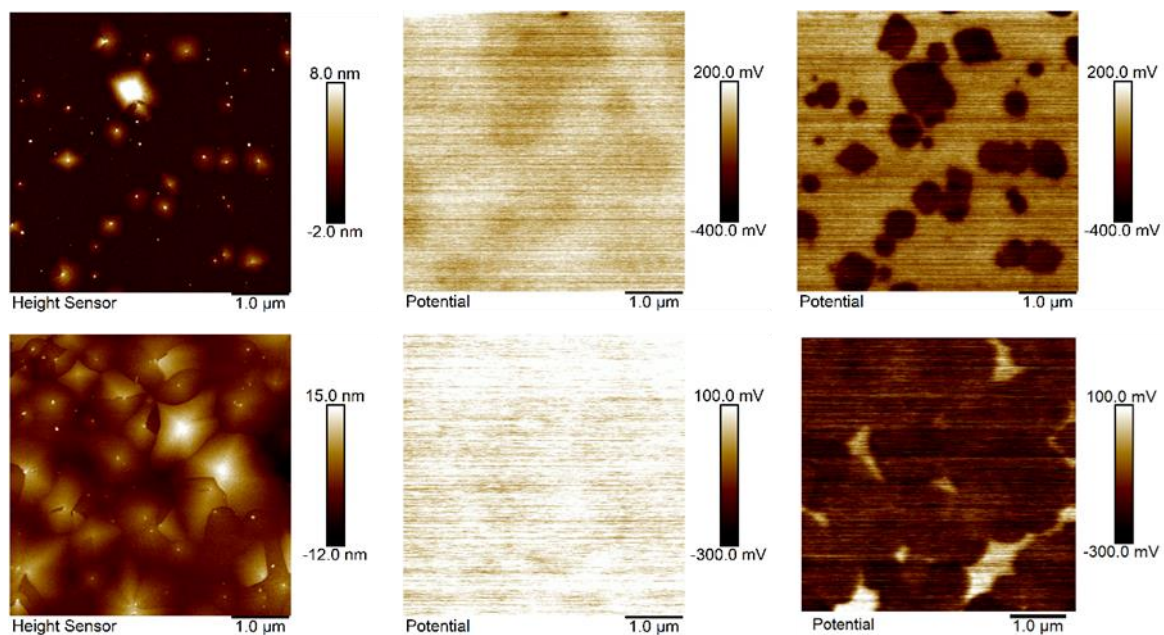


Figure 30. Topography and KPFM maps in dark and under illumination. The **top row** corresponds to the 50 nm sample and the **bottom row** to the 75 nm sample. Topography (on the left) and corresponding surface voltage maps in dark (in the middle) and under illumination (on the right).

Data histograms for the potential channel were fitted to the Gaussian distribution function in order to obtain in each case the peak value, which corresponds to the average contact potential difference (CPD) between the sample and the probe. For images in dark conditions, one peak for the whole sample can be seen, whereas under the illumination two peaks are clearly resolved. These two peaks correspond to CPD distribution of two different phases. The higher peak corresponds to the major

component phase, e.g. amorphous phase on the 50 nm sample, and the lower peak to the minor component phase. For both samples the average CPD value in dark conditions is similar, being 96 for the 50 nm sample and 92 mV for the 75 nm sample. Under illumination a peak corresponding to the crystalline phase on the 50 nm sample is observed at -236 mV, and a peak for the amorphous phase at -24 m mV. On the 75 nm sample, crystalline and amorphous phases have a peak values of -173 mV and -68 mV accordingly.

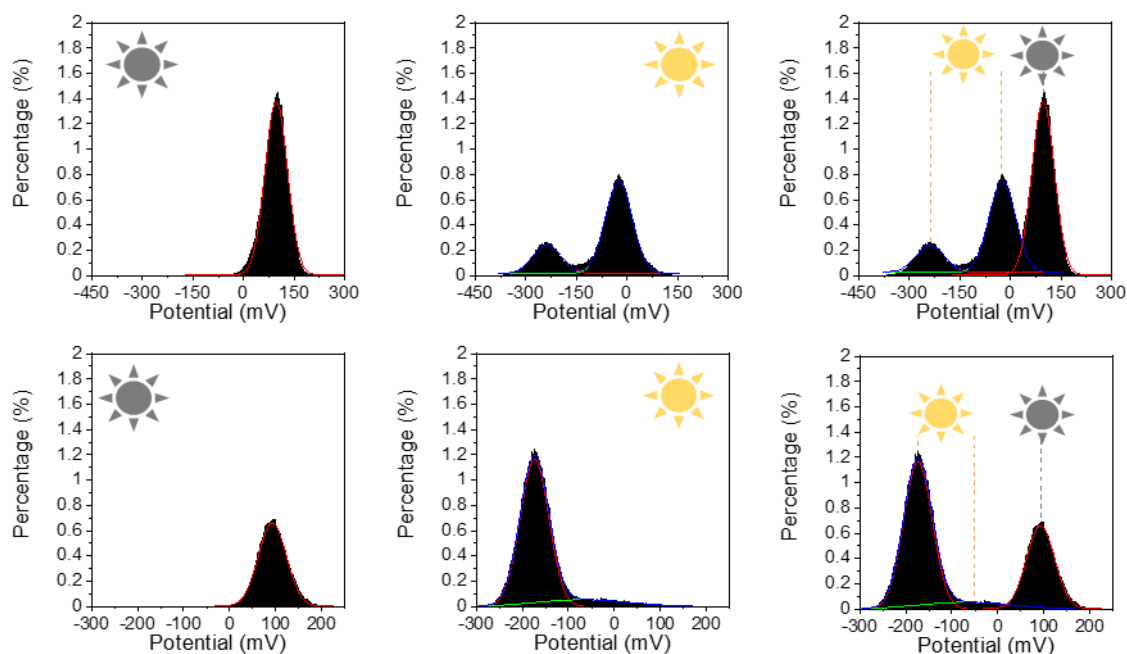


Figure 31. KPFM data histograms. **Top row** corresponds to the 50 nm sample and **bottom row** to the 75 nm sample. **Left:** CPD distribution in dark conditions; **middle:** CPD distribution under illumination and on **right:** CPD histograms in dark and under illumination are both presented for better comparison.

By subtracting CPD in dark from CPD under illumination, we can calculate the change in CPD (Δ CPD). The upward band bending of the n-type semiconductor is due to accumulation of negative charges on the surface resulting in the formation of a positively charged space-charge region. Under illumination, holes move towards the surface and neutralize the negative surface charge to some extent, while the photogenerated electrons generate an electric field that opposes the space charge field, thereby reducing the band bending. This leads to a more negative CPD. *Table 7* lists Δ CPD for amorphous and crystalline phase for both samples. Upon turning on the LED, the Δ CPD for the crystalline fraction on the 50 nm sample is -332 mV, while for the 75 nm sample reaches -265 mV. For the amorphous domain the Δ CPD on the 50 nm sample is -120 mV and on the 75 nm sample -160 mV. The distribution of Δ CPD on 50 and 75 nm samples is illustrated on *Figure 32* where the green areas correspond to higher CPD change. The Δ CPD for crystalline and amorphous phase is higher on the sample where the particular phase is the minor component. The reason for this phenomena is not yet clear and is currently under further studies.

Table 7. Change in CPD on 50 and 75 nm samples.

Sample	Crystalline phase Δ CPD (mV)	Amorphous phase Δ CPD (mV)
50 nm TiO ₂	-332	-120
75 nm TiO ₂	-265	-160

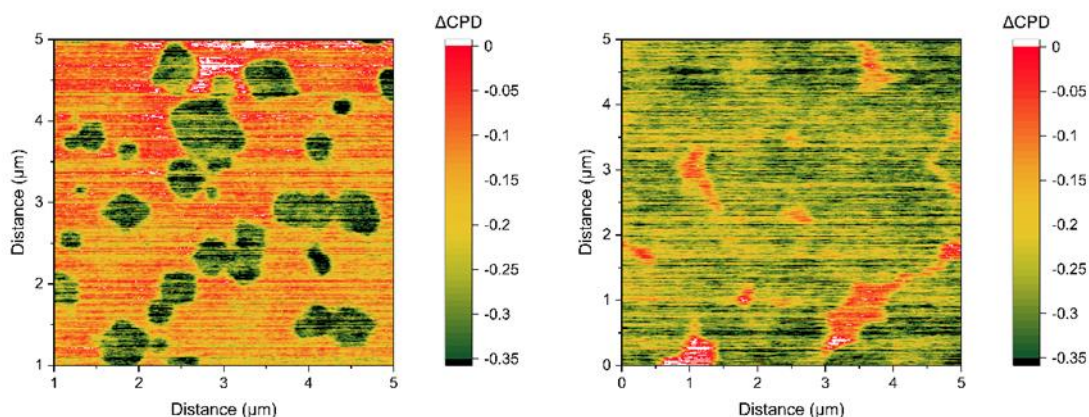


Figure 32. Change in CPD on **a)** 50 nm sample and **b)** 75 nm sample.

The scans discussed above were acquired just after switching the illumination on, starting at the top and moving downwards on 50 nm sample and starting at the bottom, and moving upwards on 75 nm sample. Thus, the ends of these scans were acquired closer to the respective equilibration potentials than the beginning.

Figure 33 shows two scans under illumination for the 75 nm sample. The scan in Figure 33b was obtained just after switching the LED on. The amorphous regions in the beginning (bottom) of the scan have similar values as the image mean in the dark (Figure 33a). On the second image under illumination (Figure 33c), the charge-carriers have reached the steady-state condition all over the CPD image.

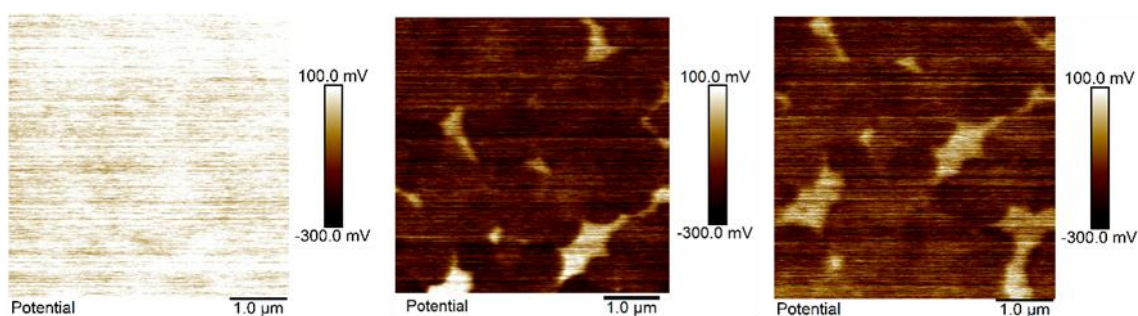


Figure 33. Potential maps on the 75 nm sample. **Left:** surface voltage in dark; **middle:** surface potential directly after turning on the LED (scan direction from bottom to top); **right:** surface potential under the illumination after the stabilization of the surface potential.

4.2.1 CPD vs time

Time-dependent CPD measurements can give insight into charge-carrier dynamic processes, such as trapping and detrapping, spatial redistribution, recombination, accumulation, etc. The evolution of the CPD after illumination was studied on the mostly amorphous 50 nm sample. Two initial KPFM images were obtained in dark conditions, followed by two images under illumination. Subsequently the LED was turned off, and the evolution of the CPD in dark conditions was observed for 3.5 hours, during which 17 KPFM images were captured. The mean value of the CPD was taken from each KPFM image and plotted against time. Three different CPD values were extracted from each image: for the crystalline phase (Figure 34a), for the amorphous phase (Figure 34b) and for the whole image, which is a mixture of both phases (Figure 34c). The topography of the area where the measurements were carried out can be seen on Figure 34e, and examples of the regions where the crystalline, amorphous and mean potential values were measured are shown on Figure 34f (CPD map in dark) and on Figure

34g (CPD map under illumination). For reference, the values obtained from Figures f and g are marked with gray circles on the curves in Figure 34a-c. A green box (5 x 1 μm) shows the area from which the image mean potential value was extracted. A blue box (250 x 300 nm) and a red box (1 x 1 μm) mark the areas where the crystalline and amorphous phase potentials were respectively measured. For each data point on the curves a to c on Figure 34, there is a corresponding potential map similar to Figure 34f and g. It can be seen that the crystalline phase almost reaches its original equilibrium value in the dark, but the initial value for the amorphous phase is not reached even after 200 minutes of measuring in the dark. Not only does it take more time for amorphous phase, compared to crystalline phase, to reach the initial equilibrium value after the illumination, but it also takes charge carriers in the amorphous phase more time to reach the steady-state condition upon illumination. It should be noted that from our previous studies on the same sample, where additional measurements under the illumination were performed before switching the light off, as similar effect was also observed upon switching the light on, that is, the crystalline phase reaches the equilibrium faster and remains stable upon illumination, whereas the amorphous phase takes more time to reach the steady-state condition.

After photoelectric charge injection the slow diffusion and redistribution of charge carriers in nanocrystalline TiO_2 can be attributed to trapping and detrapping in surface and bulk states as well as in defect states at the amorphous/crystalline interface [118], [162], [163]. The amorphous phase contains, due to its disordered structure, a larger density of deep defect sites compared with the crystalline phase [142]. Charging and discharging these deep defect states upon illumination is a slow process and can be even non-reversible [164]–[167]. Therefore, it takes more time for amorphous phase to reach its initial CPD after illumination compared with the crystalline phase.

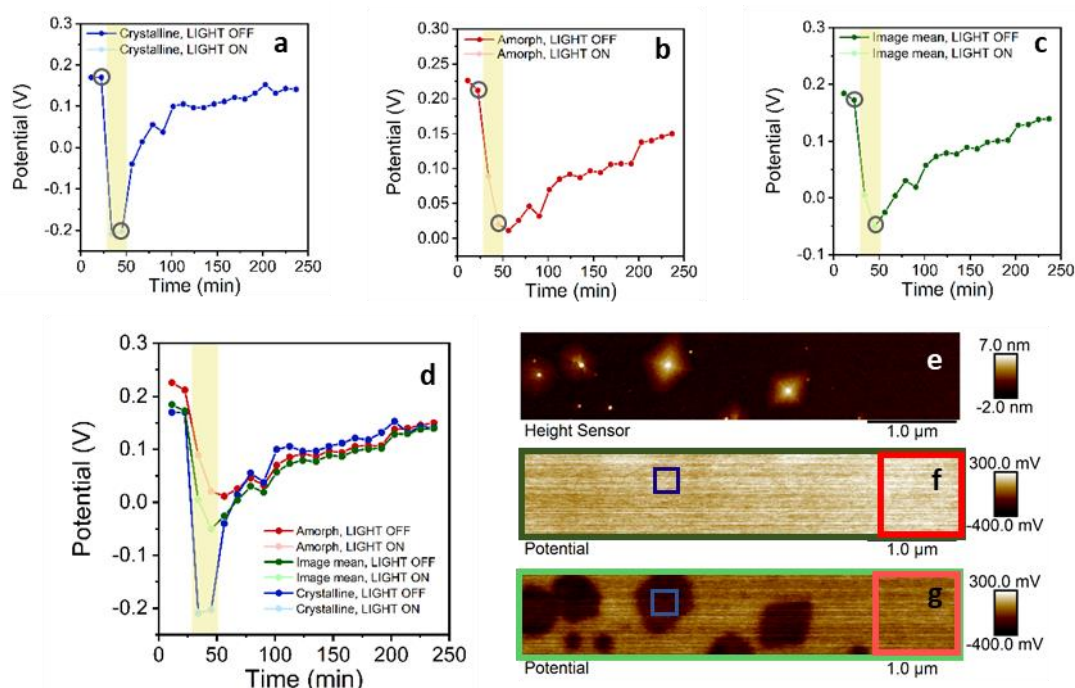


Figure 34. Evolution of the measured CPD on 50 nm sample, **a)** on crystalline regions, **b)** on amorphous regions, **c)** on the mixture of both phases (image mean). For an easier comparison, the graphs a to c are plotted together in **d)**. Yellow shaded area marks the potential values measured under illumination. The topography of the sample where the measurements were extracted is shown in **e)**, and two examples of CPD maps are shown in **f)** (in dark) and **g)** (under illumination).

Another possible consideration is the change in wetting properties of the TiO₂ surface upon UV irradiation. It has been shown that rutile and amorphous TiO₂ change from hydrophobic to superhydrophilic, and that anatase changes from hydrophilic to superhydrophilic, when illuminated with UV light [168]–[170]. The UV induced superhydrophilicity occurs within minutes, but after illumination the recovery in dark takes several days until the initial surface wetting properties are reached [168], [171]. Further studies are required to determine whether this phenomenon contributes to the behavior observed in *Figure 34*.

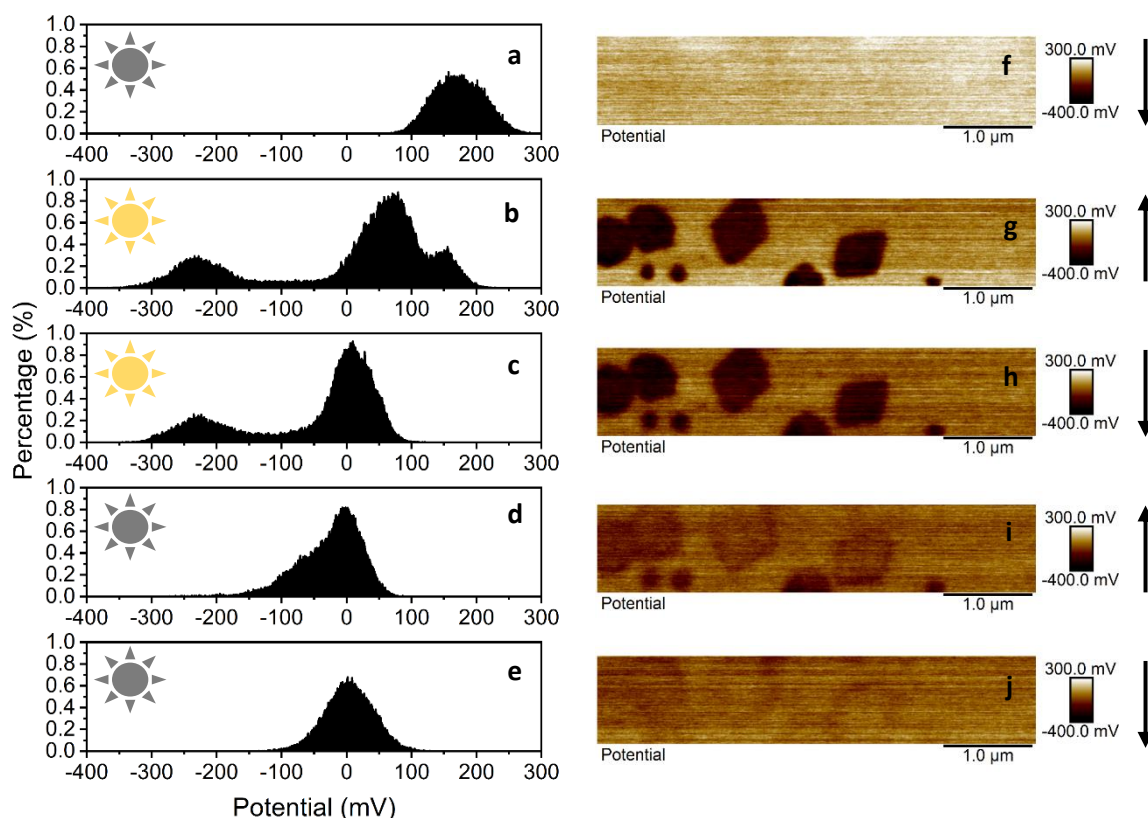


Figure 35. Evolution of the CPD in time. Data histograms in dark and under illumination (a-e) and corresponding CPD maps (f-j). Arrows on the right show the KPFM scan direction.

The evolution of the surface photovoltage with time was analyzed using the potential map data histograms. The initial data histograms in dark conditions consist of one peak (*Figure 35a*). Upon turning on the LED, three peaks can be distinguished (*Figure 35b*). The peak at more positive potential corresponds to the fraction of amorphous phase that still has a potential value similar to the initial value in the dark. The peak in the middle corresponds to the fraction of amorphous phase for which the potential has already shifted towards more negative CPD. The peak on the left represents the crystalline phase. On the second data histogram under illumination (*Figure 35c*) two peaks are recognized, higher peaks for the amorphous phase and lower for the crystalline phase. The peak corresponding to the crystalline phase is on the same position as on the previous graph (*Figure 35b*) showing that on the first CPD image under illumination, the crystalline phase has already reached the steady state condition. This is a clear demonstration of how, for the amorphous phase, the equilibrium state under illumination takes more time to reach compared with the crystalline phase. By masking different potential ranges on this map (see *Figure A. 5*), three significant sample fractions can be

identified: amorphous phase (peak at more positive CPD), crystalline inclusions (peak at more negative CPD), and the crystalline/amorphous interface (shoulder at intermediate CPD values). After turning off the LED the peak for the crystalline phase starts to disappear and forms a shoulder next to the amorphous peak (*Figure 35d*). On the second image in the dark (*Figure 35e*) only one peak is observed, as on the initial data histogram in dark. However, the initial potential value has not yet been recovered, as the peak value is 175 mV less positive than the initial peak position in the dark. *Figure 35f-j* illustrate the CPD map for each data histogram, and the arrows on right show the KPFM scan direction. As evidenced on *Figure 35j*, the CPD at crystalline/amorphous interface is the slowest to return towards the dark value after switching off the light, confirming the enhanced trapping of photogenerated carriers at this interface.

4.2.2 Instrumentation effects

As mentioned above, areas on the potential map that correspond to the crystalline phase appear larger than the crystalline areas on the height sensor map. This can also be seen on *Figure 36c-e* where the cross-sections of the height and respective cross-sections of the potential is plotted with each other. Gray dotted lines mark the beginning and the end of the potential corresponding to the protruding crystalline feature. The difference between the two maps is due to the lift height during the potential measurement, which was held 50 nm. As a result, the features on the CPD map appear at least 100 nm larger in diameter than on the height sensor map.

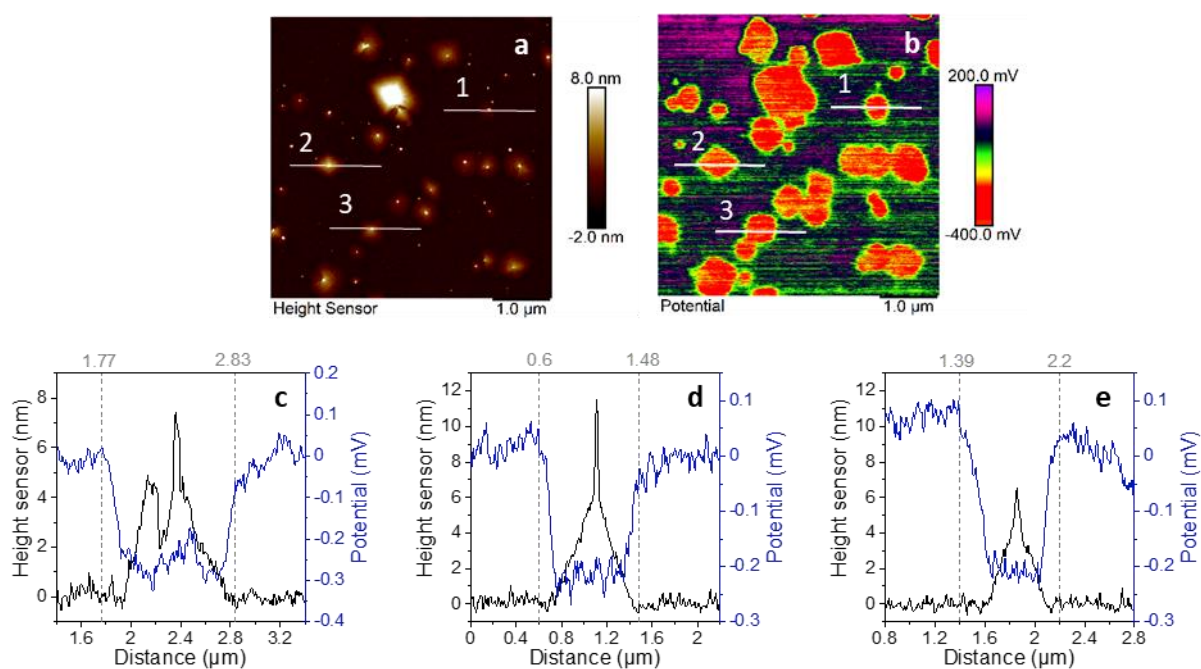


Figure 36. Topography (a) and respective potential map (b) under illumination. Cross-sections of the height and respective potential (c-d).

In addition to lift height, tip convolution effects can be seen on *Figure 36c-e*. The left side of the potential cross section is further away from the corresponding crystalline feature compared with the right side. This is due to the fact that the front angle of the probe is smaller than the back angle: 15° and 25° respectively. As the raster scan was performed using a 0° scan angle, the back side on the probe always touches the left side of the features and the front side, the right side of the features. As a result, the features on the CPD map appear larger on the left side. This artefact is seen more easily on the taller protruding objects (*Figure 37*). The sample on *Figure 37* is a 40 nm ALD TiO_2 thin film with

degraded amorphous phase and therefore more exposed crystalline phase. On the cross-sections on *Figure 37c-d*, the left side of the crystalline phase, which is detected with the back side of the probe, is larger than the right side, which is detected with the front side of the probe.

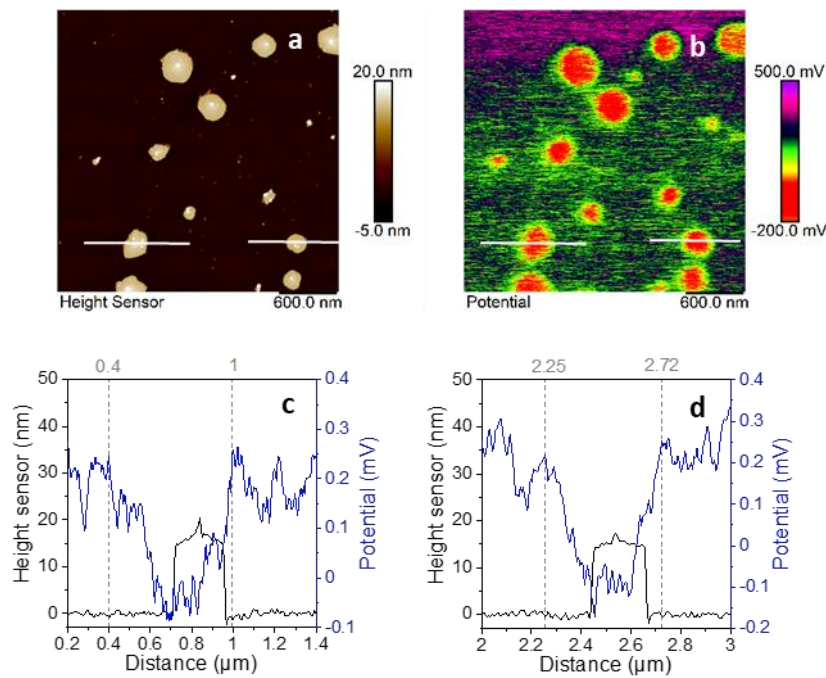


Figure 37. Topography (a) and respective potential map (b) under illumination on the degraded 40 nm thin film TiO_2 sample. Cross-sections of the height and respective potential (c-d).

In conclusion, surface voltage and photovoltage was measured for both crystalline and amorphous phase TiO_2 . We observed that, upon illumination, the amorphous phase requires more time to reach the steady-state condition compared with the crystalline phase. When turning off the light, after several hours, the amorphous phase has still not reached the initial CPD value in dark conditions. These investigations confirmed the existence of higher amount of defect states in the amorphous phase compared with the crystalline fraction. Further analysis also revealed significant trapping of charge carriers at the interface between the two phases. Additionally, by comparing CPD maps with topography images, we observed that the larger magnitude of features on the potential map is not only due to the lift height, but also because of the tip convolution effect.

4.3 Charge carrier transport mechanisms at tip-semiconductor nanojunction

In this chapter the majority charge carrier transport mechanism was studied at the metal tip and TiO₂ sample nanojunction. Current voltage curves were obtained at each pixel of the AFM scan (a total of 32768 I-V curves) on a fully crystalline TiO₂ sample. For each pixel, the segment of the I-V curve with the highest slope was fitted with the linear relationships corresponding to the various transport mechanisms that occur at the metal-semiconductor contact. Measurements were conducted with Au and Pt coated CAFM probes.

Although current maps in dark and under illumination conditions can reveal heterogeneities in photoactivity and its correlation with morphology, they do not provide information about conduction mechanisms at the tip/sample nanocontact. In order to investigate this, spectroscopy mode CAFM was used to capture full I-V curves at the tip/sample interface for each pixel on a topography scan of the surface of the sample. An array of 128 x 256 I-V curves was collected with metal coated AFM probes resulting in a total of 32768 curves per image. The scan size was 5 x 10 μm, resulting in an I-V curve being captured at about every 40 nm, which is enough for probes with end radius of 25-35 nm to avoid duplicated data points. A positive bias was applied to the Si/TiO₂ sample, as this corresponds to the operating condition for photoanodes. From the captured I-V curves it is possible to construct a current map at any voltage ("hold segment slice"). On *Figure 38* topography and current image recorded at 8.0 V in the dark can be seen. Similar to current maps measured with TUNA mode, heterogeneities in sample electronic properties are revealed. In a first approximation, regions with three different current magnitudes can be recognized: areas with high current (up to 5.5 nA), areas which exhibit no current, and regions that are in between 0 and 5.5 nA.

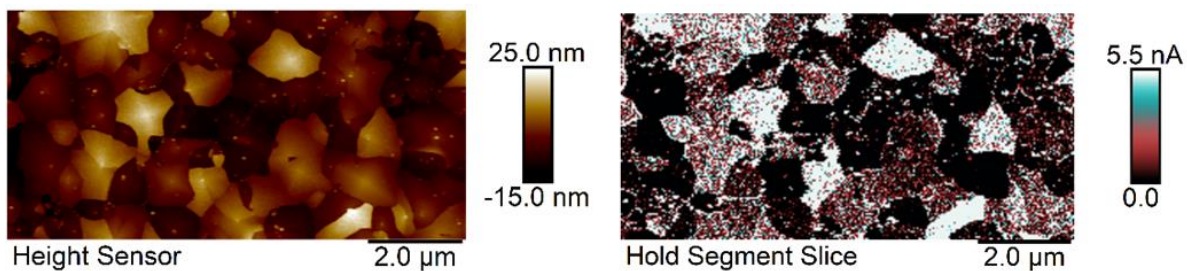


Figure 38. On the left topography and on the right current map (hold segment slice) at 8.0 V.

At higher voltages (4.0 – 8.0 V) electron injection is mostly driven by the applied bias and therefore no significant difference on current maps between dark and light can be seen. The difference is recognizable at lower voltages as shown in *Figure 39*: images were captured at 2.0, 2.5 and 3.0 V, both in the dark (top row) and under illumination (bottom row).

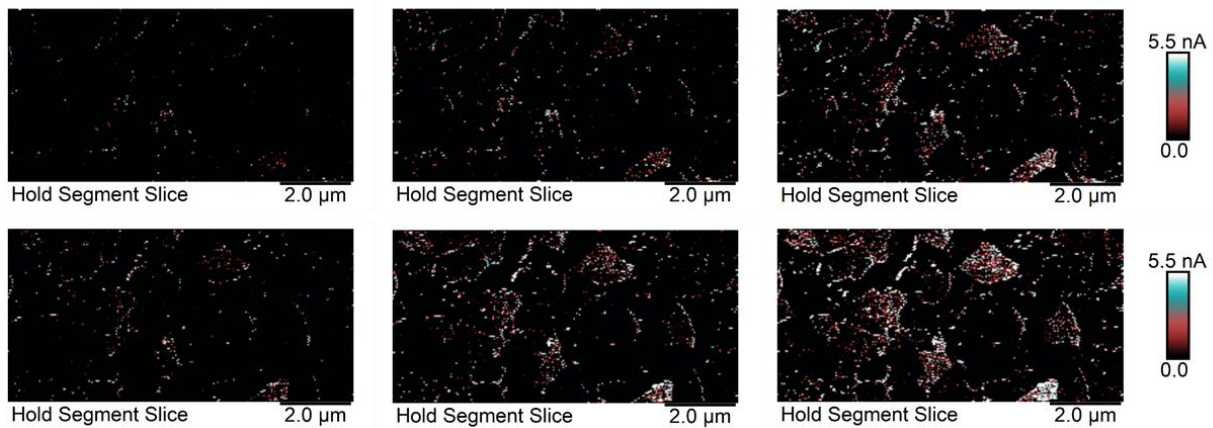


Figure 39. Current maps (hold segment slices) at (from left to right) 2.0, 2.5 and 3.0 V. Top: LED OFF and bottom: LED ON.

For our investigations, performed in the reverse bias regime, semiconductor and tip are connected respectively to the positive and to the negative terminals [172]. Electrons are injected from the AFM probe into TiO_2 thin film and collected by the back contact. Under illumination additional charge carriers are created, leading to an enhanced current (*Figure 39*) [19]. Furthermore, at high enough reverse bias voltage, a rapid current increase is observed in the reverse bias regime (*Figure 40*). This behavior has been previously observed for nanoscale Schottky junctions, and was attributed by Rezeq et al. [16],[18] to the enhanced charge density for nanosized contacts where the metal (tip) radius is much smaller than the width of the conventional depletion width at the metal/semiconductor interface.

The highest slope region of the I-V curves was fitted with different conduction mechanisms that can take place at metal-semiconductor nanojunction [34], [36]. An example I-V curve is illustrated on *Figure 40*. At a certain voltage, current increases exponentially and reaches the saturation current (5.2 nA) which is given by the current limit set in the instrument during the measurement configuration.

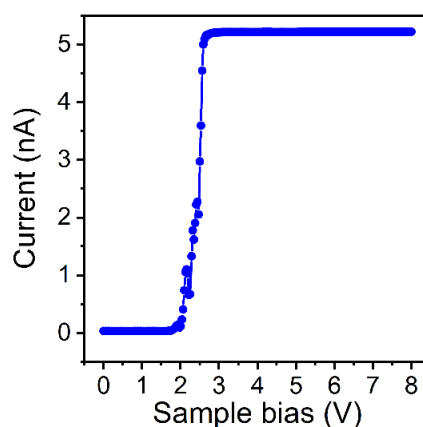


Figure 40. Example I-V curve measured on fully crystalline TiO_2 with Au coated probe. Inset graph shows the curve with current limit plateau.

Figure 41 shows curve fitting, with different conduction models, of the highest slope region of the I-V data shown on *Figure 40*. Direct tunneling/field emission is discarded since it occurs when there is a thin (up to ~ 3.5 nm) insulating layer on top of the semiconductor [34]. By applying a reverse bias up

to 8 V, the depletion layer is much larger than 3.5 nm and therefore direct tunneling through the barrier can be excluded. Schottky emission and hopping conduction have the highest R^2 values and are considered as possible transport mechanisms at this particular metal-semiconductor nanojunction. Fitting with six different conduction models was repeated for all the measured I-V curves, and a map was constructed with transport mechanisms which had the highest R^2 value at each pixel. For example, the data on *Figure 40* corresponds to pixel No. 17742: for this pixel, Schottky emission was presented on the transport mechanisms map (*Figure 42*). Each transport mechanism is presented with individual color and number.

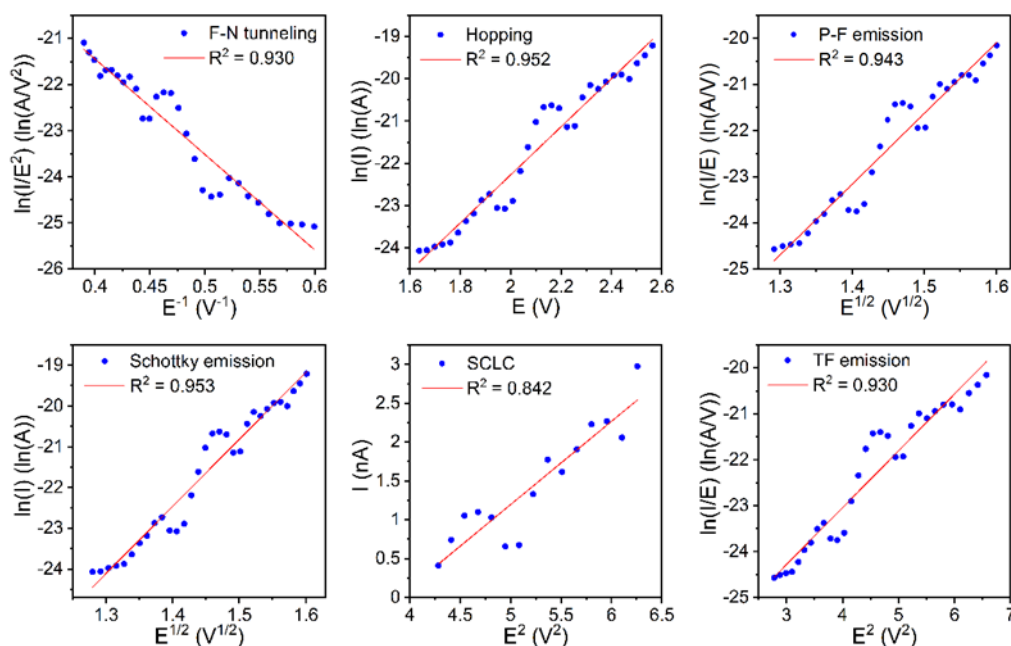


Figure 41. Fitting of the high slope region of the I-V curve to a various conduction modes.

Figure 42a (dark) and *Figure 42b* (under illumination) show, for each pixel, the transport mechanism that could be fitted with the highest R^2 value. The gray areas *Figure 42a-b* correspond to regions where no current was measured, and therefore no fitting could be done. *Figure 42c* (dark) and *Figure 42d* (under illumination) show only the pixels with best-fitting conduction mechanisms that could be fitted with R^2 higher than 0.9, all other pixels are shown in gray color. This R^2 threshold was chosen because pixels with R^2 smaller than 0.9 for the best fitting mechanism show I-V curves with significant noise and current instabilities, which can lead to misinterpretation of the data. Some minor current fluctuations can also be observed for curves with $R^2 > 0.9$ (see *Figure 40*), but these are rather small compared those for curves that have $R^2 < 0.9$. Examples of the I-V curves with conduction fluctuations are presented on *Figure 43*. Current instabilities at the tip and sample nanocontact are a well-known problem discussed in numerous research papers and will be briefly covered below [173]–[177]. On *Figure 42* it can be seen that the most of the majority charge carrier transport occurs through Schottky emission (green color). This is observed for the measurements obtained in dark and under illumination as well as when analyzing only I-V curves with lower noise ($R^2 > 0.9$). The summary of *Figure 42c* and *d* is presented on the *Table 8*. The total number of curves which had a R^2 value higher than 0.9 was 10698 for measurement in dark and 10264 under illumination. These values were taken as 100 % and the percentage of each conduction mechanism was calculated according to that. As already mentioned, the majority of the curves showed best fitting with Schottky emission model: respectively 64.97 % and

63.48 % in dark and under illumination. Charge carrier transfer by hopping conduction is the second dominating conduction mechanism: 18.75 % and 19.39 % in dark and under illumination respectively.

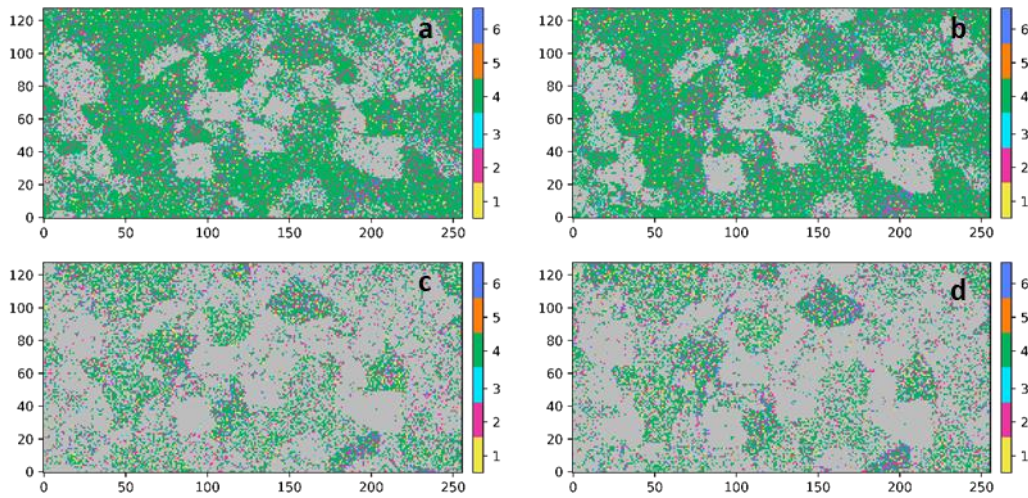


Figure 42. Mapping of charge carrier transport mechanism, a) in dark, b) under illumination conditions, c) $R^2 > 0.9$ in the dark and d) $R^2 > 0.9$ under illumination. Yellow color represents the F-N tunneling, magenta hopping conduction, turquoise PF emission, green Schottky emission, orange SCLC and blue thermionic field emission.

Table 8. Curves that have $R^2 > 0.90$. Measurements with Au coated probe.

Transport mechanism	LED OFF		LED ON	
	Number	Percentage %	Number	Percentage %
F-N tunneling	566	5.29	524	5.11
Hopping	2006	18.75	1990	19.39
P-F emission	131	1.22	110	1.07
Schottky emission	6951	64.97	6516	63.48
SCLC	178	1.66	195	1.90
Termionic field emission	866	8.09	932	9.08
All	10698	100	10264	100

Similar measurements were also performed with Pt coated probes. An array of 51 x 128 I-V curves was captured with the same measurement parameters as used with Au coated probe. A summary of the results is presented on *Table 9*. Similar to the measurements conducted with Au probe, Schottky emission is the predominant electron transport mechanism with, 62.71 and 62.51 % in the dark and under illumination, followed by hopping conduction with 22.87 and 21.15 % in the dark and under illumination.

Table 9. Curves that have $R^2 > 0.90$. Measurements with Pt coated probe.

Transport mechanism	LED OFF		LED ON	
	Number	Percentage %	Number	Percentage %
F-N tunneling	34	1.45	29	1.37
Hopping	536	22.87	448	21.15
P-F emission	80	3.42	82	3.87
Schottky emission	1468	62.71	1324	62.51
SCLC	45	1.92	39	1.84
Termionic field emission	178	7.60	196	9.25
All	2341	100	2118	100

Current instabilities at the tip and sample nanocontact

Fluctuations on the I-V curves measured across the AFM tip and sample contact can have various origins. One of the most common sources of this variability is the degradation of the nanosized AFM tip. This can happen as a result of high load which leads to mechanical wear of the tip coating, resulting in the decrease of conductivity or in the total removal of the conductive coating. Nevertheless, high peak force is essential to get a stable electrical contact between the tip and the sample, e.g. to penetrate the water layer on the sample when measuring in ambient conditions [174]. For instance, when the I-V curves map was captured using 50 nN peak force only 12.3 % of the curves in dark and 10.0 % of the curves under illumination had $R^2 > 0.9$ whereas with 150 nN peak force these numbers were 32.6 % and 31.3 % accordingly. Using even higher peak force setpoint than 150 nN could lead to even better I-V curve quality with low instabilities, but would also increase the probability of mechanical wear of the tip.

Melting of the tip apex as a result of high current flowing between the tip and the sample is another origin of the current instabilities. A Pt coated probe loses its conductivity when the currents in the range of μA flow between the probe and the tip [28]. In this work current was limited to 5.2 nA in order to avoid the melting of the tip apex. From the conductivity calibration curves on the *Figure 44* and *Figure 45* it can be seen that the probe is still conductive after the measurements with some minor decrease in the conductivity.

Environmental aspects, mainly the presence of a water layer on the sample surface, also influence the conductivity. Due to the water meniscus formed at the tip and sample contact, applying positive bias can lead to local anodic oxidation of the surface at the tip/sample contact [28], [173], [177], [178]. As in this work stoichiometric TiO_2 was studied, further oxidation of the sample can be excluded. Nevertheless, processes like ionic transport and water dissociation can still influence the current stability [178].

As the Au and Pt coated probes were still conductive after the measurements (*Figure 44* and *Figure 45*), total removal of the tip coating or melting of the tip apex can be excluded. Furthermore, the beginning and the end of the *Figure 38b* (Hold segment slice) both demonstrate the same magnitude of current, which is another indication that the tip did not lose its conductivity during the imaging. Nevertheless, fluctuations and instabilities of the measured current were still observed, (see *Figure 43*). These may originate from insufficient water layer penetration, water dissociation, minor degradation of the tip apex as well as due to the impurities that the tip collects during the measurement [174].

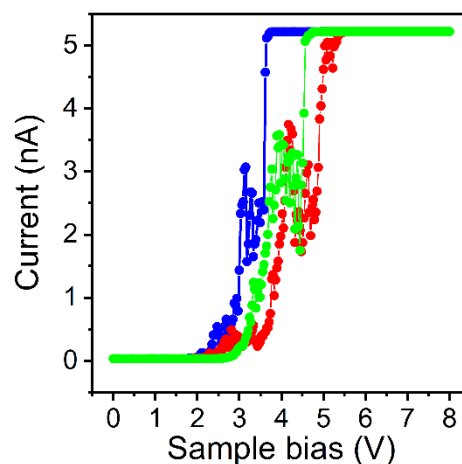


Figure 43. Current instabilities at the Au coated probe and TiO_2 interface.

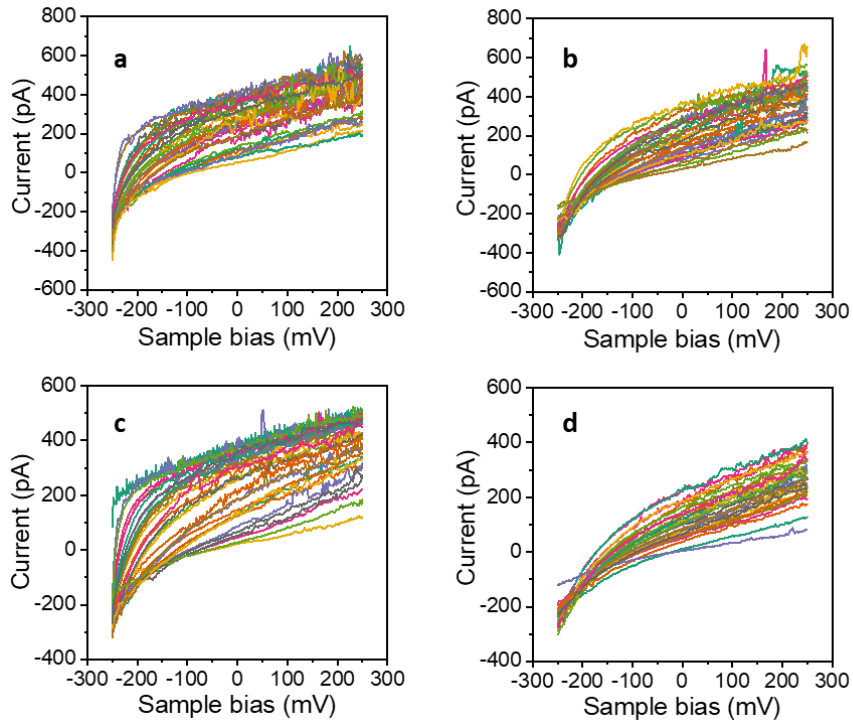


Figure 44. Calibration of the Au coated probe conductivity on freshly cleaved HOPG. Before the measurements with 50 nN peak force (a) and after the measurements (b). Before the measurements with 150 nN peak force (c) and after the measurements (d).

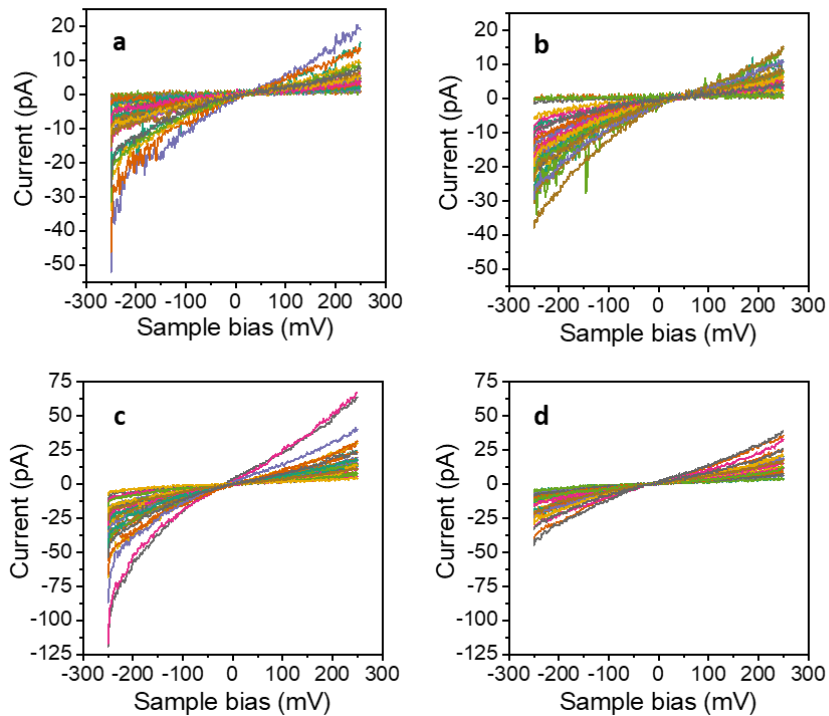


Figure 45. Calibration of the Pt coated probe conductivity on freshly cleaved HOPG. Before the measurements with 50 nN peak force (a) and after the measurements (b). Before the measurements with 150 nN peak force (c) and after the measurements (d).

In conclusion, fitting I-V curves measured at each AFM pixel with various conduction models, revealed the dominant current transport mechanism occurring between the metal tip and fully crystalline TiO₂ sample. As expected, most of the majority charge carrier transport occurs through Schottky emission, which is the most common conduction mechanism in Schottky barrier junctions. Measurements obtained done using both Au- and Pt-coated probes, in both cases leading to similar results. Nevertheless, further analysis is needed in order to confirm or discard other possible conduction mechanisms.

4.4 Degradation of amorphous phase on partially crystalline TiO₂ thin films

In this chapter we observed the loss of an amorphous phase on a partially crystalline TiO₂ samples by comparing the AFM topography images captured before and after the electrochemical studies in the conventional EC cell. To follow the degradation in-situ, electrochemical studies were conducted in AFM-EC cell followed by topography imaging. AFM-EC measurements were carried out in dark and under illumination conditions, using different light intensities as well as wavelengths. The corrosion rate was calculated for each study to reveal the conditions that have the highest impact on the degradation of the amorphous phase.

During the photoelectrochemical characterization of TiO₂ thin films it was observed that photocurrents improved on the partially crystalline samples [120]. On Figure 46 it can be seen that the improvement in photocurrent was significant when cathodic conditions (-0.7 to +0.3 V vs OCP) was applied.

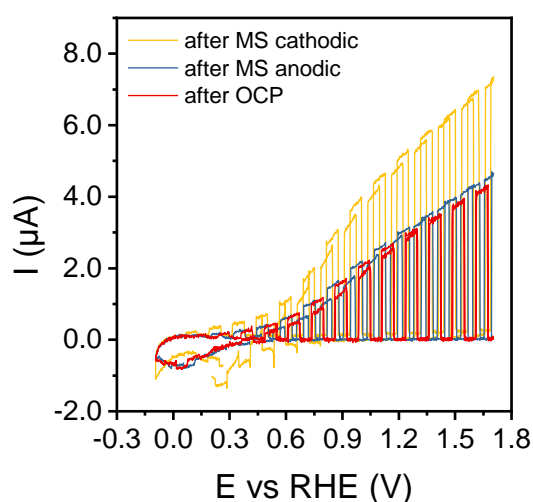


Figure 46. Improvements in photocurrents after photoelectrochemical characterization of mixed phase 40 nm TiO₂ thin film on n⁺⁺Si substrate.

In order to investigate the origin of the improved photocurrents, topography as-deposited, as well as after photoelectrochemical characterizations, was measured on the partially crystalline 40 and 75 nm TiO₂ thin film samples. The mostly amorphous as-deposited 40 nm sample (Figure 47a-b) has pyramidal-shape crystalline protrusions with an average diameter of 300 nm and approximate height of 10 nm. The as-deposited 75 nm sample (Figure 47c-d) is mostly crystalline with amorphous areas in between which are not clearly identified on the topography image, but are recognizable from the adhesion map (see Figure A. 6).

AFM topography on the samples that had undergone photoelectrochemical characterization is shown in Figure 3. The samples were studied as photoanodes in 0.5 M H₂SO₄ electrolyte and under simulated solar illumination (AM1.5G). On the 40 nm sample (Figure 48a-b) the height of the pyramidal shape crystallites has increased from 10 nm for as-deposited sample, to 30 nm. This is a clear evidence that the amorphous phase has degraded to some extent, as we have recently reported for fully amorphous samples [161]. On the 75 nm sample, pinholes have formed on the areas containing amorphous phase.

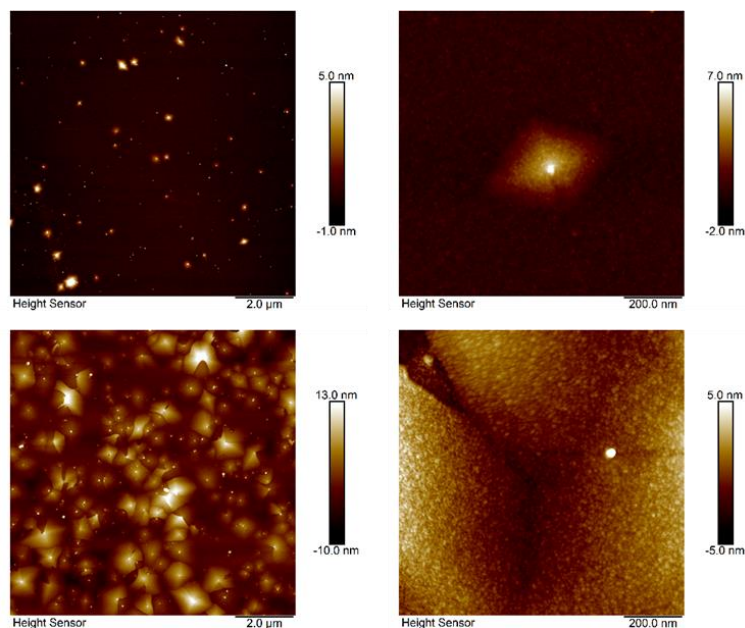


Figure 47. **a, b:** As-deposited, 40 nm ALD TiO₂ on n⁺⁺ Si and **c, d:** as-deposited, 75 nm ALD TiO₂ on n⁺⁺ Si. Images a and c were obtained with 10 μm scan size, images b and d with 1.0 μm scan size.

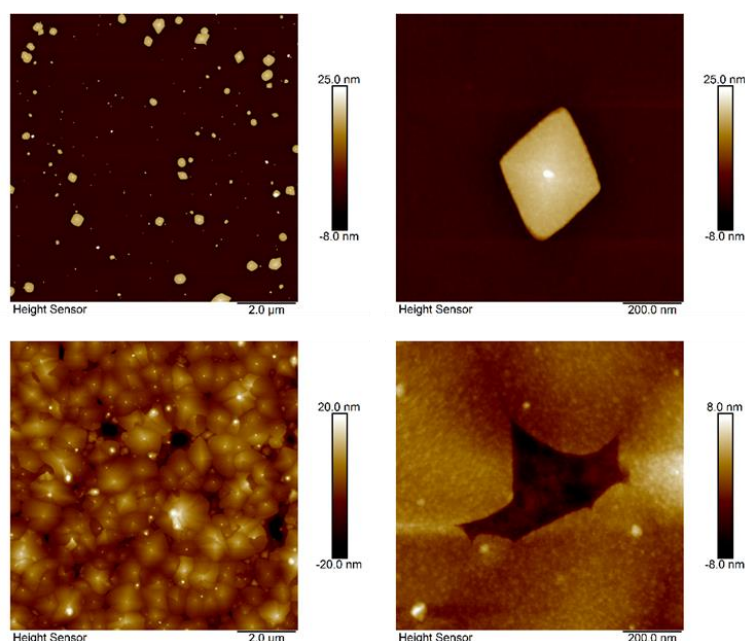


Figure 48. 40 nm TiO₂ (**a, b**) and 75 nm TiO₂ (**c, d**) on n⁺⁺ Si after photoelectrochemical measurements. Images a and c are taken with 10 μm scan size, images b and d with 1.0 μm scan size.

In order to investigate the changes taking place on the partially crystalline samples during photoelectrochemical studies, *in-situ* EC-AFM measurements were performed.

Different (photo)electrochemical conditions relevant to water splitting photoanodes were tested to get an initial impression of their influence on the degradation of TiO₂ (Figure 49 and Table 10). A series of 30 min treatments were carried out in the in-house built EC-AFM cell (see Figure A. 7), in acidic media, in the dark and under illumination (365 nm, 68.64 mW cm⁻²), both at 0 and +1.2 V vs RHE. After every treatment, an AFM topography image was captured, and the average change in the height of the amorphous phase was recorded. The largest loss of amorphous material was observed when the

sample was illuminated while applying anodic bias of +1.2 V vs RHE. Therefore, these conditions were chosen as a base for further investigation.

Table 10. Preliminary exploration of the sensitivity of the TiO₂ degradation to the experimental conditions.

Scans	LED Lamp Status	Potentiostat (all E shown are V vs RHE)
3-4	LIGHT ON (365 nm), 30 min	OCP
4-5	DARK	CV, 20 mV/s, OCP -> to 1.7 V, 3 cycles
5-6	DARK	CA, 1.2 V, 30 min
6-7	LIGHT ON (365 nm), 30 min	CA, 1.2 V, 30 min
7-8	DARK	CA, 0.0 V, 30 min
8-9	LIGHT ON (365 nm), 30 min	CA, 0.0 V, 30 min
9-10	DARK	CV, 20 mV/s, OCP -> to 1.7 V, 3 cycles

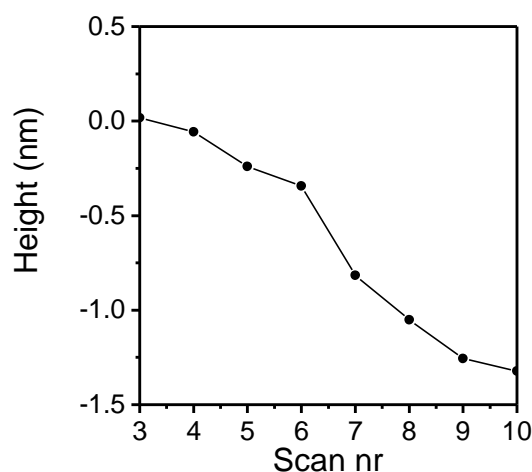


Figure 49. Preliminary exploration of the sensitivity of the TiO₂ degradation to the experimental conditions. Change in height of the amorphous film after each step in the experiment series described in *Table 10*.

4.4.1 Influence of photoelectrochemical conditions on degradation rates

A series of *in-situ* degradation studies were carried out with 40 and 75 nm thin film TiO₂ samples, each study consisting of several successive *treatments* of equal duration, at 1.2 V vs RHE under illumination, with equilibration periods between the treatments at open circuit potential (OCP) in dark. Treatment durations of 15, 30 and 60 minutes as well as several equilibration periods were explored. During the equilibration periods, AFM topography images were captured in order to record the evolution of the sample surface. Height profiles were extracted digitally from each topography image in two regions, each region containing both crystalline and amorphous phase (ROI: Regions Of Interest) using data analysis software (Bruker Nanoscope Analysis), and superimposed using the crystalline area as a reference point (*Figure 50*). Examples of topography and height profiles taken on 40 and 75 nm sample can be found in the appendix. The crystalline areas were unaffected by the treatment conditions (see discussion below) as evidenced by the perfect matching of the topography profiles on the crystallite surfaces. Hence the superposition procedure enables a direct quantification of the gradual loss of amorphous phase. The degradation rate was calculated by dividing the height reduction in the amorphous fraction over the total treatment time within each study. The parameters for each study

are summarized in *Table 11*. Examples of the AFM height profiles used to quantify the degradation are shown in *Figure 50*.

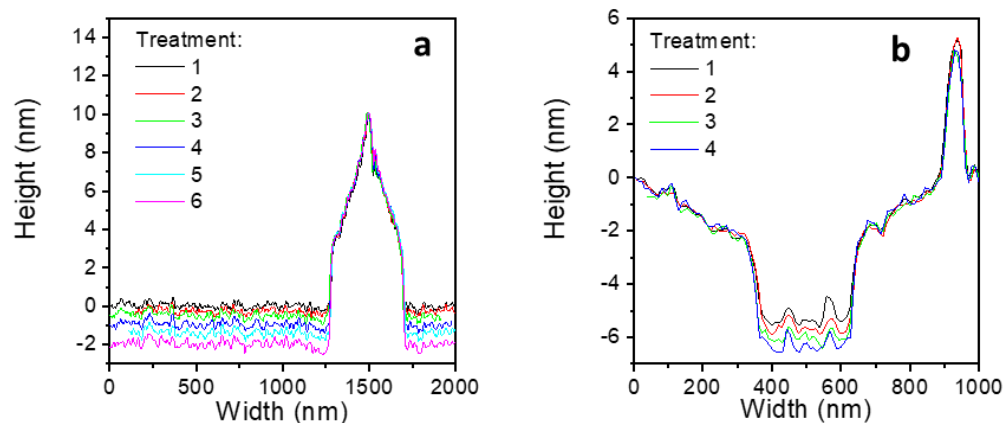


Figure 50. Examples of AFM height profiles used to directly quantify the degradation of amorphous fraction in partially crystalline TiO₂ layers under photoelectrochemical conditions. Left side image: selected profiles on a 40 nm sample, sample 1, study 1, with a degradation rate of 0.86 nm per hour. Right side image: 75 nm sample, sample 2, study 7, degradation rate of 0.35 nm per hour.

Table 11. Summary of the *in-situ* degradation studies in this work.

Sample	Study	d_{nomi} (nm)	LED wave-length (nm)	I (mW cm ⁻²)	t_{treat} (min)	N_{treat}	t_{equi} (min)	Degradation rate (nm h ⁻¹)			
								ROI 1 avg	ROI 2 avg	Sum avg	Sum sd
1	1	40	365	68.64	30	5	30	0.78	0.93	0.86	0.12
	2				60	3	30	0.66	0.60	0.63	0.21
	3				15	7	15	0.79	0.74	0.77	0.06
	4				15	5	30	0.73	0.86	0.79	0.06
2	5	75	365	68.64	15	6	30	0.72	0.90	0.81	0.06
	6				30	5	30	0.38	0.48	0.43	0.14
	7				60	3	30	0.35	0.34	0.35	0.06
	8				15	6	30	0.65	0.62	0.63	0.14
3	9	40	365	0	60	1	30	0.130	0.204	0.19	0.05
	0.176			60	2	30	0.137	0.174	0.16	0.05	
3	12	40	1050	15.76	30	3	30	0.205	0.345	0.275	0.08

d_{nomi} : nominal thickness of the TiO₂ film. I : irradiance on sample position; t_{treat} : treatment duration; N_{treat} : number of treatments; t_{equi} : equilibration time allowed between treatments; ROI: Region Of Interest: a crystallite surrounded by amorphous material for 40 nm samples, an amorphous region surrounded by crystallites for 75 nm samples. avg: average; sd: standard deviation.

Treatment duration. For both sample thicknesses it was found that the degradation rate was similar through the whole study (each treatment within one study had a similar degradation rate). Hence increasing the number of treatments within a study did not affect the degradation rate. Increasing the *treatment duration*, on the other hand, resulted in significantly lower average degradation rates, as would be expected for a diffusion-limited mechanism.

Time between studies. For successive *studies* on the same sample, the degradation rate was higher for the initial studies, and decreased with further etching. Repeating the study with shorter treatment duration (studies 1 and 4, and 5 and 8, see *Table 11*) resulted in higher degradation, but the initial degradation rate was not recovered. Faster degradation during the initial etching studies might be attributed to impurities on the top layers of the film resulting from the ALD deposition process. However, our recent observations [161] on purely amorphous coatings synthesized under the same conditions showed no significant difference between surface and bulk degradation. More plausibly, the increasing passivation at deeper etchings, observed for mixed phase layers in this work, may be caused by titanium species formed from the amorphous material dissolved during photoactivated degradation. These species would adsorb on the coating surface during the time in-between studies, creating a thin protective layer. It is known that the presence of even small amounts of sulfate inhibits the breakdown of the passivating TiO₂ layer (and thus the corrosion) of anodically polarized titanium in halide solutions. This has been attributed to the preferential adsorption of doubly charged sulfate ions [179], [180]. In our experiments, despite exhaustive rinsing of the sample with ultrapure water after each study, a thin residual layer of diluted sulfuric acid solution remained on the surface. This is evidenced by XPS spectra, which showed the presence of a sulfur 2p peak (*Figure 51a-b*). This peak disappears after sample surface bombardment with Ar cluster ion beam. The adsorbed sulfate is increasingly probable for electrolyte trapped within the pinholes being formed during treatments on the 75 nm sample, but can be expected for the 40 nm samples as well. As this residual solution evaporates and concentrates, initially further corrosion, and at higher concentrations, surface adsorption of sulfates [181], [182] could take place. This process would both etch the sample further before the start of the next study, and inhibit corrosion on subsequent studies. While this passivation effect was not observed for purely amorphous samples under simulated sunlight illumination, where temperature would increase more than 10 Kelvin within 1 hour, in the conditions studied in this work, where temperature increase is kept to a minimum (see below), the solubility of adsorbates would be correspondingly low, contributing to the passivation effect. In other words, while in warm sulfuric acid electrolyte both chemical degradation of amorphous TiO₂ and photoactivated degradation occur [161], in room temperature sulfuric acid chemical degradation is minimal, and photodegradation seems to be gradually inhibited by sulfate adsorption. Due to this progressive passivation, the degradation rates in *Table 11* must be considered relatively, and not as absolute values.

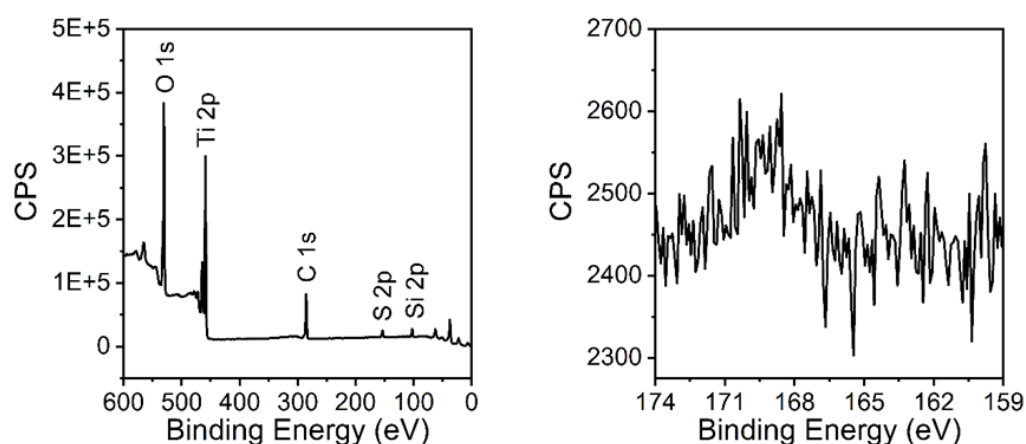


Figure 51. On the left XPS survey spectrum and on the right zoom on S 2p peak. This peak disappears after removing the superficial layers of the sample by sputtering with Ar⁺ ions.

For the 75 nm sample it should be furthermore taken into account that as the pinholes grow deeper, reduced light exposure to these areas would locally produce less photogenerated holes, resulting in lower photocorrosion at deeper etchings. Note that this is evidence for *local* origin of the photoholes involved in the degradation of the amorphous phase: that is, photoholes generated on the crystalline surface would contribute mostly to water splitting, while photoholes generated on the amorphous phase would be mostly consumed in the photocorrosion process.

4.4.2 Evolution of roughness

AFM roughness measurements show that degradation takes place homogeneously on the amorphous surface. *Figure 52* shows the evolution of the arithmetic average surface roughness (Ra) for the whole scan, as well as for the amorphous area only, obtained on height sensor images. The average roughness for the whole image increases during each study, due to the increase in height difference between crystalline and amorphous areas. On the amorphous fraction, however (*Figure 52b*), Ra values stay almost constant within each study. For studies 3 and 4 Ra values on the amorphous areas decrease due to cleaning/removing of impurities on the sample surface (see *Figure A. 10*). For the pristine (not-degraded) 40 nm sample, the roughness on the amorphous area is lower than on the fully amorphous samples deposited at 100 °C, 0.142 nm and 0.230 nm respectively [161]. After the last study (study nr. 4) the roughness of the amorphous area has reached 0.238 nm which is similar to a not-degraded fully amorphous sample. The whole-scan roughness measurements show additional evidence of sample change *in-between studies* (see final roughness after study 1, and initial roughness after study 2), as would be expected by further etching in between studies by a residual electrolyte layer.

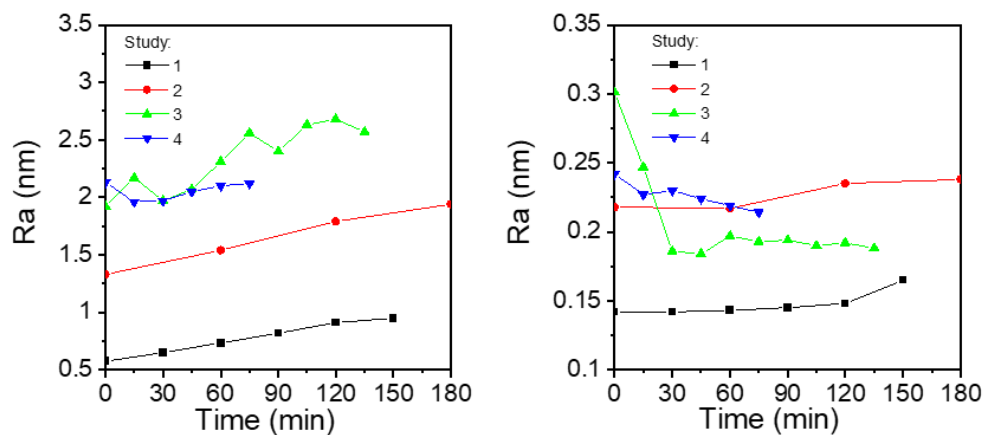


Figure 52. Evolution of nm-scale arithmetic average surface roughness (Ra) for a 40 nm sample, measured **a.** for the full image and **b.** for the amorphous fraction only.

Light intensity. On a pristine (not-degraded) 40 nm sample, two additional studies were performed at lower illumination intensities (0 and 0.176 mW/cm². See *Table 11*, studies 9 and 10). An irradiance of 0.176 mW/cm² was chosen as a non-saturation intensity (see *Figure A. 11*). As expected for a photoactivated process, higher irradiance results in higher degradation rate. Studies were also performed on 40 nm samples using LEDs centered at 565 (study nr 11 is not presented in the *Table 11* as the degradation was too low to calculate the degradation rates with method used in this work) and 1050 nm wavelength (study nr 12). Contrary to the observations at 365 nm, no significant degradation was detected at longer wavelengths. Consequently, photogeneration from absorption in the degenerately doped silicon substrate can be neglected as a source for corrosion.

Temperature. Additionally, an *in-situ* cell was assembled with a thermocouple in the position of the sample, and the temperature evolution was recorded during several subsequent illumination treatments, with treatment durations of 60 minutes for 365 nm wavelength and 30 minutes for 1050 nm wavelength LED. Under these illumination conditions, the cell temperature increased only about 0.3 and 0.2 °C accordingly (see *Figure A. 12*). This is in contrast with our previous observations under full simulated sunlight [161], where the cell temperature would increase between 10 and 15 Kelvin during treatments of similar duration. Hence, as previously mentioned, the contribution of chemical degradation route can be considered minimal in the conditions explored in this work.

Tafel polarization curves for the mixed amorphous/crystalline sample were obtained in the dark and under illumination (see *Figure A. 13*). Measurements were carried out in four steps, starting with scanning from OCP to 1.4 V in dark and under illumination, followed by scanning from OCP to -0.2 V in dark and under illumination. Between each step the OCP was recorded until stabilized. By extrapolating the Tafel slopes, corrosion current (I_{corr}), polarization resistance (R_p) as well as anodic and cathodic Tafel slopes (β_a , β_c) were calculated and are given in *Table 12*. Under illumination I_{corr} increased by a factor of two and E_{corr} decreased 348 mV, which both indicate faster corrosion under illumination. R_p , which shows the specimen resistance to oxidation and was calculated using the Stern-Geary equation:

$$R_p = \frac{\beta_a \beta_c}{2.303 I_{corr} (\beta_a + \beta_c)}$$

is also notably lower when under illumination [183]–[185]. These results confirm photocorrosion as the main degradation process for these samples under the conditions investigated.

Table 12. Parameters obtained from Tafel extrapolation. Measurements were done in dark and under illumination in 0.5 M H₂SO₄, with the scan rate of 2 mV/s.

Irradiance (mW/cm ²)	R_p (kΩ/cm ²)	I_{corr} (A/cm ²)	E_{corr} (V vs RHE)	β_a (V/dec)	β_c (V/dec)
0	45345	3.09E-9	0.398	1.10	0.456
68.64	440	1.02E-7	0.050	0.185	0.236

These experiments reveal, under controlled photoelectrochemical conditions in which chemical degradation can be neglected, significant photocorrosion for the amorphous phase of TiO₂, in mixed phase films synthesized by atomic layer deposition. Preferential degradation can be attributed the disordered structure of the amorphous material, which results in both highly elongated, weaker Ti-O bonds [45], and in extended carrier trapping in defect states [186]. Contrastingly, for the crystalline TiO₂ phase, the water splitting reaction successfully competes with photodecomposition [187], and no degradation could be measured in the time scale of our experiments.

In conclusion, we have employed AFM for the in-situ study of the degradation of amorphous phase on mixed crystalline/amorphous TiO₂ thin films. Using measurement parameters similar to the working conditions of water splitting photoanodes, by applying positive voltage (+1.2 V vs RHE) and illuminating with light of 365 nm wavelength, which has high enough energy to produce photogenerated charge carriers in the TiO₂ film, the crystalline phase remained unchanged, whereas the amorphous phase degraded considerably. Corrosion was studied in dark, as well as under non-saturating (partial band flattening) and under saturating (band flattening) light intensity, with the latter having the highest

degradation rate. Since the change in temperature in the AFM-EC cell was below 1°C during these corrosion studies, chemical corrosion can be considered minimal. Additional studies were conducted with higher wavelengths, 565 and 1050 nm, which both resulted in low degradation rate compared with the studies carried out with 365 nm wavelength. Thus, the contribution of charge carriers originating on the degenerately doped silicon substrate can be neglected. These studies revealed that, while in the crystalline phase the photogenerated holes are mostly used to propel the water-splitting reaction, in the amorphous TiO₂ regions the photogenerated holes are consumed in the photocorrosion process.

5. Conclusion and outlook

In the present thesis, different AFM based methods, in particular CAFM, KPFM and EC-AFM, were employed to investigate the (photo)electrical and (photo)electrochemical characteristics of a series of thin TiO₂ coatings prepared by atomic layer deposition. The applicability of different AFM techniques has been demonstrated in four chapters: *i)* studying the effect of surface morphology on sample photoactivity, *ii)* mapping the surface potential variations and the trapping/detrapping of photogenerated charge carriers on mixed amorphous and crystalline phase TiO₂ samples, *iii)* analyzing charge carrier transport mechanisms at the metal tip and fully crystalline TiO₂ Schottky nanocontact, and *iv)* investigating the stability of the mixed phase TiO₂ films.

High resolution AFM images gave an insight into the growth morphologies of ALD deposited TiO₂ thin films. Topography maps a) revealed the formation of initial anatase seeds in the amorphous matrix, b) demonstrated the evolution of roughness with increasing film thickness and c) enabled the estimation of the percentage of crystallized area on mostly amorphous samples.

CAFM measurements under illumination revealed heterogeneities in the surface photocurrent. Selective Pt photodeposition and high resolution topography showed that the variations in photoactivity are governed by the difference in the crystallographic orientation and faceting. Four main crystallite surface types were distinguished on the fully crystalline TiO₂ thin films, based on high spatial resolution topography and photocurrent measurements, supported by selective photodeposition experiments. EBSD data indicated that there is no preferential growth direction on the fully crystalline samples. Correlative studies with AFM and EBSD, on the same region of interest of the sample surface, confirmed the hypothesis that certain grain types have a similar crystallographic direction.

Further analysis is needed in order to fully determine the nature of the different exposed facets on the surface. Additional correlative studies with CAFM, EBSD and TEM would further help to confirm the higher photoactivity of certain directions and facets.

KPFM technique was used to calculate the surface photovoltage (SPV), for both amorphous and crystalline phase TiO₂. Upon illumination it was observed that the amorphous phase requires more time to reach the steady-state condition, as compared to the crystalline phase. After photoelectric charge injection, even after several hours in the dark, the amorphous phase has still not reached the initial dark CPD value. Further analysis also revealed a slow potential recovery at the interface between the crystalline and amorphous phase. These investigations confirmed the existence of higher amount of photogenerated charge traps in the amorphous phase and at the interface between the two phases.

The slow CPD recovery after illumination can also be related to the change in wetting properties of the TiO₂ surface upon UV irradiation. It is known that rutile and amorphous TiO₂ change from hydrophobic to superhydrophilic, and that anatase changes from hydrophilic to superhydrophilic, when illuminated with UV light. The UV induced superhydrophilicity occurs within minutes, but after illumination the recovery in dark conditions takes several days until the initial surface wetting properties are reached. The contact angle versus time curves in the dark and under illumination reported in the literature have a very similar shape and timescale, compared with the CPD versus time measurements in this work.

Further investigations are required to determine whether the surface wetting phenomenon contributes to the slow redistribution of photoinjected charge carriers.

Additionally, by comparing CPD maps with topography images, we observed that the larger size of the features on potential maps is not only due to the lift height, but also caused by a tip shape convolution effect, as the front and back angle of the probe differ from each other. This effect should be taken into account to avoid possible misinterpretations.

Spectroscopy mode CAFM was used for I-V curve mapping. The collected curves were fitted with various transport models in order to find out the main charge carrier conduction mechanisms at the metal tip and fully crystalline TiO₂ nanojunction. Maps of different transport mechanisms were obtained with high spatial resolution. The dominant charge carrier transport mechanism observed is Schottky emission, which is also the most commonly reported mechanism in Schottky barrier junctions. Measurements were done using both Au and Pt coated probes, leading to similar results.

Fitting the curves with different current mechanisms is an initial approach, but is not enough to confirm or reject additional transport mechanisms. Further analysis is in progress in order to confirm the results obtained. In addition, temperature and light intensity dependent I-V curve measurements will also help to narrow down the selection of possible transport mechanisms present. Furthermore, fitting the curves with the Schottky emission expression under reverse bias is in progress, in order to obtain Schottky barrier height (SBH) maps with high spatial resolution.

Finally, we observed a loss of amorphous phase on partially crystalline TiO₂ samples by comparing the high resolution AFM images before and after photoelectrochemical studies in a conventional PEC cell. The increased relative height of the protruding crystalline phase on the mostly amorphous samples, and the formation of pinholes on the mostly crystalline samples, were a clear indication that the amorphous phase had degraded to some extent. EC-AFM was used to follow this degradation *in-situ* by using measurement parameters similar to the working conditions of water splitting photoanodes. A positive voltage (+1.2 V vs RHE) was applied, and the sample was illuminated with light of 365 nm wavelength, which has high enough energy to produce photogenerated charge carriers in the TiO₂ film. Studies were conducted in the dark, as well as under non-saturating (partial band flattening) and under saturating (band flattening) light intensity, with the latter having the highest degradation rate. Since the change in temperature in the AFM-EC cell was below 1 °C during these corrosion studies, chemical corrosion can be considered minimal. Additional studies were conducted with longer wavelengths, 565 and 1050 nm, which both resulted in low degradation rate compared with the studies carried out with 365 nm wavelength. Therefore, the contribution to photocorrosion from holes originating from light adsorption in the degenerately doped silicon substrate can be neglected. These studies revealed that, while in the crystalline phase the photogenerated holes are mostly used to propel the water-splitting reaction, in amorphous TiO₂ the photoholes are consumed in the photocorrosion process.

Since one of the applications for the amorphous TiO₂ is as a protection layer for photoanode materials that are more efficient, expensive and/or less stable than TiO₂, care should be taken to either use fully crystalline coatings, or to select operating conditions that minimize photodegradation.

6. Appendix

6.1 Physicochemical properties

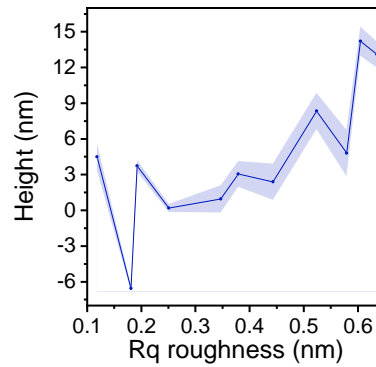


Figure A. 1. Correlation between the height and RMS roughness. Faded area is the standard deviation.

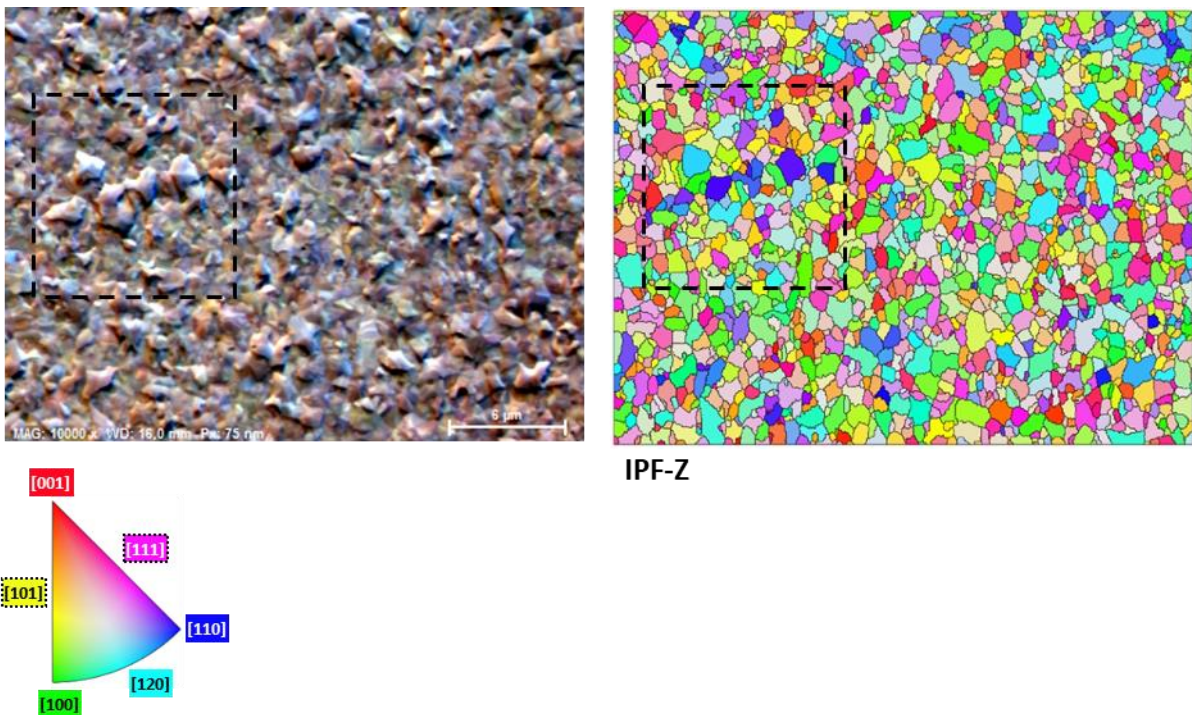


Figure A. 2. SEM and IPF-Z maps. Black dotted square presents the area where the AFM scan was taken. On the bottom is the IPF-Z color key.

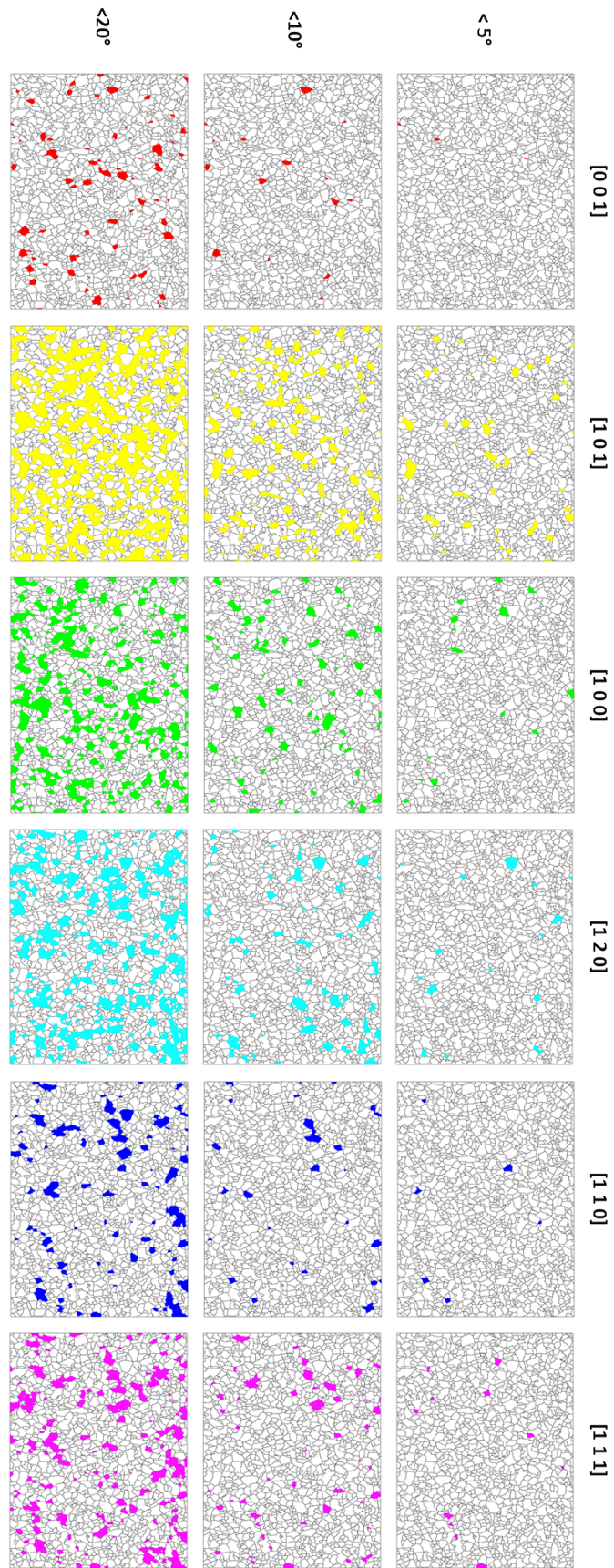


Figure A. 3. Map of grains with $[001]$, $[101]$, $[100]$, $[120]$, $[110]$ and $[111]$ direction when allowing 5, 10 and 20° of misorientation.

6.2 Surface voltage mapping

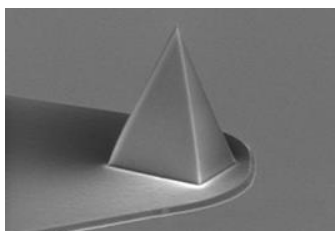


Figure A. 4. SEM image of the PFQNE-AL probe. Image taken from Bruker website (<https://www.brukerafmprobes.com/p-3817-pfqne-al.aspx>).

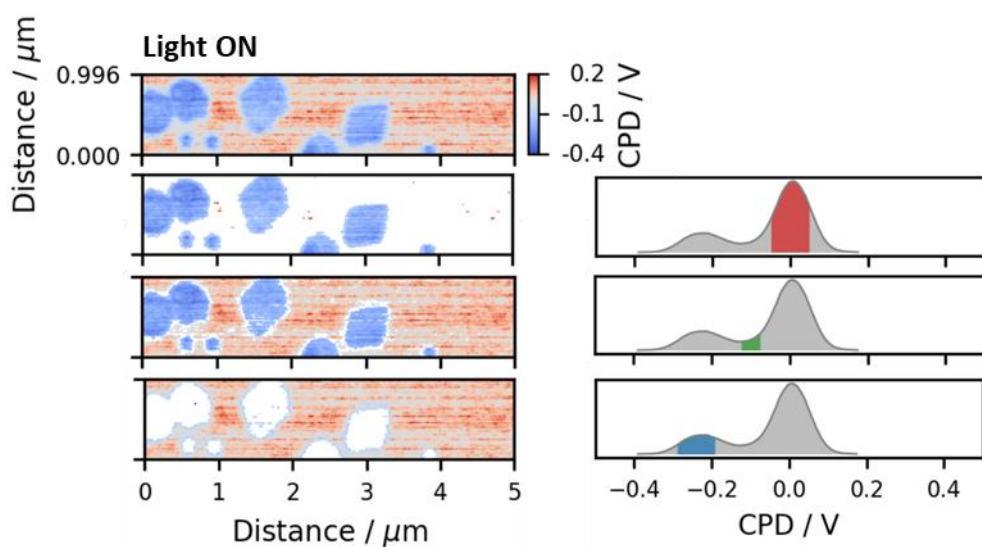


Figure A. 5. Additional representations of *Figure 35c* (sample after switching the light ON). In the CPD maps on the left, different ranges of data have been masked (white pixels) to identify fractions of the sample with specific potential values. In the corresponding (Savitzky-Golay smoothed) histograms on the right, the masked points are highlighted in color. Red: fraction with higher CPD (amorphous phase); blue: fraction with lower CPD (crystalline inclusions); green: fraction with intermediate CPD values (amorphous/crystalline interface).

6.3 Degradation of amorphous phase on partially crystalline TiO₂ thin films

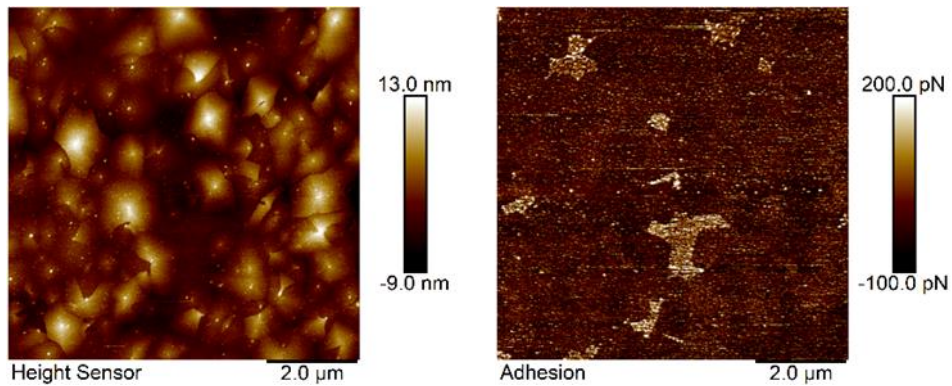


Figure A. 6. High-resolution topography measured in 0.5 M H₂SO₄ (a) and simultaneously recorded adhesion map (b). Adhesion force between AFM tip and amorphous domains is higher than on the crystalline area.

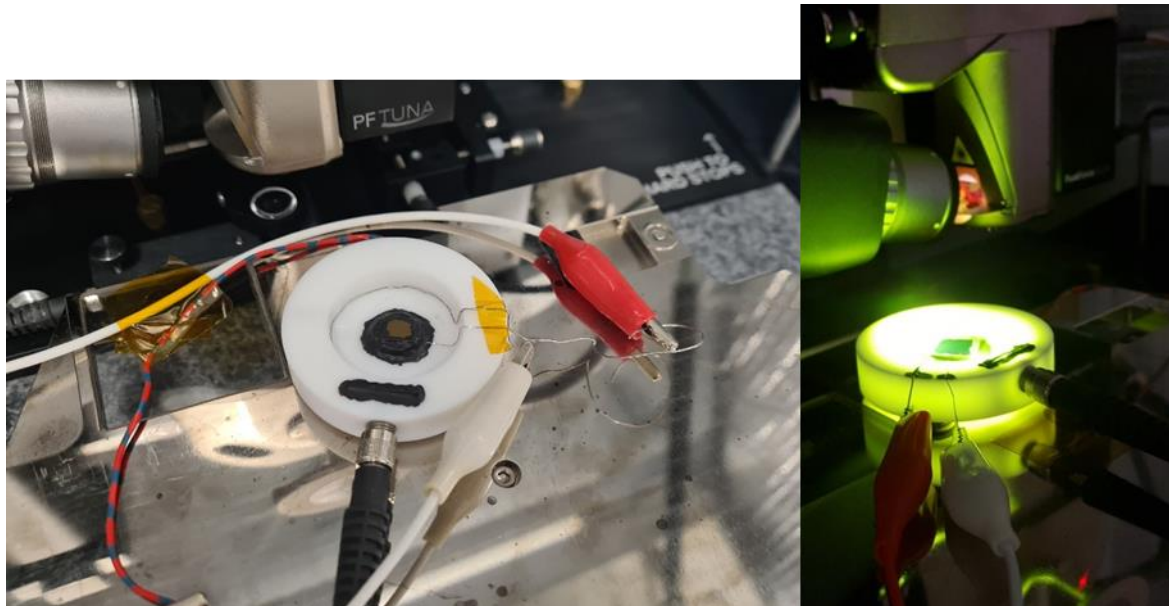


Figure A. 7. In-house built cell used for *in-situ* experiments in this work. LED light is introduced on the cell with a polarization resistant fiber optic cable (600 μm core diameter, 0.22 numerical aperture) for side illumination on the sample under investigation. The Teflon construction ensures both stability and diffuse reflection of light not directly reaching the sample.

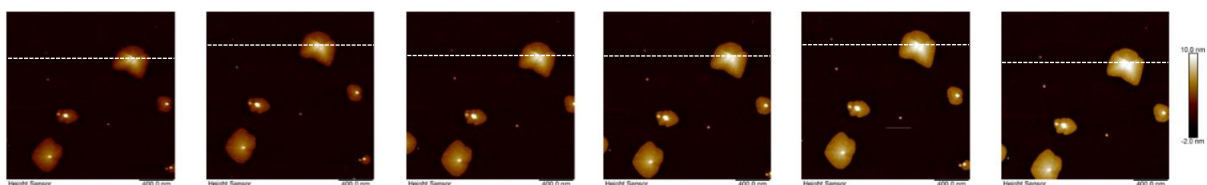


Figure A. 8. Topography and height profiles on 40 nm sample, Study nr 1 on Table 11.

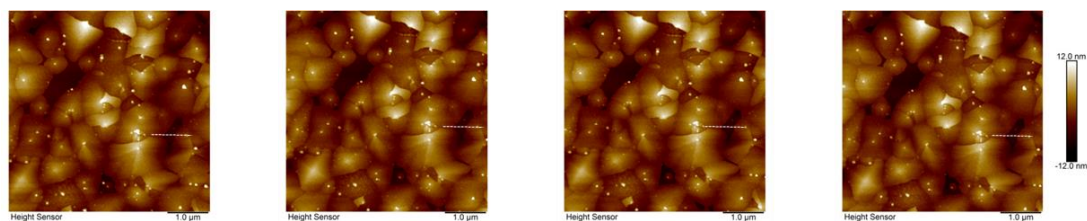


Figure A. 9. Topography and height profiles on 75 nm sample, Study nr 7 on *Table 11*.

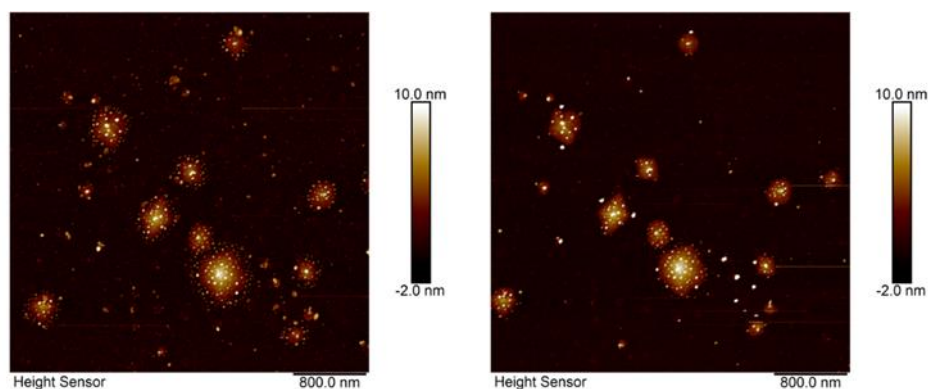


Figure A. 10. Sample before treatments (a) and sample after 30 minutes under 1.2 V and illumination (b). After applying positive bias and illuminating the sample, many of the impurities on amorphous matrix are removed.

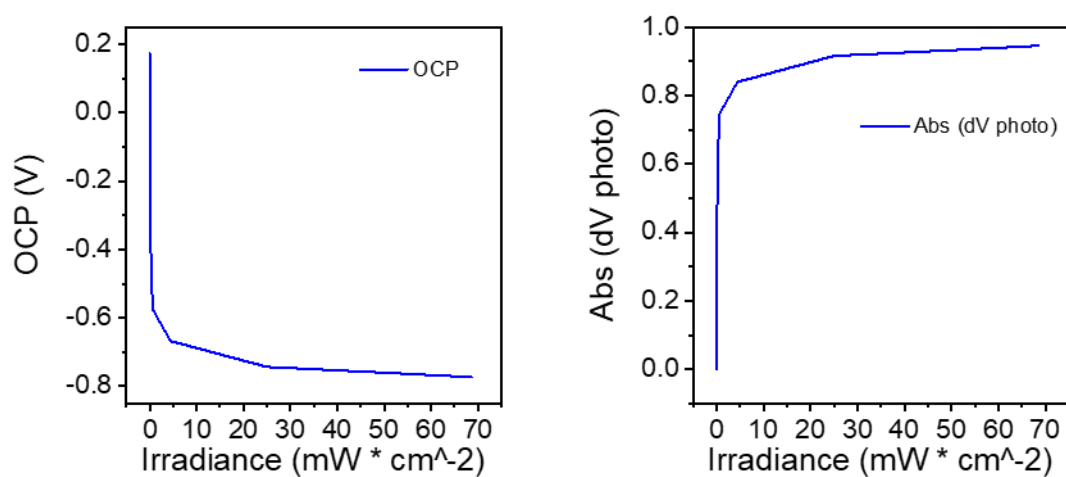


Figure A. 11. Open circuit potential and absolute change in photovoltage vs irradiance. It can be seen that the band flattening potential is achieved around 30 mW*cm⁻².

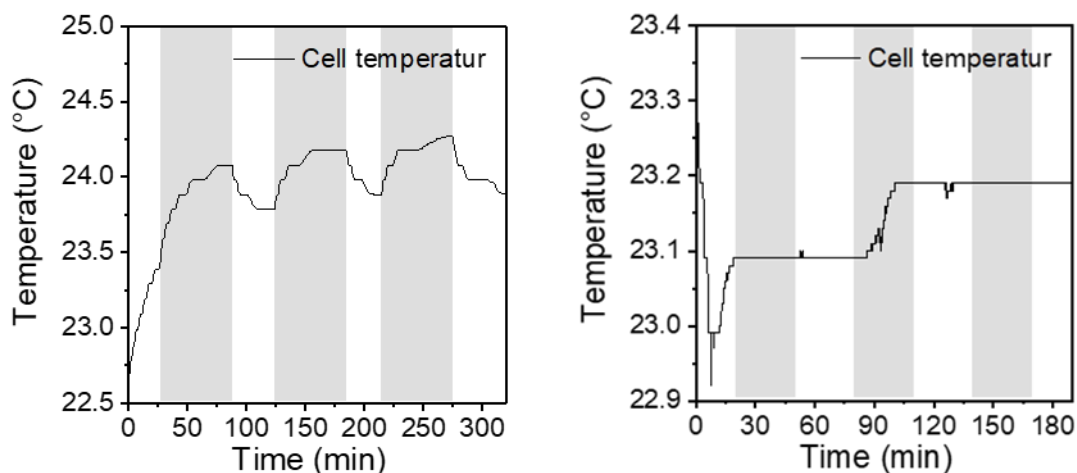


Figure A. 12. Temperature evolution in the *in-situ* electrochemical AFM cell (AFM-EC) during studies consisting of successive illumination treatments. A thermocouple was placed in position where the sample would be. The cell was filled with ultrapure water, and illuminated with LED light centered at **a**: 365 nm, with an irradiance of 68.64 mW cm^{-2} and **b**: 1050 nm, with an irradiance of 15.76 mW cm^{-2} . In both cases, the irradiance was measured on the sample position with an absolutely calibrated spectrometer. Gray shaded areas represent the illumination ("treatment") duration of 60 minutes for 365 nm LED and 30 minutes for 1050 nm LED. These were the longest treatment times for both LEDs explored in this work. The time in-between treatments was 30 minutes. Under these illumination conditions, the cell temperature increased only about $0.3 \text{ }^\circ\text{C}$ when illuminating with 365 nm LED for 60 minutes and less than $0.2 \text{ }^\circ\text{C}$ when illuminating with 1050 nm LED for 30 minutes.

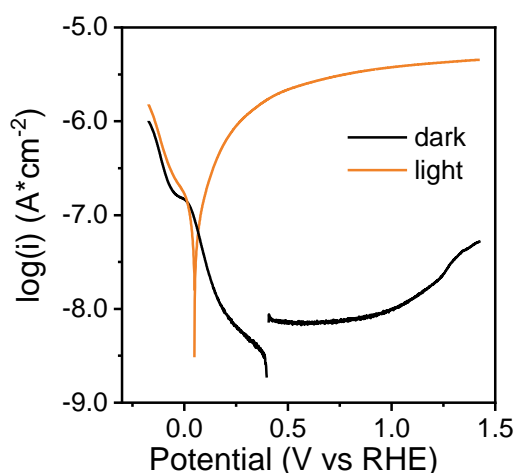


Figure A. 13. Tafel extrapolation curves of mixed crystalline/amorphous TiO_2 thin film. First the measurement in dark under anodic potential vs OCP was done, followed by the measurement under illumination at anodic potential. Last but not least, cathodic potential vs OCP was applied and the measurement in dark followed by the measurement under illumination was taken.

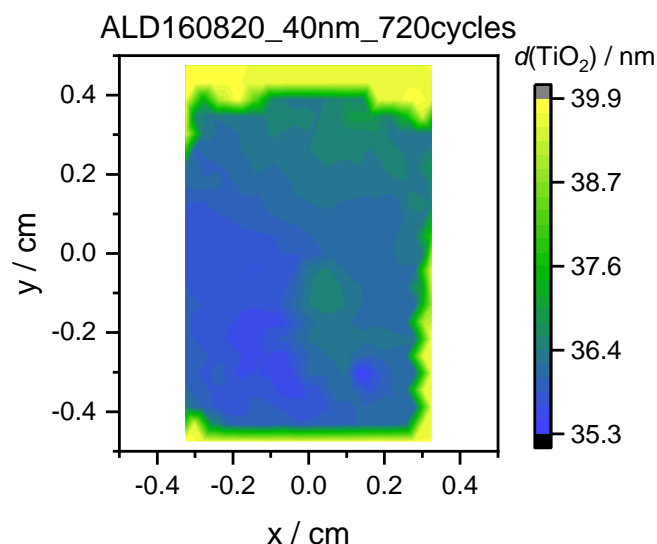


Figure A. 14. Difference in film thickness between the area that was degraded and the area that was not exposed to electrolyte was also verified by performing spectroscopic ellipsometry on J.A. Woollam RC2® ellipsometer. Angle of incidence was 60° and fitting range 400-2500 nm. Layer thickness was modelled with Cauchy relation for > 400 nm range. From figure 5 it can be seen that the layer thickness on the area that was not exposed to electrolyte is close to 40 nm as expected. Film thickness in the area where the photoelectrochemical measurements were performed has a height variation of 35.5-36.5 nm. This variation is due to side illumination setup. Nevertheless, the area exposed to electrolyte is rather homogeneously degraded.

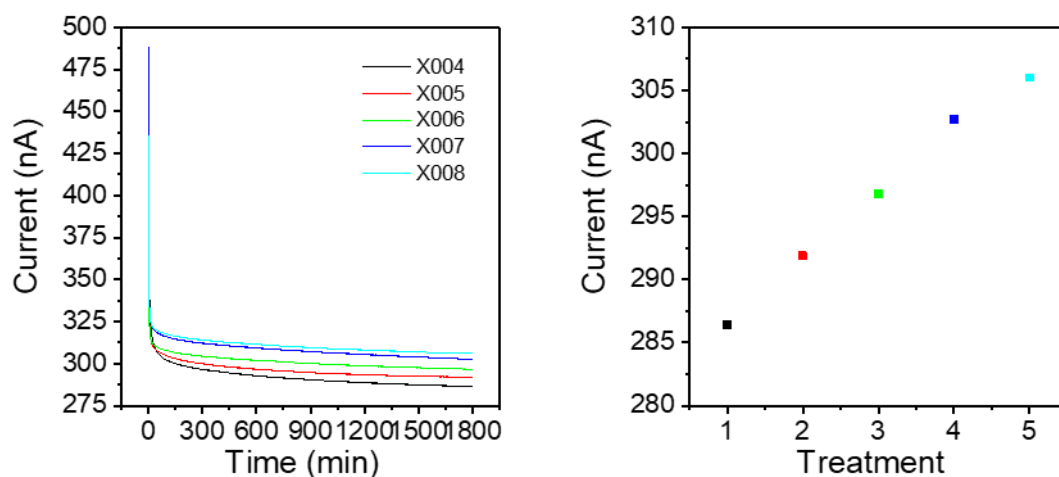


Figure A. 15. Chronoamperometry curves for the first study on 40 nm sample (a) and end current values for each curve (b).

7. References

- [1] “H2 Energy to generate green hydrogen from hydropower in Aarau,” *Fuel Cells Bulletin*, vol. 2016, no. 7, p. 8, Jul. 2016, doi: 10.1016/S1464-2859(16)30181-X.
- [2] “Shell, Mitsubishi Heavy Industries, Vattenfall and Wärme Hamburg Sign Letter of Intent for 100MW Hydrogen Project in Hamburg,” *hamburg.de*. <https://www.hamburg.de/pressearchiv-fhh/14847344/2021-01-22-hydrogen-project-hamburg-moorburg/> (accessed Apr. 29, 2021).
- [3] V. Franzitta, D. Curto, D. Rao, and A. Viola, “Hydrogen Production from Sea Wave for Alternative Energy Vehicles for Public Transport in Trapani (Italy),” *Energies*, vol. 9, p. 850, Oct. 2016, doi: 10.3390/en9100850.
- [4] R. Sánchez-Dirzo, R. G. González-Huerta, E. Mendoza, R. Silva, and J. M. Sandoval Pineda, “From wave to jet and from jet to hydrogen: A promising hybrid system,” *International Journal of Hydrogen Energy*, vol. 39, no. 29, pp. 16628–16636, Oct. 2014, doi: 10.1016/j.ijhydene.2014.03.134.
- [5] R. van de Krol and B. A. Parkinson, “Perspectives on the photoelectrochemical storage of solar energy,” *MRS Energy & Sustainability*, vol. 4, ed 2017, doi: 10.1557/mre.2017.15.
- [6] S. Haussener, S. Hu, C. Xiang, A. Z. Weber, and N. S. Lewis, “Simulations of the irradiation and temperature dependence of the efficiency of tandem photoelectrochemical water-splitting systems,” *Energy Environ. Sci.*, vol. 6, no. 12, pp. 3605–3618, Nov. 2013, doi: 10.1039/C3EE41302K.
- [7] S. Tembhurne and S. Haussener, “Integrated Photo-Electrochemical Solar Fuel Generators under Concentrated Irradiation II. Thermal Management a Crucial Design Consideration,” *J. Electrochem. Soc.*, vol. 163, no. 10, pp. H999–H1007, Jan. 2016, doi: 10.1149/2.0321610jes.
- [8] A. L. Linsebigler, G. Lu, and J. T. Yates, “Photocatalysis on TiO₂ Surfaces: Principles, Mechanisms, and Selected Results,” *Chem. Rev.*, vol. 95, no. 3, pp. 735–758, May 1995, doi: 10.1021/cr00035a013.
- [9] P. Salvador, “Hole diffusion length in n-TiO₂ single crystals and sintered electrodes: Photoelectrochemical determination and comparative analysis,” *Journal of Applied Physics*, vol. 55, no. 8, pp. 2977–2985, Apr. 1984, doi: 10.1063/1.333358.
- [10] J. Eichhorn *et al.*, “Nanoscale imaging of charge carrier transport in water splitting photoanodes,” *Nature Communications*, vol. 9, no. 1, p. 2597, Jul. 2018, doi: 10.1038/s41467-018-04856-8.
- [11] A. J. E. Rettie *et al.*, “Combined Charge Carrier Transport and Photoelectrochemical Characterization of BiVO₄ Single Crystals: Intrinsic Behavior of a Complex Metal Oxide,” *J. Am. Chem. Soc.*, vol. 135, no. 30, pp. 11389–11396, Jul. 2013, doi: 10.1021/ja405550k.
- [12] G. Zheng *et al.*, “Tungsten oxide nanostructures and nanocomposites for photoelectrochemical water splitting,” *Nanoscale*, vol. 11, no. 41, pp. 18968–18994, Oct. 2019, doi: 10.1039/C9NR03474A.
- [13] T. Lopes, L. Andrade, F. L. Formal, M. Gratzel, K. Sivula, and A. Mendes, “Hematite photoelectrodes for water splitting: evaluation of the role of film thickness by impedance spectroscopy,” *Phys. Chem. Chem. Phys.*, vol. 16, no. 31, pp. 16515–16523, Jul. 2014, doi: 10.1039/C3CP55473B.
- [14] B. Klahr, S. Gimenez, F. Fabregat-Santiago, J. Bisquert, and T. W. Hamann, “Electrochemical and photoelectrochemical investigation of water oxidation with hematite electrodes,” *Energy Environ. Sci.*, vol. 5, no. 6, pp. 7626–7636, May 2012, doi: 10.1039/C2EE21414H.
- [15] M. Muhibullah and A. Abdel Haleem, “Estimation of the Open Circuit Voltage of a pn Junction Based on Photoelectrochemical Measurements,” *Transactions of the Materials Research Society of Japan*, vol. 40, p. 247, Sep. 2015, doi: 10.14723/tmrj.40.247.
- [16] K. Rajeshwar, “Fundamentals of Semiconductor Electrochemistry and Photoelectrochemistry,” in *Encyclopedia of Electrochemistry*, American Cancer Society, 2007.
- [17] “Semiconductor Electrochemistry, 2nd Edition | Wiley,” *Wiley.com*. <https://www.wiley.com/en-us/Semiconductor+Electrochemistry%2C+2nd+Edition-p-9783527312818> (accessed Apr. 11, 2021).

- [18] Z. Chen, H. Dinh, and E. Miller, *Photoelectrochemical Water Splitting: Standards, Experimental Methods, and Protocols*. New York: Springer-Verlag, 2013.
- [19] R. Memming, "Semiconductor Surfaces and Solid–Solid Junctions," in *Semiconductor Electrochemistry*, John Wiley & Sons, Ltd, 2015, pp. 23–47.
- [20] Z. Zhang and J. T. Yates, "Band Bending in Semiconductors: Chemical and Physical Consequences at Surfaces and Interfaces," *Chem. Rev.*, vol. 112, no. 10, pp. 5520–5551, Oct. 2012, doi: 10.1021/cr3000626.
- [21] M. T. M. Koper, "Thermodynamic theory of multi-electron transfer reactions: Implications for electrocatalysis," *Journal of Electroanalytical Chemistry*, vol. 660, no. 2, pp. 254–260, Sep. 2011, doi: 10.1016/j.jelechem.2010.10.004.
- [22] M. Xiao, B. Luo, Z. Wang, S. Wang, and L. Wang, "Recent Advances of Metal-Oxide Photoanodes: Engineering of Charge Separation and Transportation toward Efficient Solar Water Splitting," *Solar RRL*, vol. 4, no. 8, p. 1900509, 2020, doi: <https://doi.org/10.1002/solr.201900509>.
- [23] B. D. Alexander, P. J. Kulesza, I. Rutkowska, R. Solarska, and J. Augustynski, "Metal oxide photoanodes for solar hydrogen production," *J. Mater. Chem.*, vol. 18, no. 20, pp. 2298–2303, May 2008, doi: 10.1039/B718644D.
- [24] R. van de Krol and M. Grätzel, Eds., *Photoelectrochemical Hydrogen Production*. Springer US, 2012.
- [25] C. Jiang, S. J. A. Moniz, A. Wang, T. Zhang, and J. Tang, "Photoelectrochemical devices for solar water splitting – materials and challenges," *Chem. Soc. Rev.*, vol. 46, no. 15, pp. 4645–4660, Jul. 2017, doi: 10.1039/C6CS00306K.
- [26] B. L. Sharma, *Metal-Semiconductor Schottky Barrier Junctions and Their Applications*. Springer Science & Business Media, 2013.
- [27] A. Di Bartolomeo, "Graphene Schottky diodes: An experimental review of the rectifying graphene/semiconductor heterojunction," *Physics Reports*, vol. 606, pp. 1–58, Jan. 2016, doi: 10.1016/j.physrep.2015.10.003.
- [28] M. Lanza, *Conductive Atomic Force Microscopy: Applications in Nanomaterials*. John Wiley & Sons, 2017.
- [29] M. A. Mastro, "17 - Power MOSFETs and diodes," in *Gallium Oxide*, S. Pearton, F. Ren, and M. Mastro, Eds. Elsevier, 2019, pp. 401–418.
- [30] M. Garg, B. Tak, V. R. Rao, and R. Singh, "Enhanced Performance of MSM UV Photodetectors by Molecular Modification of Gallium Nitride Using Porphyrin Organic Molecules," *IEEE Transactions on Electron Devices*, vol. 66, pp. 1–4, Mar. 2019, doi: 10.1109/TED.2019.2901022.
- [31] M. Garbrecht *et al.*, "Thermally stable epitaxial ZrN/carrier-compensated Sc_{0.99}Mg_{0.01}N metal/semiconductor multilayers for thermionic energy conversion," *J Mater Sci*, vol. 55, no. 4, pp. 1592–1602, Feb. 2020, doi: 10.1007/s10853-019-04127-x.
- [32] S. Bayan and D. Mohanta, "Significant Fowler–Nordheim tunneling across ZnO – Nanorod based nanojunctions for nanoelectronic device applications," *Current Applied Physics*, vol. 13, no. 4, pp. 705–709, Jun. 2013, doi: 10.1016/j.cap.2012.11.009.
- [33] I. Beinik, "Electrical Characterization of Semiconductor Nanostructures by Conductive Probe Based Atomic Force Microscopy Techniques," PhD Thesis, 2011.
- [34] F.-C. Chiu, "A Review on Conduction Mechanisms in Dielectric Films," *Advances in Materials Science and Engineering*, vol. 2014, p. e578168, Feb. 2014, doi: 10.1155/2014/578168.
- [35] E. W. Lim and R. Ismail, "Conduction Mechanism of Valence Change Resistive Switching Memory: A Survey," *Electronics*, vol. 4, pp. 586–613, Sep. 2015, doi: 10.3390/electronics4030586.
- [36] D. Cheon, M. Son, M.-H. Ham, and W. Lee, "Resistive switching in amorphous ZnO dielectric film prepared on Ga-doped ZnO transparent electrode," *RSC Adv.*, vol. 6, Nov. 2016, doi: 10.1039/C6RA21726E.
- [37] C. Ye *et al.*, "Multilevel Conductance Switching of Memory Device through Photoelectric Effect," *Journal of the American Chemical Society*, vol. 134, Nov. 2012, doi: 10.1021/ja305354y.

- [38] W. Xu, A. Chin, L. Ye, C. Z. Ning, and H. Yu, "Charge transport and trap characterization in individual GaSb nanowires," *Journal of Applied Physics*, vol. 111, no. 10, p. 104515, May 2012, doi: 10.1063/1.4720080.
- [39] F. A. Padovani and R. Stratton, "Field and thermionic-field emission in Schottky barriers," *Solid-State Electronics*, vol. 9, no. 7, pp. 695–707, Jul. 1966, doi: 10.1016/0038-1101(66)90097-9.
- [40] "Metal-Semiconductor Contacts," in *Physics of Semiconductor Devices*, John Wiley & Sons, Ltd, 2006, pp. 134–196.
- [41] S. Munjal and N. Khare, "Valence Change Bipolar Resistive Switching Accompanied With Magnetization Switching in CoFe₂O₄ Thin Film," *Scientific Reports*, vol. 7, Sep. 2017, doi: 10.1038/s41598-017-12579-x.
- [42] C. Hamann, H. Burghardt, and T. Frauenheim, *Electrical Conduction Mechanisms in Solids*. John Wiley & Sons Incorporated, 1988.
- [43] Z. A. Weinberg, "On tunneling in metal-oxide-silicon structures," *Journal of Applied Physics*, vol. 53, no. 7, pp. 5052–5056, Jul. 1982, doi: 10.1063/1.331336.
- [44] W. Frammelsberger, G. Benstetter, R. Stamp, J. Kiely, and T. Schweinboeck, "Simplified tunnelling current calculation for MOS structures with ultra-thin oxides for conductive atomic force microscopy investigations," *Materials Science and Engineering: B*, vol. 116, no. 2, pp. 168–174, Jan. 2005, doi: 10.1016/j.mseb.2004.09.027.
- [45] B. Sarker and S. Khondaker, "Thermionic Emission and Tunneling at Carbon Nanotube-Organic Semiconductor Interface," *ACS nano*, vol. 6, pp. 4993–9, May 2012, doi: 10.1021/nn300544v.
- [46] A. Fujishima and K. Honda, "Electrochemical Photolysis of Water at a Semiconductor Electrode," *Nature*, vol. 238, no. 5358, Art. no. 5358, Jul. 1972, doi: 10.1038/238037a0.
- [47] T. Berger, D. Monllor-Satoca, M. Jankulovska, T. Lana-Villarreal, and R. Gómez, "The Electrochemistry of Nanostructured Titanium Dioxide Electrodes," *ChemPhysChem*, vol. 13, no. 12, pp. 2824–2875, 2012, doi: <https://doi.org/10.1002/cphc.201200073>.
- [48] J. Wang, X. Liu, R. Li, P. Qiao, L. Xiao, and J. Fan, "TiO₂ nanoparticles with increased surface hydroxyl groups and their improved photocatalytic activity," *Catalysis Communications*, vol. 19, pp. 96–99, Mar. 2012, doi: 10.1016/j.catcom.2011.12.028.
- [49] M. Jankulovska, T. Berger, S. S. Wong, R. Gómez, and T. Lana-Villarreal, "Trap States in TiO₂ Films Made of Nanowires, Nanotubes or Nanoparticles: An Electrochemical Study," *ChemPhysChem*, vol. 13, no. 12, pp. 3008–3017, 2012, doi: <https://doi.org/10.1002/cphc.201200072>.
- [50] J. Fan *et al.*, "Enhanced Photovoltaic Performance of Nanowire Dye-Sensitized Solar Cells Based on Coaxial TiO₂@TiO Heterostructures with a Cobalt(II/III) Redox Electrolyte," *ACS Appl. Mater. Interfaces*, vol. 5, no. 20, pp. 9872–9877, Oct. 2013, doi: 10.1021/am402344d.
- [51] T. Sh. Atabaev, M. A. Hossain, D. Lee, H.-K. Kim, and Y.-H. Hwang, "Pt-coated TiO₂ nanorods for photoelectrochemical water splitting applications," *Results in Physics*, vol. 6, pp. 373–376, Jan. 2016, doi: 10.1016/j.rinp.2016.07.002.
- [52] H. Chen, G. Liu, and L. Wang, "Switched photocurrent direction in Au/TiO₂ bilayer thin films," *Sci Rep*, vol. 5, p. 10852, Jun. 2015, doi: 10.1038/srep10852.
- [53] T. W. Kim and K.-S. Choi, "Improving Stability and Photoelectrochemical Performance of BiVO₄ Photoanodes in Basic Media by Adding a ZnFe₂O₄ Layer," *J. Phys. Chem. Lett.*, vol. 7, no. 3, pp. 447–451, Feb. 2016, doi: 10.1021/acs.jpcllett.5b02774.
- [54] D. Eisenberg, H. S. Ahn, and A. J. Bard, "Enhanced Photoelectrochemical Water Oxidation on Bismuth Vanadate by Electrodeposition of Amorphous Titanium Dioxide," *J. Am. Chem. Soc.*, vol. 136, no. 40, pp. 14011–14014, Oct. 2014, doi: 10.1021/ja5082475.
- [55] J. A. Seabold and K.-S. Choi, "Efficient and Stable Photo-Oxidation of Water by a Bismuth Vanadate Photoanode Coupled with an Iron Oxyhydroxide Oxygen Evolution Catalyst," *J. Am. Chem. Soc.*, vol. 134, no. 4, pp. 2186–2192, Feb. 2012, doi: 10.1021/ja209001d.
- [56] F. F. Abdi and R. van de Krol, "Nature and Light Dependence of Bulk Recombination in Co-Pi-Catalyzed BiVO₄ Photoanodes," *J. Phys. Chem. C*, vol. 116, no. 17, pp. 9398–9404, May 2012, doi: 10.1021/jp3007552.

- [57] S. P. Berglund, D. W. Flaherty, N. T. Hahn, A. J. Bard, and C. B. Mullins, "Photoelectrochemical Oxidation of Water Using Nanostructured BiVO₄ Films," *J. Phys. Chem. C*, vol. 115, no. 9, pp. 3794–3802, Mar. 2011, doi: 10.1021/jp1109459.
- [58] J. Eichhorn *et al.*, "Revealing Nanoscale Chemical Heterogeneities in Polycrystalline Mo-BiVO₄ Thin Films," *Small*, vol. 16, no. 35, p. 2001600, 2020, doi: <https://doi.org/10.1002/sml.202001600>.
- [59] C. Wolpert *et al.*, "Aerosol-Deposited BiVO₄ Photoelectrodes for Hydrogen Generation," *J Therm Spray Tech*, Nov. 2020, doi: 10.1007/s11666-020-01104-8.
- [60] P. Dias, A. Vilanova, T. Lopes, L. Andrade, and A. Mendes, "Extremely stable bare hematite photoanode for solar water splitting," *Nano Energy*, vol. 23, pp. 70–79, May 2016, doi: 10.1016/j.nanoen.2016.03.008.
- [61] K. Sivula, F. Le Formal, and M. Grätzel, "Solar Water Splitting: Progress Using Hematite (α -Fe₂O₃) Photoelectrodes," *ChemSusChem*, vol. 4, no. 4, pp. 432–449, 2011, doi: <https://doi.org/10.1002/cssc.201000416>.
- [62] T.-Y. Yang *et al.*, "A new hematite photoanode doping strategy for solar water splitting: oxygen vacancy generation," *Phys. Chem. Chem. Phys.*, vol. 15, no. 6, pp. 2117–2124, Jan. 2013, doi: 10.1039/C2CP44352J.
- [63] Y. Wei *et al.*, "Enhanced Photoelectrochemical Water-Splitting Effect With a Bent ZnO Nanorod Photo Anode Decorated With Ag Nanoparticles," *Nanotechnology*, vol. 23, p. 235401, May 2012, doi: 10.1088/0957-4484/23/23/235401.
- [64] I. S. Mohamad, S. Ismail, M. N. Norizan, S. A. Zainol Murad, and M. M. A. B. Abdullah, "ZnO Photoanode Effect on the Efficiency Performance of Organic Based Dye Sensitized Solar Cell," May 2017, vol. 209, doi: 10.1088/1757-899X/209/1/012028.
- [65] B.-S. Wang *et al.*, "An overlapping ZnO nanowire photoanode for photoelectrochemical water splitting," *Catalysis Today*, vol. 321–322, pp. 100–106, Feb. 2019, doi: 10.1016/j.cattod.2018.02.028.
- [66] C. Haisch, J. Schneider, M. Fleisch, H. Gutzmann, T. Klassen, and D. W. Bahnemann, "Cold sprayed WO₃ and TiO₂ electrodes for photoelectrochemical water and methanol oxidation in renewable energy applications," *Dalton Trans.*, vol. 46, no. 38, pp. 12811–12823, Oct. 2017, doi: 10.1039/C7DT02063E.
- [67] J. Y. Zheng *et al.*, "Facile Fabrication of WO₃ Nanoplates Thin Films with Dominant Crystal Facet of (002) for Water Splitting," *Crystal Growth & Design*, vol. 14, no. 11, pp. 6057–6066, Nov. 2014, doi: 10.1021/cg5012154.
- [68] J. Su, X. Feng, J. D. Sloppy, L. Guo, and C. A. Grimes, "Vertically Aligned WO₃ Nanowire Arrays Grown Directly on Transparent Conducting Oxide Coated Glass: Synthesis and Photoelectrochemical Properties," *Nano Lett.*, vol. 11, no. 1, pp. 203–208, Jan. 2011, doi: 10.1021/nl1034573.
- [69] C. Fàbrega *et al.*, "Efficient WO₃ photoanodes fabricated by pulsed laser deposition for photoelectrochemical water splitting with high faradaic efficiency," *Applied Catalysis B: Environmental*, vol. 189, pp. 133–140, Jul. 2016, doi: 10.1016/j.apcatb.2016.02.047.
- [70] H. Gerischer, "Photocatalysis in aqueous solution with small TiO₂ particles and the dependence of the quantum yield on particle size and light intensity," *Electrochimica Acta*, vol. 40, no. 10, pp. 1277–1281, Jul. 1995, doi: 10.1016/0013-4686(95)00058-M.
- [71] J.-G. Li, T. Ishigaki, and X. Sun, "Anatase, Brookite, and Rutile Nanocrystals via Redox Reactions under Mild Hydrothermal Conditions: Phase-Selective Synthesis and Physicochemical Properties," *J. Phys. Chem. C*, vol. 111, no. 13, pp. 4969–4976, Apr. 2007, doi: 10.1021/jp0673258.
- [72] T. A. Kandiel, A. Feldhoff, L. Robben, R. Dillert, and D. W. Bahnemann, "Tailored Titanium Dioxide Nanomaterials: Anatase Nanoparticles and Brookite Nanorods as Highly Active Photocatalysts," *Chem. Mater.*, vol. 22, no. 6, pp. 2050–2060, Mar. 2010, doi: 10.1021/cm903472p.

- [73] D.-H. Kim, W.-S. Kim, S. Kim, and S.-H. Hong, "Brookite TiO₂ Thin Film Epitaxially Grown on (110) YSZ Substrate by Atomic Layer Deposition," *ACS Appl. Mater. Interfaces*, vol. 6, no. 15, pp. 11817–11822, Aug. 2014, doi: 10.1021/am501656r.
- [74] M. Zhang, G. Lin, C. Dong, and L. Wen, "Amorphous TiO₂ films with high refractive index deposited by pulsed bias arc ion plating," *Surface and Coatings Technology*, vol. 201, no. 16, pp. 7252–7258, May 2007, doi: 10.1016/j.surfcoat.2007.01.043.
- [75] H. H. Pham and L.-W. Wang, "Oxygen vacancy and hole conduction in amorphous TiO₂," *Phys. Chem. Chem. Phys.*, vol. 17, no. 1, pp. 541–550, Dec. 2014, doi: 10.1039/C4CP04209C.
- [76] H. Takikawa, T. Matsui, T. Sakakibara, A. Bendavid, and P. J. Martin, "Properties of titanium oxide film prepared by reactive cathodic vacuum arc deposition," *Thin Solid Films*, vol. 348, no. 1, pp. 145–151, Jul. 1999, doi: 10.1016/S0040-6090(99)00054-1.
- [77] M. Hezam, S. Qaid, I. Bedja, F. Alharbi, M. Nazeeruddin, and A. Aldwayyan, "Synthesis of Pure Brookite Nanorods in a Nonaqueous Growth Environment," *Crystals*, vol. 9, p. 562, Oct. 2019, doi: 10.3390/cryst9110562.
- [78] A. Mamakhel, J. Yu, F. Søndergaard-Pedersen, P. Hald, and B. B. Iversen, "Facile synthesis of brookite TiO₂ nanoparticles," *Chem. Commun.*, vol. 56, no. 95, pp. 15084–15087, Dec. 2020, doi: 10.1039/D0CC06795D.
- [79] S. Challagulla, R. Nagarjuna, R. Ganesan, and S. Roy, "TiO₂ synthesized by various routes and its role on environmental remediation and alternate energy production," *Nano-Structures & Nano-Objects*, vol. 12, pp. 147–156, Oct. 2017, doi: 10.1016/j.nanoso.2017.10.002.
- [80] T. Luttrell, S. Halpegamage, J. Tao, A. Kramer, E. Sutter, and M. Batzill, "Why is anatase a better photocatalyst than rutile? - Model studies on epitaxial TiO₂ films," *Scientific Reports*, vol. 4, p. 4043, Feb. 2014, doi: 10.1038/srep04043.
- [81] M. Batzill, "Fundamental aspects of surface engineering of transition metal oxide photocatalysts," *Energy Environ. Sci.*, vol. 4, no. 9, pp. 3275–3286, Aug. 2011, doi: 10.1039/C1EE01577J.
- [82] X.-Q. Gong and A. Selloni, "Reactivity of Anatase TiO₂ Nanoparticles: The Role of the Minority (001) Surface," *J. Phys. Chem. B*, vol. 109, no. 42, pp. 19560–19562, Oct. 2005, doi: 10.1021/jp055311g.
- [83] U. Diebold, N. Ruzycski, G. S. Herman, and A. Selloni, "One step towards bridging the materials gap: surface studies of TiO₂ anatase," *Catalysis Today*, vol. 85, no. 2, pp. 93–100, Oct. 2003, doi: 10.1016/S0920-5861(03)00378-X.
- [84] R. L. Penn and J. Banfield, "Morphology development and crystal growth in nanocrystalline aggregates under hydrothermal conditions: insights from titania," 1999, doi: 10.1016/S0016-7037(99)00037-X.
- [85] M. V. Dozzi and E. Selli, "Specific Facets-Dominated Anatase TiO₂: Fluorine-Mediated Synthesis and Photoactivity," *Catalysts*, vol. 3, no. 2, pp. 455–485, Jun. 2013, doi: 10.3390/catal3020455.
- [86] H. Xu *et al.*, "Anatase TiO₂ Single Crystals Exposed with High-Reactive {111} Facets Toward Efficient H₂ Evolution," *Chem. Mater.*, vol. 25, no. 3, pp. 405–411, Feb. 2013, doi: 10.1021/cm303502b.
- [87] U. Diebold, "The surface science of titanium dioxide," *Surface Science Reports*, vol. 48, no. 5, pp. 53–229, Jan. 2003, doi: 10.1016/S0167-5729(02)00100-0.
- [88] M. Lazzeri, A. Vittadini, and A. Selloni, "Structure and Energetics of Stoichiometric TiO₂ Anatase Surfaces," *Phys. Rev. B*, vol. 63, Mar. 2001, doi: 10.1103/PhysRevB.63.155409.
- [89] T. Inoue, A. Fujishima, S. Konishi, and K. Honda, "Photoelectrocatalytic reduction of carbon dioxide in aqueous suspensions of semiconductor powders," *Nature*, vol. 277, pp. 637–638, Feb. 1979, doi: 10.1038/277637a0.
- [90] J. Choi, H. Zhang, and J. H. Choi, "Modulating Optoelectronic Properties of Two-Dimensional Transition Metal Dichalcogenide Semiconductors by Photoinduced Charge Transfer," *ACS Nano*, vol. 10, no. 1, pp. 1671–1680, Jan. 2016, doi: 10.1021/acsnano.5b07457.

- [91] D. Kim *et al.*, “Dissimilar anisotropy of electron versus hole bulk transport in anatase TiO₂ : Implications for photocatalysis,” *Physical Review B*, vol. 95, Jan. 2017, doi: 10.1103/PhysRevB.95.045209.
- [92] S. Hu, M. R. Shaner, J. A. Beardslee, M. Lichterman, B. S. Brunschwig, and N. S. Lewis, “Amorphous TiO₂ coatings stabilize Si, GaAs, and GaP photoanodes for efficient water oxidation,” *Science*, vol. 344, no. 6187, pp. 1005–1009, May 2014, doi: 10.1126/science.1251428.
- [93] M. G. Ahmed, I. E. Kretschmer, T. A. Kandiel, A. Y. Ahmed, F. A. Rashwan, and D. W. Bahnemann, “A Facile Surface Passivation of Hematite Photoanodes with TiO₂ Overlayers for Efficient Solar Water Splitting,” *ACS Appl. Mater. Interfaces*, vol. 7, no. 43, pp. 24053–24062, Nov. 2015, doi: 10.1021/acsami.5b07065.
- [94] A. J. Bard and M. S. Wrighton, “Thermodynamic Potential for the Anodic Dissolution of n-Type Semiconductors: A Crucial Factor Controlling Durability and Efficiency in Photoelectrochemical Cells and an Important Criterion in the Selection of New Electrode/Electrolyte Systems,” *J. Electrochem. Soc.*, vol. 124, no. 11, p. 1706, Nov. 1977, doi: 10.1149/1.2133140.
- [95] G. Binnig, H. Rohrer, Ch. Gerber, and E. Weibel, “Tunneling through a controllable vacuum gap,” *Appl. Phys. Lett.*, vol. 40, no. 2, pp. 178–180, Jan. 1982, doi: 10.1063/1.92999.
- [96] G. Binnig and H. Rohrer, “Scanning tunneling microscopy---from birth to adolescence,” *Rev. Mod. Phys.*, vol. 59, no. 3, pp. 615–625, Jul. 1987, doi: 10.1103/RevModPhys.59.615.
- [97] G. Binnig, C. F. Quate, and C. Gerber, “The Atomic Force Microscope,” *Physical Review Letters*, vol. 56, pp. 930–933, Mar. 1986, doi: 10.1103/PhysRevLett.56.930.
- [98] B. Voigtländer, *Atomic Force Microscopy*, 2nd ed. Springer International Publishing, 2019.
- [99] U. Celano, “The Atomic Force Microscopy for Nanoelectronics,” in *Electrical Atomic Force Microscopy for Nanoelectronics*, U. Celano, Ed. Cham: Springer International Publishing, 2019, pp. 1–28.
- [100] H. Wang and P. K. Chu, “Chapter 4 - Surface Characterization of Biomaterials,” in *Characterization of Biomaterials*, A. Bandyopadhyay and S. Bose, Eds. Oxford: Academic Press, 2013, pp. 105–174.
- [101] W. Melitz, J. Shen, A. C. Kummel, and S. Lee, “Kelvin probe force microscopy and its application,” *Surface Science Reports*, vol. 66, no. 1, pp. 1–27, Jan. 2011, doi: 10.1016/j.surfrep.2010.10.001.
- [102] H. Fischer, H. Stadler, and N. Erina, “Quantitative temperature-depending mapping of mechanical properties of bitumen at the nanoscale using the AFM operated with PeakForce TappingTM mode,” *Journal of Microscopy*, vol. 250, no. 3, pp. 210–217, 2013, doi: <https://doi.org/10.1111/jmi.12036>.
- [103] Y. Gan, “Atomic and subnanometer resolution in ambient conditions by atomic force microscopy,” *Surface Science Reports*, vol. 64, no. 3, pp. 99–121, Mar. 2009, doi: 10.1016/j.surfrep.2008.12.001.
- [104] “Scanning Probe Microscopy Basics,” in *Scanning Probe Microscopy of Soft Matter*, John Wiley & Sons, Ltd, pp. 9–33.
- [105] H.-J. Butt and M. Jaschke, “Calculation of thermal noise in atomic force microscopy,” *Nanotechnology*, vol. 6, no. 1, pp. 1–7, Jan. 1995, doi: 10.1088/0957-4484/6/1/001.
- [106] Z. Zhong and Y. Lu, “Measurements of surface deformations and strains using an AFM moiré method,” *Measurement*, vol. 38, pp. 34–41, Jul. 2005, doi: 10.1016/j.measurement.2005.02.003.
- [107] H. Habibullah, “30 Years of atomic force microscopy: Creep, hysteresis, cross-coupling, and vibration problems of piezoelectric tube scanners,” *Measurement*, vol. 159, p. 107776, Jul. 2020, doi: 10.1016/j.measurement.2020.107776.
- [108] Y. Wang, J. Kilpatrick, S. Jarvis, F. Boland, A. Kokaram, and D. Corrigan, “Double-Tip Artifact Removal From Atomic Force Microscopy Images,” *IEEE Transactions on Image Processing*, 2016, doi: 10.1109/TIP.2016.2532239.

- [109] A. Méndez-Vilas, M. L. González-Martin, and M. J. Nuevo, "Optical interference artifacts in contact atomic force microscopy images," *Ultramicroscopy*, vol. 92, no. 3–4, pp. 243–250, Aug. 2002.
- [110] L. K. G. C. V. O. D. C. L. L. D. F. R. S. M.R.I., "V. Contact electricity of metals," *The London, Edinburgh, and Dublin Philosophical Magazine and Journal of Science*, vol. 46, no. 278, pp. 82–120, Jul. 1898, doi: 10.1080/14786449808621172.
- [111] "Light-Induced Charge Separation and Surface Photovoltage," in *Surface Photovoltage Analysis of Photoactive Materials*, 0 vols., WORLD SCIENTIFIC (EUROPE), 2019, pp. 1–46.
- [112] D. Luo, H. Sun, and Y. Li, "Kelvin Probe Force Microscopy in Nanoscience and Nanotechnology," in *Surface Science Tools for Nanomaterials Characterization*, C. S. S. R. Kumar, Ed. Berlin, Heidelberg: Springer, 2015, pp. 117–158.
- [113] L. Polak, J. H. Rector, M. J. Slaman, and R. J. Wijngaarden, "NaTaO₃ Photoanode for Bias-Free Water Splitting: A Photo-Electrochemical and Kelvin Probe Surface Photovoltage Study," *J. Phys. Chem. C*, vol. 120, no. 41, pp. 23559–23565, Oct. 2016, doi: 10.1021/acs.jpcc.6b07247.
- [114] P. Schindler *et al.*, "Surface Photovoltage-Induced Ultralow Work Function Material for Thermionic Energy Converters," *ACS Energy Letters*, vol. 4, pp. 2436–2443, Jul. 2019, doi: 10.1021/acsenergylett.9b01214.
- [115] Y. Turkulets and I. Shalish, "Surface properties of semiconductors from post-illumination photovoltage transient," *Surfaces and Interfaces*, vol. 24, p. 101052, Jun. 2021, doi: 10.1016/j.surfin.2021.101052.
- [116] V. W. Bergmann *et al.*, "Real-space observation of unbalanced charge distribution inside a perovskite-sensitized solar cell," *Nature Communications*, vol. 5, no. 1, Art. no. 1, Sep. 2014, doi: 10.1038/ncomms6001.
- [117] S. Sadewasser and N. Nicoara, "Time-Resolved Electrostatic and Kelvin Probe Force Microscopy," in *Springer Series in Surface Sciences*, 2018, pp. 119–143.
- [118] A. Henning *et al.*, "Kelvin probe force microscopy of nanocrystalline TiO₂ photoelectrodes," *Beilstein Journal of Nanotechnology*, vol. 4, no. 1, pp. 418–428, Jul. 2013, doi: 10.3762/bjnano.4.49.
- [119] N. Elgrishi, K. J. Rountree, B. D. McCarthy, E. S. Rountree, T. T. Eisenhart, and J. L. Dempsey, "A Practical Beginner's Guide to Cyclic Voltammetry," *J. Chem. Educ.*, vol. 95, no. 2, pp. 197–206, Feb. 2018, doi: 10.1021/acs.jchemed.7b00361.
- [120] H. Kriegel, "Untersuchung von regelmäßigen Nanostrukturen für die solare Wasserspaltung," Thesis, Helmut-Schmidt-Universität / Universität der Bundeswehr Hamburg, 2020.
- [121] L. M. Peter, "Energetics and kinetics of light-driven oxygen evolution at semiconductor electrodes: the example of hematite," *Journal of Solid State Electrochemistry*, vol. 17, no. 2, pp. 315–326, Feb. 2013, doi: 10.1007/s10008-012-1957-3.
- [122] H. Dunn *et al.*, "Tin doping speeds up hole transfer during light-driven water oxidation at hematite photoanodes," *Phys. Chem. Chem. Phys.*, vol. 16, Oct. 2014, doi: 10.1039/C4CP03946G.
- [123] R. K. Franklin, S. M. Martin, T. D. Strong, and R. B. Brown, "Chemical and Biological Systems: Chemical Sensing Systems for Liquids," in *Reference Module in Materials Science and Materials Engineering*, Elsevier, 2016.
- [124] L. Girardi, M. Blanco, S. Agnoli, G. A. Rizzi, and G. Granozzi, "A DVD-MoS₂/Ag₂S/Ag Nanocomposite Thiol-Conjugated with Porphyrins for an Enhanced Light-Mediated Hydrogen Evolution Reaction," *Nanomaterials*, vol. 10, no. 7, Art. no. 7, Jul. 2020, doi: 10.3390/nano10071266.
- [125] S. D. Tilley, M. Schreier, J. Azevedo, M. Stefik, and M. Graetzel, "Ruthenium Oxide Hydrogen Evolution Catalysis on Composite Cuprous Oxide Water-Splitting Photocathodes," *Advanced Functional Materials*, vol. 24, no. 3, pp. 303–311, 2014, doi: <https://doi.org/10.1002/adfm.201301106>.

- [126] R. A. Buchanan and E. E. Stansbury, "4 - Electrochemical Corrosion," in *Handbook of Environmental Degradation of Materials (Second Edition)*, M. Kutz, Ed. Oxford: William Andrew Publishing, 2012, pp. 87–125.
- [127] U. Fegade and G. Jethave, "Chapter 8 - Advances and applications," in *Interface Science and Technology*, vol. 33, M. Ghaedi, Ed. Elsevier, 2021, pp. 557–586.
- [128] "Allen J. Bard and Larry R. Faulkner, *Electrochemical Methods: Fundamentals and Applications*, New York: Wiley, 2001, 2nd ed.," *Russian Journal of Electrochemistry*, vol. 38, no. 12, pp. 1364–1365, Dec. 2002, doi: 10.1023/A:1021637209564.
- [129] M. Leskelä and M. Ritala, "Atomic Layer Deposition Chemistry: Recent Developments and Future Challenges," *Angewandte Chemie International Edition*, vol. 42, no. 45, pp. 5548–5554, 2003, doi: <https://doi.org/10.1002/anie.200301652>.
- [130] G. Malandrino, "Chemical Vapour Deposition. Precursors, Processes and Applications. Edited by Anthony C. Jones and Michael L. Hitchman.," *Angewandte Chemie International Edition*, vol. 48, no. 41, pp. 7478–7479, 2009, doi: <https://doi.org/10.1002/anie.200903570>.
- [131] P. O. Oviroh, R. Akbarzadeh, D. Pan, R. A. M. Coetzee, and T.-C. Jen, "New development of atomic layer deposition: processes, methods and applications," *Sci Technol Adv Mater*, vol. 20, no. 1, pp. 465–496, May 2019, doi: 10.1080/14686996.2019.1599694.
- [132] K. Wenderich and G. Mul, "Methods, Mechanism, and Applications of Photodeposition in Photocatalysis: A Review," *Chem. Rev.*, vol. 116, no. 23, pp. 14587–14619, Dec. 2016, doi: 10.1021/acs.chemrev.6b00327.
- [133] Chanjuan Xi, Zhengshi Chen, Qinglin Li, and Zhensheng Jin, "Effects of H⁺, Cl⁻ and CH₃COOH on the photocatalytic conversion of PtCl₆²⁻ in aqueous TiO₂ dispersion," *Journal of Photochemistry and Photobiology A: Chemistry*, vol. 87, no. 3, pp. 249–255, Apr. 1995, doi: 10.1016/1010-6030(94)03983-2.
- [134] C. Sungbom, M. Kawai, and K. Tanaka, "XPS Studies of the Platinum Species Photodeposited on Titania from Aqueous Chloroplatinic Acid," *BCSJ*, vol. 57, no. 3, pp. 871–872, Mar. 1984, doi: 10.1246/bcsj.57.871.
- [135] J. Lee and W. Choi, "Photocatalytic Reactivity of Surface Platinized TiO₂: Substrate Specificity and the Effect of Pt Oxidation State," *J. Phys. Chem. B*, vol. 109, no. 15, pp. 7399–7406, Apr. 2005, doi: 10.1021/jp044425+.
- [136] Z. Jiang *et al.*, "Photodeposition as a facile route to tunable Pt photocatalysts for hydrogen production: on the role of methanol," *Catalysis Science & Technology*, vol. 6, no. 1, pp. 81–88, 2016, doi: 10.1039/C5CY01364J.
- [137] M. Yamamoto *et al.*, "Comparison of platinum photodeposition processes on two types of titanium dioxide photocatalysts," *Phys. Chem. Chem. Phys.*, vol. 22, no. 16, pp. 8730–8738, Apr. 2020, doi: 10.1039/C9CP06988G.
- [138] M. QAMAR and A. K. GANGULI, "Self-assembling behaviour of Pt nanoparticles onto surface of TiO₂ and their resulting photocatalytic activity," *Bull Mater Sci*, vol. 36, no. 6, pp. 945–951, Nov. 2013, doi: 10.1007/s12034-013-0556-y.
- [139] F. Mahlamvana and R. J. Kriek, "Photocatalytic reduction of platinum(II and IV) from their chloro complexes in a titanium dioxide suspension in the absence of an organic sacrificial reducing agent," *Applied Catalysis B: Environmental*, vol. 148–149, pp. 387–393, Apr. 2014, doi: 10.1016/j.apcatb.2013.11.011.
- [140] R. A. Schwarzer, D. P. Field, B. L. Adams, M. Kumar, and A. J. Schwartz, "Present State of Electron Backscatter Diffraction and Prospective Developments," in *Electron Backscatter Diffraction in Materials Science*, A. J. Schwartz, M. Kumar, B. L. Adams, and D. P. Field, Eds. Boston, MA: Springer US, 2009, pp. 1–20.
- [141] J. K. Mason and C. A. Schuh, "Representations of Texture," in *Electron Backscatter Diffraction in Materials Science*, A. J. Schwartz, M. Kumar, B. L. Adams, and D. P. Field, Eds. Boston, MA: Springer US, 2009, pp. 35–51.

- [142] S. Fengler *et al.*, "Charge Transfer in c-Si(n++)/TiO₂(ALD) at the Amorphous/Anatase Transition: A Transient Surface Photovoltage Spectroscopy Study," *ACS Appl. Mater. Interfaces*, vol. 12, no. 2, pp. 3140–3149, Jan. 2020, doi: 10.1021/acsami.9b17592.
- [143] C. Ros, T. Andreu, M. D. Hernández-Alonso, G. Penelas-Pérez, J. Arbiol, and J. R. Morante, "Charge Transfer Characterization of ALD-Grown TiO₂ Protective Layers in Silicon Photocathodes," *ACS Appl. Mater. Interfaces*, vol. 9, no. 21, pp. 17932–17941, May 2017, doi: 10.1021/acsami.7b02996.
- [144] M. Kamei, "Localization of the Photocatalytic Reaction on the Grain Boundary of Bicrystalline TiO₂," *Applied Physics Express - APPL PHYS EXPRESS*, vol. 1, Oct. 2008, doi: 10.1143/APEX.1.101201.
- [145] E. S. Machlin, "Chapter II - Defect structure," in *Materials Science in Microelectronics I (Second Edition)*, E. S. Machlin, Ed. Oxford: Elsevier, 2005, pp. 23–53.
- [146] I. Jelovica Badovinac *et al.*, "Grain size effect on photocatalytic activity of TiO₂ thin films grown by atomic layer deposition," *Thin Solid Films*, vol. 709, p. 138215, Sep. 2020, doi: 10.1016/j.tsf.2020.138215.
- [147] M. Ibadurrohman and K. Hellgardt, "Importance of surface roughness of TiO₂ photoanodes in promoting photoelectrochemical activities with and without sacrificial agent," *Thin Solid Films*, vol. 705, p. 138009, Jul. 2020, doi: 10.1016/j.tsf.2020.138009.
- [148] F. E. Osterloh, "Inorganic nanostructures for photoelectrochemical and photocatalytic water splitting," *Chem. Soc. Rev.*, vol. 42, no. 6, pp. 2294–2320, Feb. 2013, doi: 10.1039/C2CS35266D.
- [149] M. Chamtoury *et al.*, "Facet-Dependent Diol-Induced Density of States of Anatase TiO₂ Crystal Surface," *ACS Omega*, vol. 2, no. 7, pp. 4032–4038, Jul. 2017, doi: 10.1021/acsomega.6b00473.
- [150] B. Kenens *et al.*, "Solvent-induced improvement of Au photo-deposition and resulting photocatalytic efficiency of Au/TiO₂," *RSC Adv.*, vol. 6, no. 100, pp. 97464–97468, Oct. 2016, doi: 10.1039/C6RA19372B.
- [151] L. Chu, Z. Qin, J. Yang, and X. Li, "Anatase TiO₂ Nanoparticles with Exposed {001} Facets for Efficient Dye-Sensitized Solar Cells," *Scientific Reports*, vol. 5, no. 1, Art. no. 1, Jul. 2015, doi: 10.1038/srep12143.
- [152] H. G. Yang *et al.*, "Solvothermal Synthesis and Photoreactivity of Anatase TiO₂ Nanosheets with Dominant {001} Facets," *J. Am. Chem. Soc.*, vol. 131, no. 11, pp. 4078–4083, Mar. 2009, doi: 10.1021/ja808790p.
- [153] Y.-K. Peng *et al.*, "Unravelling the key role of surface features behind facet-dependent photocatalysis of anatase TiO₂," *Chem. Commun.*, vol. 55, no. 30, pp. 4415–4418, Apr. 2019, doi: 10.1039/C9CC01561B.
- [154] C. Adler, D. Mitoraj, I. Krivtsov, and R. Beranek, "On the importance of catalysis in photocatalysis: Triggering of photocatalysis at well-defined anatase TiO₂ crystals through facet-specific deposition of oxygen reduction cocatalyst," *J. Chem. Phys.*, vol. 152, no. 24, p. 244702, Jun. 2020, doi: 10.1063/5.0013115.
- [155] Y. Luan, L. Jing, Y. Xie, X. Sun, Y. Feng, and H. Fu, "Exceptional Photocatalytic Activity of 001-Facet-Exposed TiO₂ Mainly Depending on Enhanced Adsorbed Oxygen by Residual Hydrogen Fluoride," *ACS Catal.*, vol. 3, no. 6, pp. 1378–1385, Jun. 2013, doi: 10.1021/cs400216a.
- [156] A. Selloni, "Anatase shows its reactive side," *Nature Materials*, vol. 7, no. 8, Art. no. 8, Aug. 2008, doi: 10.1038/nmat2241.
- [157] W. Wang, C. Lu, Y. Ni, and Z. Xu, "Crystal facet growth behavior and thermal stability of {001} faceted anatase TiO₂: mechanistic role of gaseous HF and visible-light photocatalytic activity," *CrystEngComm*, vol. 15, no. 13, pp. 2537–2543, Mar. 2013, doi: 10.1039/C2CE26702K.
- [158] R. Hengerer, B. Bolliger, M. Erbudak, and M. Grätzel, "Structure and stability of the anatase TiO₂ (101) and (001) surfaces," *Surface Science*, vol. 460, no. 1, pp. 162–169, Jul. 2000, doi: 10.1016/S0039-6028(00)00527-6.
- [159] M. Lazzeri and A. Selloni, "Stress-driven reconstruction of an oxide surface: the anatase TiO₂(001)-(1 × 4) surface," *Phys Rev Lett*, vol. 87, no. 26, p. 266105, Dec. 2001, doi: 10.1103/PhysRevLett.87.266105.

- [160] G. Li *et al.*, “Surface study of the reconstructed anatase TiO₂ (001) surface,” *Progress in Natural Science: Materials International*, vol. 31, no. 1, pp. 1–13, Feb. 2021, doi: 10.1016/j.pnsc.2020.11.002.
- [161] H. Kriegel, J. Kollmann, R. Raudsepp, T. Klassen, and M. Schieda, “Chemical and photoelectrochemical instability of amorphous TiO₂ layers quantified by spectroscopic ellipsometry,” *Journal of Materials Chemistry A*, vol. 8, no. 35, pp. 18173–18179, 2020, doi: 10.1039/D0TA04878J.
- [162] K. Schwarzburg and F. Willig, “Influence of trap filling on photocurrent transients in polycrystalline TiO₂,” *Appl. Phys. Lett.*, vol. 58, no. 22, pp. 2520–2522, Jun. 1991, doi: 10.1063/1.104839.
- [163] S. D. R. Stangl, A. Laades, and S. C., “Recombination analysis at the n doped a Si H n c Si p heterojunction by means of time and intensity dependent surface photovoltage,” Jan. 2005.
- [164] R. Chen, F. Fan, T. Dittrich, and C. Li, “Imaging photogenerated charge carriers on surfaces and interfaces of photocatalysts with surface photovoltage microscopy,” *Chem. Soc. Rev.*, vol. 47, no. 22, pp. 8238–8262, Nov. 2018, doi: 10.1039/C8CS00320C.
- [165] M. A. Reshchikov, M. Foussekis, and A. A. Baski, “Surface photovoltage in undoped n-type GaN,” *Journal of Applied Physics*, vol. 107, no. 11, p. 113535, Jun. 2010, doi: 10.1063/1.3430979.
- [166] A. Winnerl, R. N. Pereira, and M. Stutzmann, “Kinetics of optically excited charge carriers at the GaN surface,” *Phys. Rev. B*, vol. 91, no. 7, p. 075316, Feb. 2015, doi: 10.1103/PhysRevB.91.075316.
- [167] R. B. Darling, “Defect-state occupation, Fermi-level pinning, and illumination effects on free semiconductor surfaces,” *Phys. Rev. B*, vol. 43, no. 5, pp. 4071–4083, Feb. 1991, doi: 10.1103/PhysRevB.43.4071.
- [168] V. Vrakatseli, E. Farsari, and D. Mataras, “Wetting Properties of Transparent Anatase/Rutile Mixed Phase Glancing Angle Magnetron Sputtered Nano-TiO₂ Films,” *Micromachines (Basel)*, vol. 11, no. 6, Jun. 2020, doi: 10.3390/mi11060616.
- [169] A. Terriza *et al.*, “Light induced hydrophilicity and osteoblast adhesion promotion on amorphous TiO₂,” *Journal of Biomedical Materials Research Part A*, vol. 101A, no. 4, pp. 1026–1035, 2013, doi: <https://doi.org/10.1002/jbm.a.34405>.
- [170] V. Rico, P. Romero, J. L. Hueso, J. P. Espinós, and A. R. González-Elipe, “Wetting angles and photocatalytic activities of illuminated TiO₂ thin films,” *Catalysis Today*, vol. 143, no. 3, pp. 347–354, May 2009, doi: 10.1016/j.cattod.2008.09.037.
- [171] V. Vrakatseli, E. Pagonis, E. Amanatides, and D. Mataras, “Photoinduced superhydrophilicity of amorphous TiO_x-like thin films by a simple room temperature sol-gel deposition and atmospheric plasma jet treatment,” Jun. 2014, vol. 550, doi: 10.1088/1742-6596/550/1/012034.
- [172] M. Rezeq, K. Eledlebi, M. Ismail, R. K. Dey, and B. Cui, “Theoretical and experimental investigations of nano-Schottky contacts,” *Journal of Applied Physics*, vol. 120, no. 4, p. 044302, Jul. 2016, doi: 10.1063/1.4959090.
- [173] D.-Z. Guo, S.-M. Hou, G.-M. Zhang, and Z.-Q. Xue, “Conductance fluctuation and degeneracy in nanocontact between a conductive AFM tip and a granular surface under small-load conditions,” *Applied Surface Science*, vol. 252, no. 14, pp. 5149–5157, May 2006, doi: 10.1016/j.apsusc.2005.07.058.
- [174] L. Jiang *et al.*, “Understanding Current Instabilities in Conductive Atomic Force Microscopy,” *Materials (Basel)*, vol. 12, no. 3, Feb. 2019, doi: 10.3390/ma12030459.
- [175] S. A. Sumaiya, A. Martini, and M. Z. Baykara, “Improving the reliability of conductive atomic force microscopy-based electrical contact resistance measurements,” *Nano Ex.*, vol. 1, no. 3, p. 030023, Nov. 2020, doi: 10.1088/2632-959X/abcae0.
- [176] W. Lu, L.-M. Wong, S. Wang, and K. Zeng, “Effects of oxygen and moisture on the I-V characteristics of TiO₂ thin films,” *Journal of Materiomics*, vol. 4, no. 3, pp. 228–237, Sep. 2018, doi: 10.1016/j.jmat.2018.01.005.

- [177] N. A. Lashkova, N. V. Permiakov, A. I. Maximov, Y. M. Spivak, and V. A. Moshnikov, "Local analysis of semiconductor nanoobjects by scanning tunneling atomic force microscopy," *St. Petersburg Polytechnical University Journal: Physics and Mathematics*, vol. 1, no. 1, pp. 15–23, Mar. 2015, doi: 10.1016/j.spjpm.2015.03.014.
- [178] V. Cambel and J. Šoltýs, "The influence of sample conductivity on local anodic oxidation by the tip of atomic force microscope," *Journal of Applied Physics*, vol. 102, no. 7, p. 074315, Oct. 2007, doi: 10.1063/1.2794374.
- [179] I. Dugdale and J. B. Cotton, "The anodic polarization of titanium in halide solutions," *Corrosion Science*, vol. 4, no. 1, pp. 397–411, Jan. 1964, doi: 10.1016/0010-938X(64)90041-1.
- [180] J. Liu, A. Alfantazi, and E. Asselin, "Effects of Temperature and Sulfate on the Pitting Corrosion of Titanium in High-Temperature Chloride Solutions," *J. Electrochem. Soc.*, vol. 162, no. 4, p. C189, Jan. 2015, doi: 10.1149/2.0541504jes.
- [181] S. M. Kramer, I. G. Gorichev, Yu. A. Lainer, I. V. Artamonova, and M. V. Terekhova, "Calculation of the solubility of TiO₂ and titanates in sulfuric acid solutions," *Russ. Metall.*, vol. 2014, no. 9, pp. 704–707, Sep. 2014, doi: 10.1134/S0036029514090109.
- [182] I. G. Gorichev and N. A. Kipriyanov, "Regular Kinetic Features of the Dissolution of Metal Oxides in Acidic Media," *Russ. Chem. Rev.*, vol. 53, no. 11, p. 1039, Nov. 1984, doi: 10.1070/RC1984v053n11ABEH003139.
- [183] B. Díaz *et al.*, "Low-temperature atomic layer deposition of Al₂O₃ thin coatings for corrosion protection of steel: Surface and electrochemical analysis," *Corrosion Science*, vol. 53, no. 6, pp. 2168–2175, Jun. 2011, doi: 10.1016/j.corsci.2011.02.036.
- [184] Z. Chai, J. Li, X. Lu, and D. He, "Use of electrochemical measurements to investigate the porosity of ultra-thin Al₂O₃ films prepared by atomic layer deposition," *RSC Adv.*, vol. 4, no. 74, pp. 39365–39371, Aug. 2014, doi: 10.1039/C4RA04565C.
- [185] S. Mirhashemihaghighi *et al.*, "Electrochemical and Surface Analysis of the Corrosion Protection of Copper by Nanometer-Thick Alumina Coatings Prepared by Atomic Layer Deposition," *Journal of the Electrochemical Society*, vol. 162, pp. C377–C384, May 2015, doi: 10.1149/2.0081508jes.
- [186] K. K. Ghuman and C. V. Singh, "Self-Trapped Charge Carriers in Defected Amorphous TiO₂," *J. Phys. Chem. C*, vol. 120, no. 49, pp. 27910–27916, Dec. 2016, doi: 10.1021/acs.jpcc.6b07326.
- [187] H. Gerischer, "On the stability of semiconductor electrodes against photodecomposition," *Journal of Electroanalytical Chemistry and Interfacial Electrochemistry*, vol. 82, no. 1, pp. 133–143, Sep. 1977, doi: 10.1016/S0022-0728(77)80253-2.

Acknowledgements

This thesis would have not been possible without the contribution of many people I would like to thank in this part.

First of all, my greatest gratitude goes to my supervisor Dr. Mauricio Schieda who has been supporting me throughout my whole PhD. I could not have done it without him.

Very special thanks go to Prof. Thomas Klassen for the opportunity to be a part of his groups in Helmut Schmidt University and Helmholtz – Zentrum Hereon. Thank you for your guidance and advice and most important – always being positive.

I would like to thank Dr. Maria Villa Vidaller for giving me the opportunity to start my PhD at the Young Investigator's group.

I am very grateful to Prof. Thomas Dittrich for his advice and ideas regarding the surface voltage mapping chapter in this thesis.

I thank Bernhard Eltzhig from the Helmholtz – Zentrum Hereon workshop for preparing the AFM-EC cells.

I would like to thank all my friends and colleagues in Helmut Schmidt University and Helmholtz – Zentrum Hereon. I am especially thankful to Dr. Herman Kriegel who provided me the samples to investigate, proofread the numerous preliminary drafts of this thesis and always listened when I needed some advice. I would also like to thank Jiri Kollmann for the samples, discussions we had and your supportive words. I thank Dr. Carmen Tenholt, Dr. Steffen Fengler and Dr. Lucian Blaga for cross-reading some of the preliminary chapters in this thesis and for their feedback and advice.

Thank you Zhida Liang for all the coffee breaks and discussions about everything and nothing.

Finally, I thank all my friends and family in Estonia and in Germany, especially my beloved partner Paul, who never stopped believing in me and gave me all the time I needed to devote myself to this thesis.

Posters and Presentations at conferences

Posters

Characterization of Microscopic Interface Phenomena of Water Splitting Photo-electrodes by Scanning Probe Microscopy, ZHM Kick-off Event, Geesthacht, March 2016.

Big Data Mining in Scanning Probe Microscopy, ZHM Symposium, Geesthacht, November 2018.

Presentations

Characterization of Water-Splitting Photoelectrodes by Scanning Probe Microscopy, IAMNano Conference, Hamburg, October 2018.

Invited talk, Characterization of Water-Splitting Photoelectrodes by Scanning Probe Microscopy, International Workshop on Photovoltaic and Hydrogen Energy Technologies, Port Elizabeth, July 2019.

Characterization of Water-Splitting Photoelectrodes by Scanning Probe Microscopy, 10th Workshop on Scanning Electrochemical Microscopy and Related Techniques, Paris, September 2019.

Invited talk, Characterization of Water-Splitting Photoelectrodes by Scanning Probe Microscopy, 4th Sino-German Symposium on Aberration-Corrected and In Situ Electron Microscopy and Spectroscopy in the Age of Big Data, Beijing, October 2019.

Publications

H. Kriegel, J. Kollmann, R. Raudsepp, T. Klassen, M. Schieda, "Chemical and photoelectrochemical instability of amorphous TiO₂ layers quantified by spectroscopic ellipsometry", *Journal of Materials Chemistry A*, vol. 8, no. 35, pp. 18173–18179, 2020

Manuscripts in preparation:

R. Raudsepp, H. Kriegel, J. Kollmann, T. Klassen, M. Schieda, "*In-situ* AFM characterization of the photoelectrochemical stability of TiO₂ thin films prepared by atomic layer deposition"

„Correlative studies with AFM and EBSD on a ALD TiO₂“

"Mapping the charge carrier transport mechanism and Schottky barrier height at the metal tip/semiconductor interface"

G. V. Krishnamrthy, M. Chirumamilla, T. Krekeler, M. Ritter, R. Raudsepp, M. Schieda, A. Y. Petrov, M. Eich, M. Störmer, „Investigation of magnetron sputtered hafnium oxide films“.